UNIVERSITY OF CALIFORNIA SAN DIEGO

Dissecting Circuits that Coordinate Spike Timing in the Hippocampus and Medial Entorhinal Cortex

A dissertation submitted in partial satisfaction of the
requirements for the degree Doctor of Philosophy

in

Biology

by

Ipshita Zutshi

Committee in charge:

Professor Stefan Leutgeb, Chair
Professor Jeffry S. Isaacson
Professor Jill K. Leutgeb
Professor Byungkook Lim
Professor Mark Mayford

2019

The Dissertation of Ipshita Zutshi is approved, and it is acceptable in quality and form for publication on microfilm and electronically:

_____

_____

_____

_____

_____

Chair

University of California San Diego

2019

DEDICATION

To my family, for their love,

To my mentors, for their faith,

To my friends, for their laughter,

And to darling Scooby, my source of comfort.

EPIGRAPH

"I know, my dear Watson, that you share my love of all that is bizarre and outside the conventions and humdrum routine of everyday life."

— Sir Arthur Conan Doyle, Sherlock Holmes

TABLE OF CONTENTS

LIST OF FIGURES

LIST OF TABLES

ACKNOWLEDGEMENTS

I have learnt several lessons during my PhD. But perhaps the most important is the knowledge that it is easy to dabble and tinker with protocols, obtain results and plot graphs. But this does not make one a scientist. The real challenge lies in asking the right questions, seeking answers and embracing results when they are contrary to what we expect. My PI, Stefan Leutgeb, has taught me by example of what being a scientist truly means. I am grateful to him for his support and guidance throughout all my thesis projects, but perhaps more importantly, I thank him for acting as a role model who I can emulate in my career. His encyclopedic knowledge, approachable nature, keen grasp on concepts and humility have often left me astounded, and I am so fortunate to have been trained by someone like him. I have also been fortunate enough to receive encouragement, feedback, and support from several other mentors along the way. I would like to thank Byungkook Lim for teaching me the wonders of using novel tools in neuroscience, while being an approachable mentor I could turn to for advice and reassurance. I would also like to thank Jill Leutgeb for her valuable feedback and comments at every stage of my project. Lastly, I would like to thank my remaining committee members – Jeffry Isaacson and Mark Mayford for their instrumental role in guiding my project and career.

Of course, none of the work described here was done in isolation. I would like to acknowledge Mark Brandon, my first teacher, and at times, personal cheerleader. I would also like to thank the very talented Maylin Fu, who not only performed a large part of the cumbersome experiments described in this thesis, but also became my closest friend forced to hear long rants on failed experiments. I am grateful to the other brilliant undergraduate student volunteers I was fortunate enough to work with - Stanley Liu and Gecelle de Guia. I am also grateful to my office mates, aka, gossip buddies, Marta Sabariego-Collett and Silvia Viana da Silva who have been my go-to source for advice and comfort. In addition, I would like to thank the rest of my lab mates –

Clare Quirk, Sunandha Srikanth, Geoffrey Diehl, Laura Ewell, Siavash Ahmadi, Magda Schlesiger, Macayla Donegan and Anna-Lena Schlenner, with whom I have often collaborated, learnt, and been supported, and without whom graduate school would have been a lot harder. In addition to members in the Leutgeb lab, I must acknowledge friends and collaborators in the other labs. Members of the Lim lab have not only freely allowed me to use equipment, viruses and microscopes, but also helped me learn all of these techniques. I would like to especially thank Varoth Lilascharoen for selflessly generating and providing viruses, as well as the other Lim lab members including Xiao-Yun and Daniel Knowland. I would like to thank Eric Wang, not just for his everlasting patience on virus related queries, but also for the long discussions (which also forced me to stop being lazy and walk every once in a while) and inspiration for shaping the questions I want to ask in the future. I would also like to thank Andre Sousa from the Mayford lab for a fun and successful collaboration. Lastly, during my PhD, I have spent countless hours performing surgery or histology listening to podcasts by This American Life, Radiolabs or the Moth RadioHour, and audiobooks (i.e., All 7 harry potter books on loop) on Audible. They really helped the hours go by, and I would have probably only been half as productive without them.

I have been fortunate to have the support of my classmates from the Biology Graduate Program – Pragya, my movie partner and piece of high school in San Diego, and Nandu, Ami, Angela, Varoth, Yeara, Mai, Mizu, Bu, Meiyan, Sia, Alison and Hyeseon whose monthly gatherings often kept me going. They have been a set of friends I could rely on and share woes with throughout my PhD, and I am grateful for their support.

In addition to a set of friends, I have also been able to receive support from UCSD in so many other ways. I would like to thank the faculty, my rotation PIs, and class instructors for teaching me much of what I know today. The collaborative environment at UCSD, with constant seminars and neurodinners has taught me to appreciate science across multiple fields. I would like

to thank the biology graduate division for seamlessly taking care of all financial and administrative paperwork, allowing me to just focus on the science. I would also like to thank the staff in Pacific Hall, and specifically those in the vivarium – Neil and Scott without whom my graduate work would have been substantially more frustrating.

I was fortunate enough to be supported with a Howard Hughes Medical Institute International Student Research Fellowship. Apart from providing me a stable source of funding for three years of my PhD, this grant provided me with funding to attend conferences and purchase supplies. These conferences have helped shape my future trajectory and I am extremely grateful to HHMI for making this possible.

I could not be where I am today had it not been for years of support and guidance from past mentors and teachers. I would like to thank Ravi Gopinath for being the first to instill a passion for neuroscience. I am grateful to my professors from BITS Pilani – Manoj Kannan, Rajesh Mehrotra, AK Das, and Suman Kapur for providing me training opportunities in their labs and inspiring me to pursue a career in research. I am also indebted to Ronald Kalil – he was the first mentor to show me what it really meant to be a scientist, and probably is the reason I got into graduate school in the first place. Finally, I would like to thank my other research mentors – Osborne Almeida and Carmen Sandi, who trained me, and took a chance on me when I had no experience. I stand today on the shoulders of these giants.

In addition to all the friends and colleagues I have made in my professional career, I have been fortunate to have the support of friends and family at every step of the journey. I am grateful to all my friends from high school – the Bombshell Blossoms, Mahima, Mukund, and Saksham, but most of all Mukta, who has been my best friend-cum-sister for the past 18 years, and Aarushi for being a source of comfort (literally, with heated car seats) in a foreign land. I am so grateful to my friends from college who have made me happier than I could have ever imagined. I thank my

BFFs – Aman, Ankita, Dhwani and Zara for XOXO chats and all the love. I thank Akhil for proofreading all my grad school application essays and being the only one who attempted to read my papers. I am grateful for the support of Kaul and Karthik, who have always cheered me while ensuring they make fun of me, and Sukrit for reminding me to party every now and then. I also thank Gandhi, Pranjal, Birdie, Sud, SidG, SidLa, Nishith and the several others who have patiently dealt with my incessant worries, and yet continued to be friends with me.

Most of all, I am immensely grateful to Sachin Sethi. He has been my biggest rival, my closest confidante, my personal advisor, and guidance counselor. He motivates me to be more hard working, more diligent, more ambitious and a better scientist every second of every day. I have known him as a classmate, a friend, a lab mate, a collaborator, a classmate again, and now my fiancé, and I would have probably not lasted a day in graduate school without him.

And none of this of course, would have ever been possible without the support of my family. My parents – Mondira Dutta and Bupinder Zutshi, both professors, are the toughest, most resilient, and most brilliant people I know. They have sheltered me from all troubles, and always encouraged me by providing me with a level of freedom, independence and trust that is rare. I would like to thank my brother, Aneesh Zutshi, whose unconventional habit of teaching me fluid mechanics since I was 5, probably led to my love of science today. I would also like to thank my sister in law, Tahere Nodehi, for all her encouragement along the way. Lastly, I would like to thank my dog, Scooby, who brought me more joy than anything else in this world. Together, my family is solely responsible for who I am today, and I owe it all to them. Words cannot express how grateful I am for them, and how much I miss them when I am away.

Finally, I would like to acknowledge the countless mice that I have used over the course of my research projects. Their sacrifice is what made my research possible, and I am acutely aware of

the level of privilege to be able to perform such experiments. I will always try to ensure that this sacrifice is never in vain.

Chapter 2, in full, is material that is unpublished and coauthored by Zutshi, I, Fu, ML, Lilascharoen, V, Leutgeb, JK, Lim, BK, and Leutgeb, S. The dissertation author was the primary researcher of this material.

Chapter 3, in full, is material as it appears in *Nature Communications*, 2018, Zutshi, Ipshita, Fu, Maylin L., Lilascharoen, Varoth, Leutgeb, Jill K., Lim, Byungkook, Leutgeb, Stefan (Zutshi et al., 2018a). The dissertation author was the primary researcher and author of this paper.

Chapter 4, in full, is material as it appears in *Current Biology*, 2018, Zutshi, Ipshita, Brandon, Mark P., Fu, Maylin L., Donegan, Macayla L., Leutgeb, Jill K., Leutgeb, Stefan (Zutshi et al., 2018b). The dissertation author was a primary researcher and author of this paper.

Chapter 5, in full, is material as it appears in *Current Opinion in Behavioral Sciences*, 2018, Zutshi, Ipshita, Leutgeb, Jill K., Leutgeb, Stefan (Zutshi et al., 2017). The dissertation author was the primary researcher and author of this paper.

VITA

2013 Master of Science (Hons.) and Bachelor of Engineering (Hons.), Birla Institute of Technology and Science, Pilani, India
2019 Doctor of Philosophy, University of California San Diego, USA

PUBLICATIONS

Mehrotra R, Sethi S*, Zutshi I*, Bhalothia P and Mehrotra S (2013). Patterns and evolution of ACGT repeat cis-landscape across four plant genomes. *BMC Genomics* 14 (1), 203. * These authors contributed equally

Yu, S, Zutshi, I, Stoffel, R, Zhang, J, Ventura-Silva, AP, Sousa, N, Costa, PS, Holsboer, F, Patchev, A, and Almeida, OFX (2017). Antidepressant responsiveness in adulthood is permanently impaired after neonatal destruction of the neurogenic pool. *Translational Psychiatry* 7 (1), e990.

Zutshi, I, Leutgeb, JK, and Leutgeb, S (2017). Theta sequences of grid cell populations can provide a movement-direction signal. *Current opinion in behavioral sciences* 17, 147-154.

Hendrickson, ML, Zutshi, I, Wield, A, and Kalil, RE (2018). Nestin expression and in vivo proliferative potential of tanycytes and ependymal cells lining the walls of the third ventricle in the adult rat brain. *European Journal of Neuroscience* 47 (4), 284-293.

Zutshi, I*, Brandon, MP*, Fu, ML, Donegan, M, Leutgeb, JK, and Leutgeb, S (2018). Hippocampal neural circuits respond to optogenetic pacing of theta frequencies by generating accelerated oscillation frequencies. *Current Biology* 28 (8), 1179-1188. *These authors contributed equally

Zutshi, I, Fu, ML, Lilascharoen, V, Leutgeb, JK, Lim, BK, and Leutgeb, S (2018). Recurrent circuits within medial entorhinal cortex superficial layers support grid cell firing. *Nature Communications* 9 (1), 3701.

De Sousa, AF, Zutshi, I, Cowansage, KK, Cardozo LM, Yoo, EJ, Leutgeb, S, and Mayford, M. Optogenetic reactivation of memory ensembles in the retrosplenial cortex induces systems consolidation. *In revision.*

FIELDS OF STUDY

Major Field: Biological Sciences

Studies in Biological Sciences, PhD
Professor Stefan Leutgeb

Studies in Biological Sciences, MSc
Professor Carmen Sandi

ABSTRACT OF THE DISSERTATION

Dissecting Circuits that Coordinate Spike Timing in the Hippocampus and Medial Entorhinal Cortex

by

Ipshita Zutshi

Doctor of Philosophy in Biology

University of California San Diego, 2019

Professor Stefan Leutgeb, Chair

Memory and spatial navigation involve complex neural processes that depend on accurate and coordinated firing of neurons within the hippocampus and medial entorhinal cortex (mEC). Neurons within these regions are tuned to various features of the environment, including space and context, and incorrect firing is hypothesized to lead to catastrophic errors in our ability to generate new, stable, and coherent memories. There are numerous methods in which the brain might establish and maintain reliable firing, and here, we examined different network mechanisms that

determine spike timing. The first property that significantly influences the firing of neurons is the network connectivity of cells within and between brain regions. To understand how networks are organized within the mEC, we employed rabies virus-mediated retrograde trading and determined that projections within the superficial layers of the mEC are organized as cortical columns, parallel to the radial axis of the brain. Next, with information on how these local projections are organized, we performed transient, local perturbations of these circuits and examined whether the precise spatial firing of neurons within the mEC is dependent on these local circuits. While we found small errors in the spatial firing of grid cells following each perturbation, these errors were brief and not cumulative, suggesting robust mechanisms for afferent inputs to maintain firing.

In addition to the connectivity between neurons, a key factor coordinating spike timing, especially between brain regions, are global oscillations that act as an external pacemaker. Within the context of the mEC and hippocampus, these are called theta oscillations, and most neurons within these brain regions are rhythmically paced to theta oscillations. To test how these oscillations might coordinate spike timing, we artificially accelerated the frequency of theta oscillations and determined that neurons within the hippocampus respond to the stimulation by shifting their oscillation frequencies to match the stimulation frequency. Finally, we provide an example of how a functional readout of coordinated spiking between neurons involving both the above described mechanisms – a local network dependent rate code, and theta oscillation dependent temporal code – may be used on a population level to generate complex internal representations.

I.

Introduction

"Memories warm you up from the inside. But they also tear you apart."

-Haruki Murakami, Kafka on the Shore

Curiosity, philosophy and art - all extraordinary abilities of the human mind, are also the key features that distinguish us humans from our evolutionary predecessors. Perhaps the biggest testament of these abilities is our endeavor to uncover the mysteries of the brain, the very source of our remarkable abilities. The brain has been the subject of fascination documented by early philosophers and religious texts, dating back to 4000 B.C., but perhaps the significance of the brain was first proposed by Alcmaeon of Croton in his book *De Natura* back around 500 B.C., where he attributed the functioning of the 'mind' to the brain instead of the heart, as was commonly believed by several philosophers in those days, including Aristotle (Debernardi et al., 2010).

However, the earliest, best-preserved documentation of the relationship between the brain and mind is within the 400 B.C. book, 'On the Sacred Disease', by Hippocrates, describing his observations of the epileptic brain (Hippocrates, 1990). Here, Hippocrates writes,

> *And men ought to know that from nothing else but (from the brain) come joys, delights, laughter and sports, and sorrows, griefs, despondency, and lamentations. And by this, in an especial manner, we acquire wisdom and knowledge, and see and hear, and know what are foul and what are fair, what are bad and what are good, what are sweet, and what unsavory; some we discriminate by habit, and some we perceive by their utility. By this we distinguish objects of relish and disrelish, according to the seasons; and the same things do not always please us. And by the same organ we become mad and delirious, and fears and terrors assail us, some by night, and some by day, and dreams and untimely wanderings, and cares that are not suitable, and ignorance of present circumstances, desuetude, and unskillfulness.*

These musings eventually set the stage for the field of neuroscience as we know it today, with incremental advances in our knowledge by experiments and theories proposed by exceptional

scientists and philosophers. Perhaps unsurprisingly, the earliest studies of the brain focused on brain anatomy – of the ventricular structures, and of the characterization of different structures within the brain – and as our understanding of different brain regions grew, so did our knowledge of the individual functions of each sub-region. While the earliest empirical studies connecting structure and function focused on sensory perceptions, it was not until the late 1800s that the more complex and abstract field of memory research was brought to the laboratory by Hermann Ebbinghaus.

The revolution of empirical research, and a growing interest in understanding memory brought about the earliest attempts to understand where memories are stored within the brain. The pioneer of these studies was Karl Lashley, who performed intricate experiments by training rats to run along a simple maze back in 1920. He subsequently removed different areas of cortex to find a causal role between a certain region of the cortex and memory impairments. He discovered that while the severity of memory impairment correlated with the amount of cortex removed, there was no correlation between specific parts of the cortex and memory (Lashley, 1950). While correct in interpreting that there is no single center where all memories are permanently stored, Lashley's focus on the cerebral cortex prevented him from implicating any one brain region as responsible for memory formation. Instead, the earliest suggestions of aspects of memory being localized to a single brain region were provided by Wilder Penfield in 1938. Coincidentally, akin to Hippocrates' observations, Penfield's inferences arose while performing treatment on patients with focal epilepsy. He developed a technique to remove small regions of the brain that would trigger epileptic attacks, and while doing so, applied weak artificial stimulation across different brain regions to determine which regions were involved in the patients' ability for speech and comprehension, thereby avoiding those areas. While performing these weak simulations, he would occasionally find patients who would experience coherent perceptions, as described in the following excerpt from his article (Penfield, 1952),

> *When, in another case, that of D. F., a point on the superior surface of the right temporal lobe was stimulated within the fissure of Sylvius, the patient heard a specific popular song being played as though by an orchestra. Repeated stimulations reproduced the same music. While the electrode was kept in place, she hummed the tune, chorus, and verse, thus accompanying the music she heard.*
>
> *The patient, L. G., was caused to experience "something," he said, that had "happened" to him before. Stimulation at another temporal point caused him to see a man and a dog walking along a road near his home in the country.*
>
> *Another woman heard a voice which she did not quite understand when the first temporal convolution was stimulated initially. When the electrode was reapplied to approximately the same point, she heard a voice distinctly, calling "Jimmie, Jimmie, Jimmie"—Jimmie was the nickname of the young husband to whom she had been married recently.*

In his article, Penfield describes how all of these vivid recollections occurred only when he stimulated certain regions of the temporal lobe, which he described as the 'memory cortex'. Ultimately, the knowledge that the temporal lobe plays a crucial role in memory was established by William Scoville and Brenda Milner in 1957, with their examinations of the patient H.M, who, to treat his severe focal epilepsy, had a bilateral medial temporal lobe resection. H.M. suffered from debilitating memory loss following the resection, with a complete inability to form new memories. Some examples to describe his symptoms are provided here (Scoville and Milner, 1957).

> *This patient's memory defect has persisted without improvement to the present time, and numerous illustrations of its severity could be given. Ten months ago, the family moved from their old house to a new one a few blocks away on the same street; he still has not learned the new address, though remembering the old one perfectly, nor can he be trusted to find his way home alone…This patient has even eaten luncheon in front of one of us (B. M.) without being able to name, a mere half-hour later, a single item of food he had eaten; in fact, he could not remember having eaten luncheon at all. Yet to a casual observer this man seems like a relatively normal individual, since his understanding and reasoning are undiminished.*

As a result of these findings, by the end of the 1950s, the role of the medial temporal lobe in generating declarative memories, i.e., the memory of facts and events, became indisputably established.

Structure and organization of the medial temporal lobe

The medial temporal lobe comprises several sub-regions (Squire and Zola-Morgan, 1991): the hippocampal region (including the CA1, CA2 and CA3 fields, the dentate gyrus, and the subicular complex), and the adjacent entorhinal, perirhinal and parahippocampal cortices. In terms of the basic network architecture, sensory information from the primary cortices reaches the perirhinal and parahippocampal cortices through multiple parallel pathways, to give rise to multimodal representations. These perirhinal and parahippocampal regions project densely to the entorhinal cortex, which is the primary source of excitation to the hippocampus. Information is processed locally within the hippocampus, which projects back to the entorhinal cortex, which in turn sends information back out to the cortical and association areas (Squire et al., 2004). The entorhinal cortex can be further subdivided into two anatomical regions, the medial entorhinal cortex (mEC) and the lateral entorhinal cortex (lEC). The cytoarchitectural character and the projections to and from the medial and lateral aspects of the entorhinal cortex are vastly distinct (Amaral and Witter, 1989; Van Strien et al., 2009; Witter and Amaral, 1991, 2004), with the lEC receiving the majority of its projections from the perirhinal cortex and the mEC receiving dense projections from the parahippocampal regions. The efferent projections from the lEC and mEC to the hippocampal subregions also diverge considerably, suggesting independent functions of the two entorhinal regions. Within this dissertation, we will focus specifically on the hippocampal and mEC sub-regions, with occasional references to the projections from the parahippocampal cortices to the mEC.

The mEC is a six layered cortical structure, with layers I and IV being primarily cell-free. In terms of information flow, layers II and III, referred to as the mEC superficial layers, receive extensive projections from the parahippocampal cortices and the medial septal area, and project densely to the hippocampus (Van Strien et al., 2009; Witter et al., 1988). Neurons in layer II and III diverge in their projections to the hippocampus, with mEC layer III projecting primarily to the

distal and proximal ends of the stratum lacunosum moleculare in CA1. On the other hand, the neurons in layer II are broadly subdivided in two major excitatory cell populations, each with distinct projections to the hippocampus. Stellate cells, which are present all along the mEC layer II and typically express the trans-membrane protein *reelin,* project densely to the outer molecular layer of the dentate gyrus (DG) and stratum lacunosum molecular of CA3. The second excitatory sub-population, pyramidal cells, are organized into distinct patches across the layer and characteristically express the calcium protein *calbindin* (Varga et al., 2010). These neurons send a minor projection to the stratum lacunosum moleculare in CA1 (Kitamura et al., 2014), and have been reported to project to the contralateral mEC (Varga et al., 2010) (**Figure 1.1**).

Conversely, neurons in mEC layers V and VI, referred to as the mEC deep layers, receive projections from multiple cortical regions, in addition to dense feedback projections from the hippocampus and subiculum (Bonnevie et al., 2013; Kloosterman et al., 2003). These neurons subsequently project to the mEC superficial layers, thereby completing the entorhino-hippocampal loop (**Figure 1.1**). However, in addition to this major loop, multiple subloops also exist, such as a substantial projection from layer II stellate cells to layer Vb neurons in the mEC (Sürmeli et al., 2015).

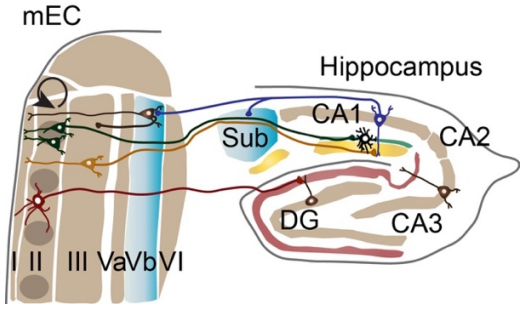

Figure 1.1. Anatomical projections between the mEC and the hippocampus.

Pyramidal (green) and stellate (red) cells in layer II project to the stratum lacunosum moleculare of CA1 and the outer molecular layer of the DG respectively, while pyramidal cells in layer III (yellow) only project to the stratum lacunosum moleculare of CA1. CA1 pyramidal cells and subicular cells (blue) both project to neurons in the mEC deep layers (brown), which subsequently project back to superficial layer cells.

Within the hippocampus, information flow is primarily unidirectional, with granule cells in the DG projecting to CA3 pyramidal neurons. The CA3 circuit is highly recurrent, with extensive projections from CA3 neurons to other CA3 pyramidal cells, in addition to projections to CA2 and CA1. CA1 neurons subsequently send most of their projections to the subicular complex and back to the mEC (**Figure 1.2**).

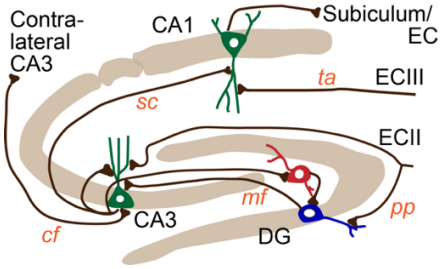

Figure 1.2. Excitatory projections within the hippocampus

Schematic depicting the trisynaptic loop (DG–CA3–CA1), but also describing the subloops and back-projections that exist within this network. Green, pyramidal cells, red, DG mossy cell, blue, DG granule cell. EC, entorhinal cortex, pp, perforant path, mf, mossy fibers, sc,schaffer collaterals, cf, commissural fibers, ta, temporoammonic pathway.

Representations of space within the mEC

Studies that have performed lesions or inactivation of the mEC have established a crucial role of the mEC in memory formation and spatial navigation (Gil et al., 2018; Hales et al., 2014; Parron et al., 2004; Robinson et al., 2017; Steffenach et al., 2005). Accordingly, there have been several reports that have examined the tuning properties of neurons within the medial entorhinal cortex with respect to spatial location. The earliest studies reported the existence of grid cells – cells that fire at repeated intervals to give rise to firing fields that strikingly form a hexagonal lattice (Hafting et al., 2005; Sargolini et al., 2006). Grid cells were first discovered in the rat mEC (Sargolini et al., 2006), but have since been found in other species including mice (Fyhn et al., 2008), bats (Yartsev et al., 2011) and humans (Jacobs et al., 2013). Apart from the mEC, they are

also present in areas of the parahippocampal cortex, but the highest proportion of grid cells are found in the dorsal region of mEC layer II (Sargolini et al., 2006). Grid cells that lie next to each other usually show the same grid spacing (distance between individual grid fields) and orientation, with grid vertices displaced by offsets (Hafting et al., 2005). Grid spacing specifically shows a distinct modularity along the mEC dorsal-ventral axis, with ventrally located cells having larger firing fields at each grid vertex, and greater spacing between the vertices (Brun et al., 2008; Stensola et al., 2012).

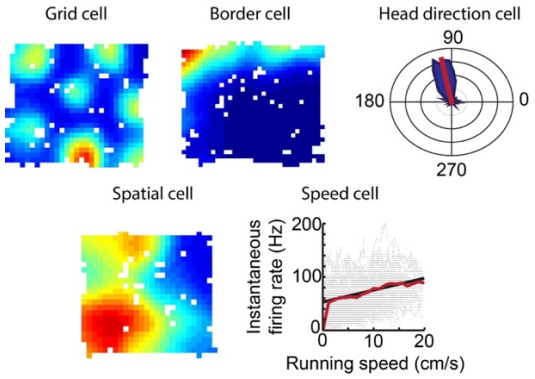

Figure 1.3. Functional cell types within the mEC

Examples of the functional cell types that co-exist within the mEC, including grid, border, head direction, spatial, and speed cells. The rate maps are color-coded from blue to red, with blue corresponding to minimum and red corresponding to maximum firing rate.

In addition to grid cells, there have now been various other functionally defined cell types described in the mEC. For example, head direction cells fire only when the animal is facing a particular direction (Taube et al., 1990; Winter et al., 2015), and are found dispersed across all layers of the mEC, in addition to in the thalamic nuclei, the pre- and para-subiculum and the subiculum (Giocomo et al., 2014; Taube, 2007). A third class of cells – boundary-vector or border cells are only active along a certain boundary of an environment (Solstad et al., 2008), and are also found across all layers of the mEC, in addition to the parahippocampal cortices. More recently, speed cells have also been described within the mEC – cells that either increase or decrease their

firing rates with changes in running speed (Hinman et al., 2016; Kropff et al., 2015). Within the mEC, these precisely tuned spatial cells are co-mingled with other cells that have broadly tuned, but reliable spatial tuning (Diehl et al., 2017). While the vast majority of studies have focused on examining tuning properties of mEC cells in the context of spatial location, there is now considerable evidence to suggest that these cells can be tuned to any other ongoing aspect of an experience, such as an auditory landscape, or time (Aronov et al., 2017; Kraus et al., 2015). These results suggest that together, with such diverse representations of any environment, neurons within this mEC are poised to generate a coherent, multimodal, internal representation that likely plays a role in generating memories for distinct events.

Spatially modulated cells in the hippocampus

Contrary to cells in the mEC, which tend to have multiple or dispersed spatial fields, neurons within the hippocampus, called 'place cells', fire only in restricted parts of the trajectory of an animal, thus enabling a network where sequences of place cells are constantly active in any environment (O'Keefe, 1976). Over 50 years of research has now unequivocally demonstrated that the hippocampus is required for tasks involving the formation of spatial memory, such as the Morris water maze, radial arm maze and spatial alternation (Beason-Held et al., 1999; Malkova and Mishkin, 2003; Morris et al., 1982; Racine and Kimble, 1965). Together, these results strongly suggest that place cell activity within hippocampal neurons plays a significant role in enabling memory formation. Corroborating this hypothesis for a more general role of hippocampal neurons supporting memory, place cells within the hippocampus are strongly influenced by diverse factors, including visual and tactile cues, reward expectation, novelty, direction of running, internal decisions, and metabolic state (Anderson and Jeffery, 2003; Bostock et al., 1991; Kennedy and Shapiro, 2009; Knierim, 2002; Leutgeb et al., 2005; Shapiro et al., 1997; Wood et al., 2000). Moreover, similar to the mEC, pyramidal cells within the hippocampus also display tuning to

features of an environment apart from space, such as elapsed time while running on a treadmill or auditory tones (Aronov et al., 2017; Kraus et al., 2013; MacDonald et al., 2011, 2013; Pastalkova et al., 2008). Therefore, the consensus is that rather than simply encoding space, the activity of populations of place cells also correspond to internal representations of any experience.

Theta oscillations arising from the medial septum

The theta rhythm is a 6-10 Hz brain oscillation detected by local field potential (LFP) recordings in the hippocampus and mEC during periods of mobility or REM sleep (Vanderwolf, 1969). The medial septal area (MSA) is considered to be critical for theta generation (Mitchell et al., 1982; Petsche et al., 1962), but the exact mechanism that gives rise to the theta rhythm is unknown. Individual cholinergic or GABAergic lesions of the MSA are insufficient to disrupt theta rhythm, but combined lesions completely abolish theta in the hippocampus (Brandon et al., 2011; Koenig et al., 2011; Mitchell et al., 1982; Mizumori et al., 1989; Wilson et al., 1978; Yoder and Pang, 2005). Moreover, combined GABAergic MSA lesions and lesions of the perforant path also abolish theta, while combined cholinergic MSA lesions and perforant path lesions are insufficient to cause a similar effect (Yoder and Pang, 2005). This finding that the perforant path can compensate during GABAergic, but not during combined lesions of the MSA, suggests that cholinergic projections of the MSA influence theta oscillations via the mEC. Additionally, cholinergic antagonist systemic scopolamine also abolishes the correlation of theta frequency with running speed (Newman et al., 2013). In contrast, manipulations of the MSA GABAergic cells reveal that activation of these cells at frequencies outside physiological theta can completely switch theta frequency to the frequency of stimulation (Bender et al., 2015; Zutshi et al., 2018b). This suggests that while the GABAergic cells directly control the frequency of theta, cholinergic cells contribute towards theta more subtly, possibly routing information through the mEC (Dannenberg et al., 2015).

Disruption of theta during memory tasks severely impairs performance, and it is believed that this deficit may arise due to inaccurate spatial and temporal firing of spatially modulated cells in the absence of theta (Mizumori et al., 1990; Winson, 1978). Likewise, the firing of almost all place cells, and most layer II grid cells is strongly coupled to theta oscillations (Hafting et al., 2005; O'Keefe and Recce, 1993). While theta oscillations are unlikely to be essential for spatial firing properties of neurons within the medial temporal lobe, inactivation of the MSA, which disrupts theta, also impairs grid cell spatial tuning without affecting properties of place cell firing (Brandon et al., 2011, 2014; Koenig et al., 2011).

Modulation of neuronal firing by theta oscillations

Neurons within the hippocampus and mEC are strongly modulated by theta oscillations, usually firing at a specific phase of the ongoing oscillations (Buzsáki, 2002; O'Keefe and Recce, 1993; Skaggs et al., 1996). This modulation of neural population is considered to play a key factor in coordinating spike timing between neurons, allowing information flow to be occur at a controlled pace. Indeed, windows of different phases of the oscillation allow different subpopulations of neurons to fire at these distinct phases, maintaining accurate firing relationships between populations of neurons (Buzsáki, 2002). One key phenomenon that arises from tightly regulated control of spike timing by theta oscillations is that of phase precession. Here, place cells always fire at a frequency slightly higher than local theta, causing each spike within a place field to occur at an earlier phase of theta (O'Keefe and Recce, 1993). This property has two benefits – (1) based on the phase at which the place cell is spiking, an animal can gather an estimate of where in the place field it is, and (2) for a series of overlapping place fields, the sequence of place fields according to the animal's path is maintained by the order in which spikes fire in relation to theta phase (**Figure 1.3**). Such sequential firing of neurons during behavior is thought to be critical to allow for spike-timing dependent plasticity between these neurons, a phenomenon that

unidirectionally strengthens the synaptic weights of cells firing in sequential order (Bennett et al., 1994; Guzman et al., 2016; McNaughton and Morris, 1987; Mishra et al., 2016; Nakazawa et al., 2002; Pfeiffer and Foster, 2015; Treves and Rolls, 1994). This mechanism thus organizes neuronal firing for past trajectories of an animal as 'assembly chains', supporting subsequent recall of the same trajectories for memory consolidation. Notably, both place cells in the hippocampus and grid cells in layer II of the mEC both show robust theta phase precession (Hafting et al., 2008; O'Keefe and Recce, 1993; Skaggs et al., 1996).

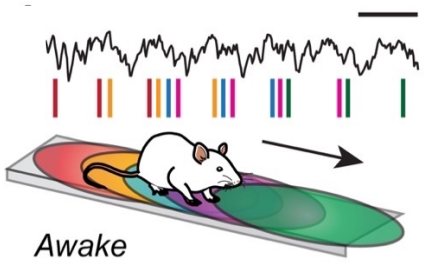

Figure 1.4. Theta oscillations coordinating place cell sequences in the hippocampus.

Phase precession, where progressive spikes of a place cell occur at earlier phases of the theta oscillation, sets up sequential firing of place cells (each color represents firing of one neuron) during movement. *Scale bar, 150 ms.*

The prevalence of theta-modulated, spatially restricted activity of neurons within the hippocampus and mEC suggests that there are distinct factors that play a role in determining when and how a certain neuron fires an action potential. One major class of factors can be attributed to the intrinsic properties of the neuron – its resting membrane potential, the concentration and type of ion channels present in its membrane, the shape and size of the neuron, the calcium binding proteins expressed etc. However, in addition to these cellular level properties, the key external factors that govern spike timing include the network anatomy, where the location and connectivity of presynaptic cells determine how and whether a certain set of afferent inputs can sufficiently depolarize the cell to fire an action potential. In addition to these connections, however, as described

previously, there seems to be an added layer of control of spike timing using theta oscillations that more tightly control the firing of populations of neurons, permitting more synchronous, and thus more effective depolarization. While network-dependent and oscillation-dependent control of spike timing are not mutually exclusive mechanisms, in this dissertation, these network-dependent mechanisms will be explored in the context of local recurrent circuits, involving relatively direct synapses between neurons. On the other hand, oscillation-dependent control of spike timing will be examined in the context of external control of spike timing, arising from distant brain regions, and likely involving complex interactions between a network of synapses across brain regions rather than within a local circuit.

Preview of the dissertation

In chapters II and III, the role of local networks in generating and sustaining functional firing properties of cells in the mEC is explored. As described, cells within the mEC, particularly in the superficial layers, display a wide variety of spatial tuning. However, it is unclear how such spatial tuning arises – whether the organization of networks within the mEC give rise to spatial firing, or whether these signals reach the mEC from long-range afferents. In chapter II, we first comprehensively describe local projections within the mEC, particularly within layers II and III, which contain most of the precisely tuned spatial cells. Notably, the tuning properties of grid cells and head direction cells become broader as we move along the dorso-ventral axis of the mEC (Giocomo et al., 2014; Stensola et al., 2012). For grid cells in particular, the spacing between grid nodes increases in distinct steps along the mEC dorso-ventral axis, and the properties of grid cells belonging to a particular spacing or module, are independent of grid cells in other mEC modules (Stensola et al., 2012). These results indicate that there might be some organization of the local projections within the mEC that correspond to different grid cell modules. To address this question, we performed cell-type specific retrograde tracing from layer II stellate and pyramidal cells, and

layer III cells at restricted locations along the dorso-ventral axis of the mEC and quantified the topography of local projections to these labelled cell types. Consistent with the hypothesis of a modular architecture within the mEC, we found that most local projections within the mEC occur along the radial axis of the mEC, with few projections between the dorsal and the ventral, and the medial and the lateral aspects of the mEC. These results suggest that these local networks within the mEC may play a role in determining the spatial firing properties, and especially govern the tuning widths of the functional cell types that exist within these networks.

In chapter III, we specifically test the hypothesis that local circuits within the superficial layers of the medial entorhinal cortex (mEC) contribute to the functional firing properties of cells found within the region, such as head direction, speed and grid cells. We recorded from cells in the mEC with transient, simultaneous optogenetic inhibition of most cells within the superficial layers. Consistent with several computational models, we found that local network inhibition led to small errors in the firing properties of grid cells, but not in speed and head direction cells. These results suggest that while local circuits within the mEC contribute to some aspects of spatial firing, such as grid cells, other spatial firing is solely inherited from long-range afferents to the mEC. Moreover, these afferents are sufficient to rapidly correct any errors that arise within the local computations, preventing cumulative and catastrophic errors in spatial firing properties.

In chapter IV, we shift gears and focus on neuronal firing in the hippocampus and pyramidal cells may be modulated by ongoing theta oscillations. Specifically, we optogenetically controlled the frequency of theta oscillations arising from the medial septum to address how hippocampal cells would respond to an artificially driven theta frequency. We found that during septal stimulation, the oscillation frequency of hippocampal neurons was accelerated beyond the stimulation frequency. These results provide evidence for cortical mechanisms that coordinate spike timing by using the firing of septal neurons as the base pacemaker, but further process this rhythmic input to generate an accelerated oscillation frequency in CA1 pyramidal neurons.

Finally, in chapter V, we provide an alternate hypothesis for the functional role of grid cell firing. We propose that populations of grid cells can give rise to a movement direction signal that can be used for updating internal representations during path integration and navigation. Moreover, such a signal can be read out on a longer time-scale in terms of sequences of progressively firing grid cells, but also within a single theta cycle using phase precessing grid cells. Such a functional readout is the perfect example of how both mechanisms that control spike firing discussed in this dissertation – a local network dependent rate code and an oscillation dependent temporal code – can be used in the same network of neurons to convey meaningful information during behavior.

II.

Layer Specific Characterization of Local Projections within the Medial Entorhinal Cortex

"To develop a complete mind: Study the art of science; study the science of art. Learn how to see. Realize that everything connects to everything else."

— Leonardo Da Vinci

Abstract

The medial entorhinal cortex (mEC) receives multimodal inputs from several cortical regions and its superficial layers (layers II and III) are the primary source of excitation to the hippocampus. In addition to extensive projections from the deep to the superficial mEC layers, there are also highly recurrent local projections within and between all layers of the mEC. These local connections become particularly relevant with the observation that mEC cells have unique functional properties corresponding to combinations of grid, head direction, border, speed, and other context-dependent spatial tuning. Moreover, the spatial scale of some of these functional cell types, such as grid and head direction cells, increases in modular steps along the dorso-ventral axis of the mEC (Giocomo et al., 2014; Stensola et al., 2012), suggesting some degree of topographical organization within the mEC. In this study, we took advantage of a wide range of layer specific mouse lines, corresponding to the two major excitatory cell types in layer II – pyramidal and stellate cells, and to cells in LIII, LVa and LVI, and utilized cell type specific anterograde and retrograde viral tracing strategies to dissect and quantify local projections between the mEC layers. On performing retrograde tracing from sub-populations of layer II pyramidal cells and layer III cells at various depths along the mEC, we found that we could confirm several previous reports on the connectivity between these cell types and determined that superficial layer presynaptic projections

arise from cells within modules along the same dorsoventral and mediolateral level. We are currently performing similar experiments to determine the organization of local projections to layer II stellate cells. Cells from the mEC deep layers, specifically from layers Va and VI, only weakly projected to the superficial layers of the mEC, suggesting that layer Vb neurons act as the primary source of projections from the deep to superficial layers. Instead, we report a previously undescribed projection arising from mEC layer VI neurons to the CA2/ CA3 region of the hippocampus. Eventually, such a comprehensive characterization of deep to superficial layer projections, as well as of recurrent superficial layer projections, could provide more insight into the circuits that support diverse functional cell types in the mEC.

Introduction

Neurons in the medial entorhinal cortex (mEC) belong to segregated functional classes such as grid cells, border cells, speed cells or head-direction cells (Giocomo et al., 2014; Hafting et al., 2005; Kropff et al., 2015; Sargolini et al., 2006; Solstad et al., 2008). Of all these functional cell types, grid cells have the most striking firing patterns, with field that form a periodic, hexagonal lattice. While first discovered in rats (Hafting et al., 2005), grid cells have now been observed in mice (Fyhn et al., 2008), bats (Yartsev et al., 2011), non-human primates (Killian et al., 2012), and humans (Jacobs et al., 2013). Grid cells are also present in the parasubiculum and subiculum (Boccara et al., 2010), and in the deep layers of the mEC, but the highest proportion of grid cells are found in mEC layer II (Sargolini et al., 2006). Especially within layer II, grid cells are modularly organized along the dorsoventral axis of mEC with increasing grid spacing and grid field size in each module (Barry et al., 2007; Brun et al., 2008; Gu et al., 2018; Stensola et al., 2012). Interestingly, the increase in grid spacing occurs in steps by a factor of ~1.4 with grid cells of different spacing lying in broadly overlapping anatomical modules (Stensola et al., 2012) (**Figure 2.1A**). Most environment manipulations that lead to changes in the alignment, spacing, rates and

orientation of grid cells cause correlated changes to grid cells within a module, but unrelated to those occurring within other modules, suggesting that grid cell functional modules are largely independent of each other (Carpenter et al., 2015; Fyhn et al., 2007; Gu et al., 2018; Rowland and Moser, 2014; Stensola et al., 2012).

In addition to changes in grid cell spacing, there are several other gradients that have been reported along the dorsoventral axis of the mEC. For example, in layer III of the mEC, there is a gradual increase in the average width of the directional firing field of head direction cells (Giocomo et al., 2014). Consistent with these gradients in functional firing, the intrinsic properties of layer II stellate cells also differ from dorsal to ventral, with changes in the I_h currents leading to differences in their membrane potential oscillations and resonant frequency (Giocomo and Hasselmo, 2008; Giocomo et al., 2007). These differences were found to become abolished upon knockout of the HCN1 subunit channel, suggesting that these cellular level gradients might arise from an ion channel expression gradient along the dorsoventral axis (Giocomo and Hasselmo, 2009). However, complete or selective knockouts of HCN1 channels, while leading to a universal increase in grid scaling, maintain the dorsal to ventral increase in grid spacing (Giocomo et al., 2011a; Mallory et al., 2018). Together, these results suggest that HCN1-dependent cellular resonance gradients cannot explain the independent grid cell modules. Previous studies have also reported a decreasing gradient in inhibitory synapses arising from parvalbumin positive interneurons, with a corresponding increase in calbindin expression along the dorsoventral axis of the mEC (Beed et al., 2013; Fujimaru and Kosaka, 1996)

Instead of arising from cellular properties of neurons, gradients in functional firing along the dorsoventral axis of the superficial layers of mEC may arise from anatomically segregated modules that have few projections between each other. However, previous studies examining the local connectivity of the superficial layers of mEC have predominantly patched from cells in close proximity to each other, performed glutamate uncaging in slices, or performed photostimulation –

and results from these independent studies have been incomplete and conflicting (Couey et al., 2013; Dhillon and Jones, 2000; Fuchs et al., 2016; Pastoll et al., 2013; Sürmeli et al., 2015; Winterer et al., 2017) (results summarized in **Figure 2.1B**). While initial studies reported that layer II stellate cells are predominantly connected with inhibitory cells (Couey et al., 2013; Dhillon and Jones, 2000; Pastoll et al., 2013), more recent studies have identified direct excitatory connectivity between subsets of layer II stellate cells (Fuchs et al., 2016; Winterer et al., 2017). Similarly, it is

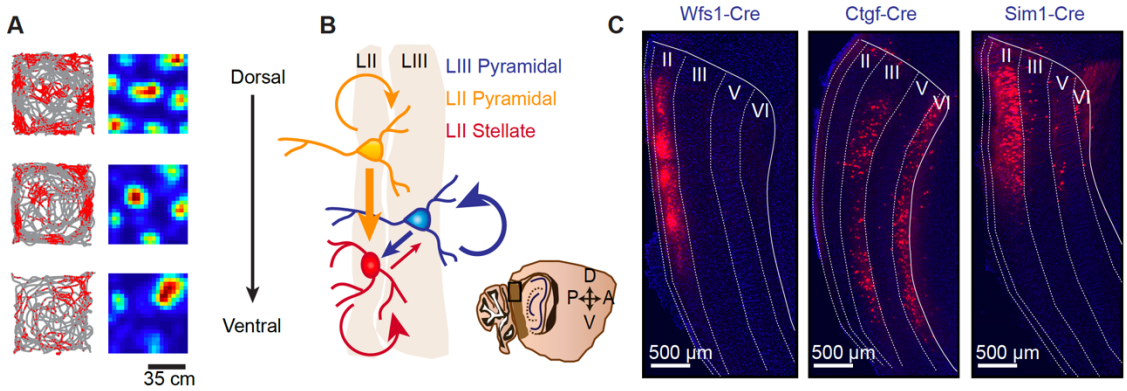

Figure 2.1. Connecting anatomy to grid cell modules.

(A) Three distinct grid cells, each recorded at different depths along the dorsoventral axis of the mEC. The spacing between grid fields increases as we move further ventral along the mEC. *Scale bar*, 35 cm. (B) Schematic summarizing known projections between the predominant excitatory cell types within the superficial layers of the mEC. (C) Sagittal sections from three mice injected in the mEC with a Cre dependent AAV expressing the red fluorophore tdTomato. In Wfs1-Cre mice, Cre expression is restricted to layer II pyramidal cells, observable as distinct patches along the dorsoventral extent of mEC layer II. In Ctgf-Cre mice, Cre expression was predominantly observed scattered in subsets of layer III cells, and also in cells in layer VI of the mEC. In Sim1-Cre mice, Cre expression was restricted to layer II stellate cells, but also spread out to small subsets of cells in layers III and V of the mEC. *Scale bar, 500 µm.*

unclear how layer II stellate and pyramidal cells are connected to each other, but a recent study reported dense layer II pyramidal to stellate connectivity, but sparse projections in the reverse direction (Couey et al., 2013; Fuchs et al., 2016; Sürmeli et al., 2015; Winterer et al., 2017). Moreover, while cell types and local projections have been extensively examined within layer II, layer III predominantly consists of pyramidal cells that have not been further subdivided by

physiological criteria (Canto and Witter, 2012). Cells in layer III have dense axon collaterals that predominantly target the superficial cell layers, where dendrites of layers II, III and V are located (Alonso and Klink, 1993; Beed et al., 2010; Canto and Witter, 2012; Dickson et al., 1997; Fuchs et al., 2016; Gloveli et al., 1997; Kumar et al., 2007; Winterer et al., 2017). Connectivity from layer III cells to other cells in the superficial layers has predominantly been characterized by patch-clamp recordings in slices, and layer III cells have been reported to project densely to other cells in layer III, along with projections to stellate cells in layer II (Couey et al., 2013; Fuchs et al., 2016; Winterer et al., 2017). In addition, cells in layer III also densely project to the contralateral hemisphere (Tang et al., 2015).

One key limitation of all these above described studies is that their method of slice recording restricted the estimation of the connectivity of neurons to those in proximity to their recording area. For a thorough understanding of how local mEC circuits might contribute to functional cell types, and specifically whether the dorsoventral gradient observed in the functional firing properties of grid cells and head direction cells may be dependent on anatomically defined modules within the mEC, we require a definite description of the extent and topography of connections between cells in the superficial layers, including over distances that exceed those that can be examined in slice experiments. In this paper, we used transgenic mouse lines that selectively target pyramidal cells in layer II, pyramidal cells in layer III, and stellate cells in layer II to express the Cre recombinase protein in these cell types (**Figure 2.1C**). Using cell-type specific virus-mediated retrograde tracing, we targeted different positions along the dorsoventral axis of the mEC such that only few starter cells are labelled in each injection. Next, for each cell type, we quantified the projections from cells in the mEC superficial layers to the labelled starter cells and compared these inputs across different cell types. In addition, we also used layer Va and layer VI specific mouse line to compare the inputs and outputs from the deep layers of the mEC versus the superficial layers.

Methods

Approvals: All animal experiments were approved by the University of California, San Diego Institutional Animal Care and Use Committee and conducted according to National Institutes of Health guidelines.

Animals: Wfs1-creERT2 and Ctgf-2A-dgCre-D mice were obtained from The Jackson Laboratory [B6.Cg-Tg(Wfs1-cre/ERT2)2Aibs/J, Stock No.:009614 and B6.Cg-Ccn2$^{tm1.1(folA/cre)Hze}$/J, Stock No.: 028535, respectively]. Sim1-Cre mice and Rbp4-Cre mice were obtained from the Mutant Mouse Resource and Research Centers [Tg(Sim1-cre)KJ21Gsat/Mmucd, Stock No.: 034614-UCD and Tg(Rbp4-cre)KL100Gsat/Mmucd, Stock No.: 031125-UCD. The Rbp4-Cre mice were generously provided by Prof. Jeffry Isaacson]. Importantly, the Wfs1-Cre, Ctgf-Cre and Rbp4-Cre mice were mated with C57BL6/J from the Jackson Labs, while Sim1-Cre were mated with Crl:CD1 mice from Charles River Laboratories.

For viral tracing procedures, we used heterozygous mice, weighing between 20-30 g, and at least 8 weeks old, for each genotype, with equal numbers of males and females. Importantly, we observed no differences in the projection patterns of LIIP cells between male and female. To obtain Cre expression in Wfs1-Cre mice, mice were given three IP injections of tamoxifen (0.25 mg/g body weight, Sigma-Aldrich, T5648) over 5 days. The tamoxifen was prepared as 20 mg/ml in corn oil (Sigma-Aldrich, C8267) and stored at -20 °C (400 mg tamoxifen in 20 ml corn oil). To obtain Cre expression in Ctgf-Cre mice, the mice were given a single IP injection of trimethoprim (170 µg/g body weight, Sigma-Aldrich, T7883). The trimethoprim solution was prepared fresh prior to injection as 50 mg/ml dissolved in DMSO solution (25 mg trimethoprim in 500 µl DMSO, Sigma-Aldrich, D4540). The mice were housed on an inverse 12 hr light/dark cycle (lights off at 8 am). Mice were provided food and water *ad libitum* and were housed in groups (maximum 5 per cage) before and after surgery. Genotyping was performed by Transnetyx using real-time PCR.

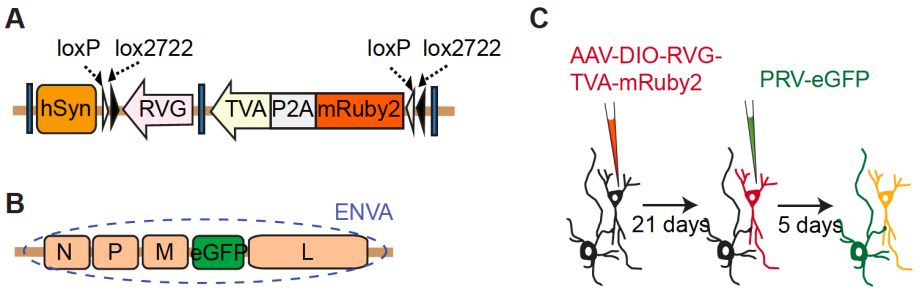

Figure 2.2. Schematic of viral constructs and infection pattern.

(A, B, C) The AAV-DJ-DIO-RVG-TVA-mRuby2 expresses an avian receptor (TVA) and rabies virus glycoprotein (RVG, G-protein) in Cre expressing cells, labelling them red. A subsequent injection of G-protein deleted rabies virus pseudotyped with the TVA binding ligand (ENVA) allows specific uptake in the Cre+ cells (now yellow). This virus is then retrogradely transported by one synapse (green) using the RVG present in starter cells (yellow).

Injection of viral vectors: All mice were anesthetized with isoflurane (1.5-2.5 % in O_2) and mounted in a stereotaxic frame (David Kopf Instruments, Model 1900). Once unresponsive to toe-pinch, an incision was made, and the skull was leveled to bring bregma and lambda to the same plane. A unilateral craniotomy was made over the mEC (+0.2 AP from the transverse sinus, +3.75 ML from lambda) and a glass pipette containing the virus was slowly lowered into the brain at a 6° angle (towards anterior). A single virus, AAV-hSyn-FLEX-mRuby2-T2A-TVA-RVG (provided by Dr. Byung Kook Lim, titer: ~1.5 x 10^{14} diluted in 1x PBS 1:10, packaged into AAV2/DJ serotypes) was injected at a single location (either -1.8 DV, -1.3 DV, or -0.9 DV from the surface of the brain) with ~150 nl volumes. The pipette was left in place for 5 minutes at the injection site, and then slowly brought out of the brain. The injection was administered at a flow rate of 100 nl/min using a microsyringe pump (World Precision Instruments, UMP3 UltraMicroPump). This construct was allowed to express for at least three weeks before a second pseudotyped rabies virus (provided by Dr. Byung Kook Lim, G protein deleted rabies virus pseudotyped with the TVA receptor, ENVA) injection was performed at the same location. Following 5 days for rabies expression, the mice were perfused (**Figure 2.2**).

Tissue processing and immunohistochemistry: Anesthetized mice were perfused with cold saline solution (0.9 %) followed by cold pre-made 4 % paraformaldehyde in PBS solution (Affymetrix USB). Brains were post-fixed for 24 hours in 4 % paraformaldehyde at 4°C and then transferred to PBS solution and subsequently sagittally sectioned (40-50 µm) on a vibrating blade microtome (Leica, VT1000 S). The sections were either mounted directly on electrostatic slides or transferred to 1x PBS for immunohistochemistry. Slides were coverslipped with DAPI Fluoromount-G (Southern Biotech, 0100-20) and imaged using a virtual slide microscope (Olympus, VS120).

For sections used for immunohistochemistry, prior to the addition of primary antibodies, the slices were blocked for 1 hour at room temperature (RT) with a blocking solution comprising 10 % horse serum (HS), 0.2 % bovine serum albumin (BSA) and 0.05 % Triton-X in 1x PBS. Slices were incubated overnight at 4 °C with primary antibodies dissolved in a carrier solution made with 1 % HS, 0.2 % BSA, and 0.05 % Triton-X in 1x PBS. After overnight incubation and 4 washes for 10 min each with 1x PBS, the slices were incubated for at least 2 hours at RT with secondary antibodies in carrier solution. Next, the slices were washed four times with 1x PBS, mounted on glass slides and coverslipped with DAPI Fluoromount-G. The following primary antibodies were used, mouse anti-reelin (Millipore Cat# MAB5364, RRID:AB_2179313, 1:1000), mouse anti-reelin (MBL International Cat# D223-3, RRID:AB_843523) and rabbit anti-Wfs1 (Proteintech Group Cat# 11558-1-AP, RRID: AB_2216046, 1:1000). All secondary antibodies (AlexaFluor488 anti-mouse, AlexaFluor405 anti-rabbit, AlexaFluor488 anti-rabbit) were obtained from ThermoFisher Scientific. Sections were imaged using a virtual slide microscope (Olympus, VS120) and higher magnification images were obtained from a confocal microscope using 10x, 20x or 60x magnification lenses (Olympus FluoView, FV1000).

Fluorescence quantification: Sections containing the ipsilateral and contralateral mEC of mice were imaged using a virtual slide microscope (Olympus, VS120) at 10x magnification. For each animal, the sections were imaged with three to four laser wavelengths – 405 nm (blue), 495 nm (green), 532 nm (red) and 647 nm (far-red). Sagittal sections separated by ~150 μm (6-8 sections per mouse) were used to quantify the topography of projections within each mouse and analyzed using Fiji ImageJ (Schindelin et al., 2012). Within each section, ten non-overlapping regions of interest (ROIs) were defined along the dorsoventral axis of the mEC, five within layer II and five within layer III of the mEC. Within each block, the number of starter cells (yellow) and presynaptic cells (green) was manually counted and normalized by the total number of cells found across all blocks within the relevant layer (**Figure 2.2**).

Results

Layer II pyramidal cells receive columnar projections from other layer II and III cells

Wfs1-Cre mice have previously been reported to show restricted Cre expression in layer II pyramidal neurons (Kitamura et al., 2014; Sürmeli et al., 2015; Zutshi et al., 2018a). Therefore, we used this mouse line to generate a topographical map of all superficial layer mEC projections to these layer II pyramidal cells. In order to determine the distribution of presynaptic cells to layer II pyramidal cells within a single grid cell module, we performed small injections along varying dorso-ventral coordinates of the mEC of Wfs1-Cre mice. We injected an AAV containing the construct AAV-hSyn-FLEX-mRuby2-T2A-TVA-RVG, which led to the expression of the red fluorophore mRuby2, in addition to the avian receptor TVA, and the rabies virus glycoprotein, RVG, specifically in cells expressing the Cre recombinase protein. Following sufficient time for the AAV to express, we injected a second virus – a replication deficient G-protein deleted rabies virus, pseudotyped with the TVA binding protein ENVA. This strategy therefore selectively allowed uptake of the rabies virus in Cre expressing cells, labelling the “starter” cells yellow. Due

to the complementation of the RVG protein from the initial AAV, this rabies virus could successfully jump one synapse up to label all presynaptic cells to the starter cells, in the process labelling them green (Callaway and Luo, 2015; Wickersham et al., 2007) (**Figure 2.2**).

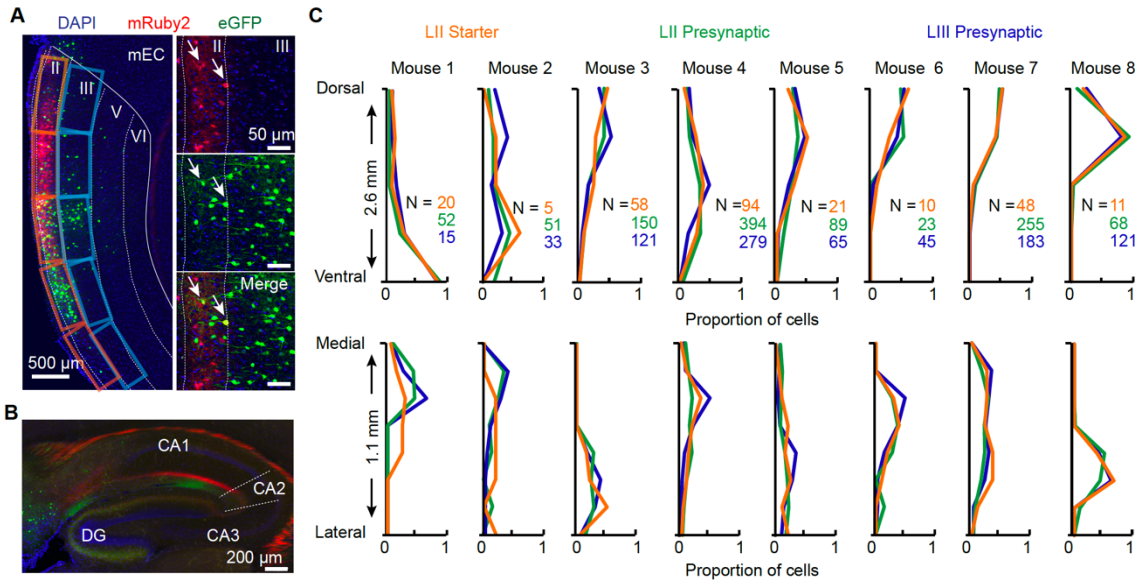

Figure 2.3. Layer II pyramidal cells receive projections from other layer II and III cells.

(A) Representative section from an animal where starter cells were primarily restricted to the middle portion of the mEC. The total number of yellow starter cells in layer II and green presynaptic cells in layers II and III were counted for each ROI drawn over the section. *Arrows*, layer II pyramidal starter cells. (B) Green axon collaterals from presynaptically labelled layer II stellate cells to DG and CA3, and presynaptically labelled layer III cells to CA1. (C) Summary of the topography of projections across 8 mice. *Top row,* Proportion of layer II starter cells along the dorsoventral axis of the mEC (*yellow*) within each ROI, summed across all sections. For each animal, both presynaptic layer II (*green*) and layer III (*blue*) cells were most prominent at the same depth as where the starter cells were the most prevalent. *Bottom row,* Proportion of layer II starter cells along the mediolateral axis of the mEC (yellow) within each sagittal section, summed across all ROIs. Most presynaptic cells, especially those in layer III were found more medial to the starter cells. The total number of starter and presynaptic cells is provided for each animal.

On targeting different dorso-ventral sites of the mEC of Wfs1-Cre mice we observed that most layer II pyramidal cells receive dense inputs from mEC LIII pyramidal and from LII stellate cells, but sparse inputs from the deep layers (layer V, VI) of the mEC (**Figure 2.3A, B**). The inputs to a single layer II pyramidal cell patch arose from other LII pyramidal cells within the patch, layer

II stellate cells surrounding the patch, and from layer III cells at the same dorsoventral level. In addition, the axon terminals of the presynaptically labelled cells could be clearly observed in the hippocampus, which confirms the identity of the presynaptic neurons based on the following considerations (**Figure 2.3B**). For example, layer II stellate cells are known to terminate in the outer molecular layer of the dentate gyrus (DG) and CA3 (Witter and Amaral, 1991; Witter et al., 1988), and the presence of green, but not red fluorescence within these layers confirmed that stellate cells in layer II were presynaptically labelled. Similarly, we observed green but not red axon collaterals at the proximal and distal ends of the stratum lacunosum moleculare of CA1, consistent with the known anatomical projections of mEC layer III cells (Witter and Amaral, 1991; Witter et al., 1988). Conversely, we observed red-labelled fibers in the zone within the CA1 where layer II pyramidal cells have been reported to terminate (Kitamura et al., 2014; Sürmeli et al., 2015; Zutshi et al., 2018a). Finally, we selected eight mice (3 males, 5 females) in which the injections were satisfactorily targeted to layer II pyramidal cell in 1-2 patches and quantified the topography of projections within each mouse (see Methods). Across all the mice, we observed that in addition to maintaining their dorsoventral topography, local projections were shifted along the radial axis of the mEC, which was visible as an increased number of presynaptic cells more medial to the injection site on these sagittal sections (**Figure 2.3C**).

Layer II stellate cells appear to receive sparse projections from nearby mEC cells

We repeated the same experimental procedure described for layer II pyramidal cells in Sim1-Cre mice, which selectively express Cre recombinase protein in layer II stellate cells (Sürmeli et al., 2015). Currently the data are preliminary, and obtained from 2-3 mice, but with these limited sample sizes we observed sparse labelling of presynaptic cells within the mEC despite several starter stellate cells labelled by the virus (**Figure 2.4A**). These results could be confirmed again by examining the projections of these cells in the hippocampus, where the predominant axons labelled

in green and red terminated in the DG and CA3, consistent with layer II starter cell expression, but sparse layer II pyramidal and layer III cells infected by the rabies (**Figure 2.4B**). This discrepancy with previously reported data could be attributed to several reasons – first the Sim1-Cre line is bred as a different strain to the more commonly used and reported C57BL6. However, in addition to strain differences, there may be limitations with the rabies virus technique employed for this set of preliminary data (see Discussion). Further experiments are currently being performed to confirm and verify these results.

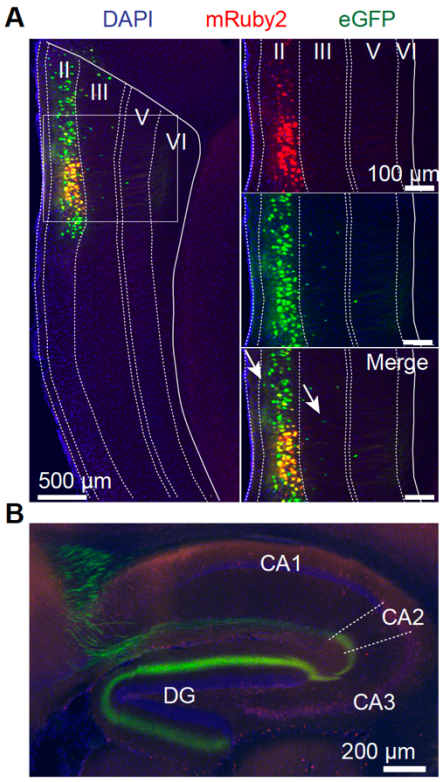

Figure 2.4. Layer II stellate cells receive sparse projections from within the mEC

(A) Representative section from a Sim1-Cre animal where starter cells were primarily restricted to the dorsal portion of the mEC, labelling layer II stellate cells. Very few presynaptic cells were observed (*arrows)* (B) Green merged with red axon collaterals from starter layer II stellate cells to DG and CA3, and a lack of labelling of the fiber terminals of the other cell types in mEC superficial layers. This confirms that few presynaptic cells were labelled in this animal.

Layer III pyramidal cells receive dense projections from layer II stellate and other layer III cells

Finally, we repeated the same procedure in Ctgf-Cre mice, that sparsely labelled subsets of neurons within layer III of the mEC. On targeting different dorso-ventral depths of the mEC of these mice, we observed that layer III neurons pyramidal cells receive dense inputs from other layer III cells, from layer II stellate cells, and sparse inputs from the mEC deep layers (**Figure 2.5A**). For injections targeted to a certain depth along the dorsoventral axis of the mEC, presynaptic cells

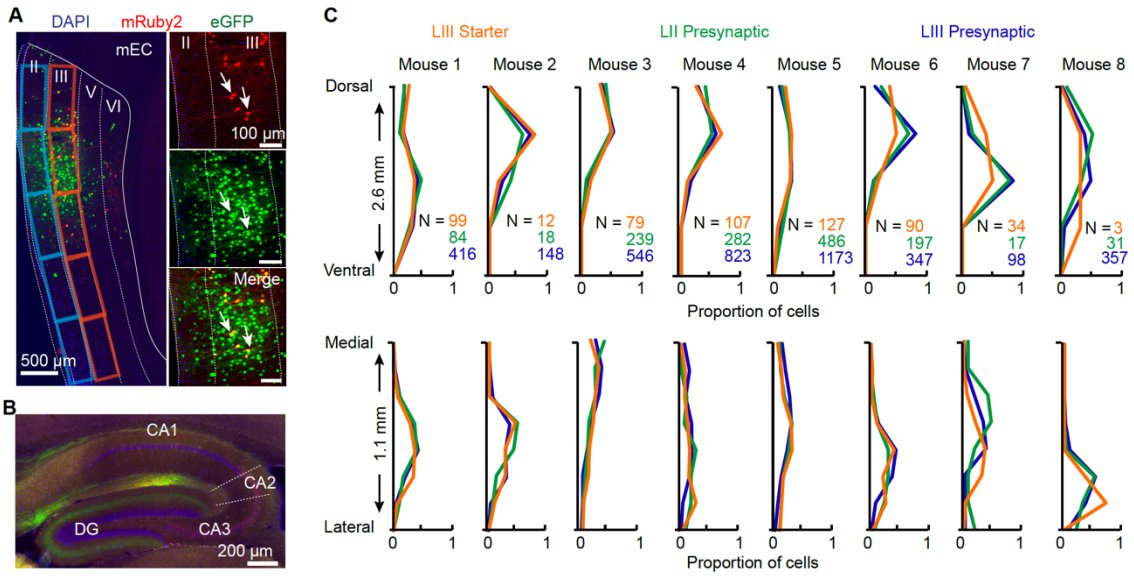

Figure 2.5. Layer III pyramidal cells have extensive recurrent connections.

(A) Representative section from a Ctgf-Cre animal where starter cells were restricted to layer III. The number of yellow starter cells in layer III (*arrows*) and green presynaptic cells in layers II and III were counted for each ROI. Note the high convergence of presynaptic cells in layer III to a small population of layer II starter cells. (B) Green and red overlapping axon collaterals from starter layer III cells terminating in the stratum lacunosum moleculare of CA1. Green axon fibers consistent with the performant path terminating in the DG and CA3 were also observed, suggesting that layer II stellate cells project to layer III neurons. (C) Summary of the topography of projections across 8 mice. *Top row,* Proportion of layer III starter cells along the dorsoventral axis of the mEC (*yellow*) within each ROI, summed across all sections. For each animal, both presynaptic layer II (*green*) and layer III (*blue*) cells were most prominent at the same depth as where the starter cells were the most prevalent. *Bottom row,* Proportion of layer II starter cells along the mediolateral axis of the mEC (yellow) within each sagittal section, summed across all ROIs. The total number of starter and presynaptic cells is provided for each animal. Note the high convergence of layer III starter to layer III presynaptic cells, indicating a densely recurrent local circuit.

were observed in proximity to the injection site. The axon terminals of the presynaptically labelled cells terminated in the outer molecular layer of the DG and CA3, and the stratum lacunosum moleculare of CA1, confirming that layer II stellate and other layer III pyramidal cells project to layer III pyramidal cells (**Figure 2.5B**). Similar to the analysis performed for Wfs1-Cre mice, we used eight mice (2 males, 6 females) in which the injections were targeted to small populations of layer III pyramidal cells. We again observed that the local projections maintain their dorsoventral and mediolateral topography (**Figure 2.5C**). Notably, the layer III projections were highly convergent, with multiple presynaptic layer III cells projecting to a few starter cells.

Layer VI neurons in the mEC project to the CA2/ CA3 region of the hippocampus

As mentioned previously, Cre expression in the Ctgf-Cre mice was not restricted to layer III, and when performing AAV injections, we often observed expression in layers Va and VI of the mEC. In subsets of mice where only layer Va and VI neurons were infected, we observed several presynaptic cells only in layer Va, but sparse expression in the superficial layers, further confirming that the dense presynaptic cells observed upon layer III injections was not a result of Cre expression also in the mEC deep layers (**Figure 2.6A**). Surprisingly, we observed dense red axon collaterals in the stratum lacunosum moleculare of CA2 and CA3 within these animals with layer Va and VI expression (**Figure 2.6B**). While there have been few reports of a small subset of deep layer mEC cells projecting to the hippocampus, it is widely assumed that these projections are sparse and not significant (van Groen et al., 2003; Witter and Amaral, 1991). To further examine this previously undescribed projection, we used an anterograde AAV virus expressing the red fluorophore mRuby2 in cell bodies and axons, and a synaptophysin-tagged-eGFP at the synapse terminals in a Cre dependent manner (**Figure 2.6C**). First, we used a mouse line, Rbp4-Cre, that selectively targeted layer Va neurons within the mEC, to determine if this hippocampal projection was specifically arising from these cells. We observed synapses from layer Va neurons in layer VI of the mEC, in

addition to previously reported extra-hippocampal targets such as the striatum and retrosplenial cortex (Ohara et al., 2018; Sürmeli et al., 2015), but found no projections to the hippocampus (**Figure 2.6D, E**). On the contrary, when we targeted the same virus to layer VI neurons within the mEC of Ctgf-Cre mice, we found dense synapses terminating in CA2 and CA3, consistent with a novel projection arising from layer VI mEC neurons to the hippocampus (**Figure 2.6F, G**).

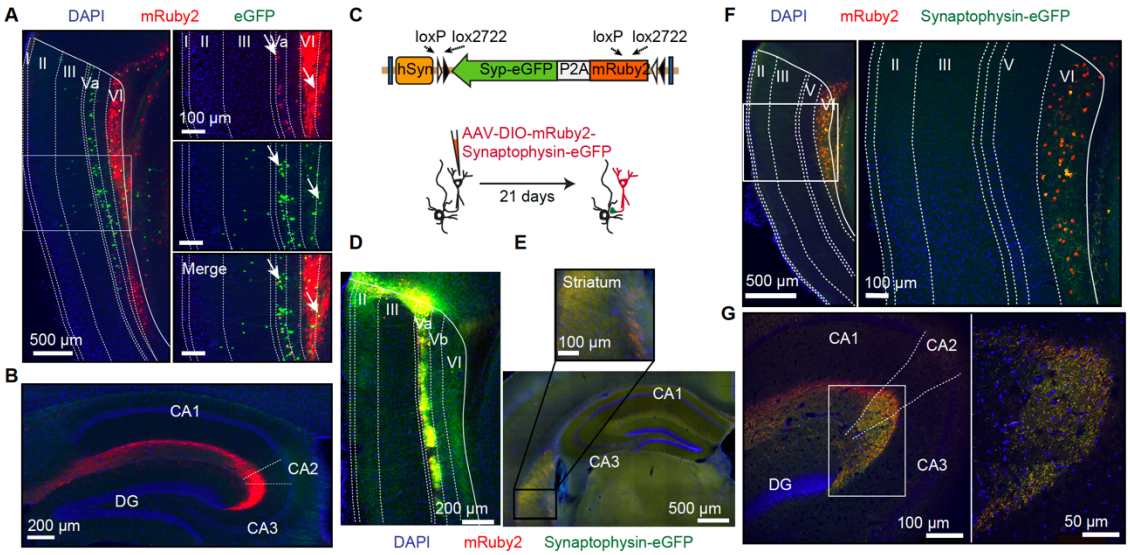

Figure 2.6. mEC Layer VI neurons project to CA2 and CA3 in the hippocampus.

(A) Representative section from a Ctgf-Cre animal. Cre expression was observed in this mouse line in layer III and the deep layers of the mEC, specifically layers Va and VI. In a subset of mice, we performed targeted injections to the deep layers of the mEC. Starter cells were observed in both layers Va and VI (*arrows*), and green presynaptic cells were found primarily in layer Va, but not in the superficial layers. (B) Red axon collaterals from AAV infected layer Va and VI cells were observed to terminate in the stratum lacunosum moleculare of CA2 and CA3. (C) Schematic of virus construct used to perform anterograde tracing from mEC deep layer cells. (D) Representative section from an Rbp4-Cre mice injected with an anterograde virus. AAV expression was restricted to layer Va neurons, and dense synapses (green) arising from these cells were observed in layer VI within the mEC. (E) No synapses were observed in the hippocampus from layer Va neurons. However, as previously reported in literature, synapses were observed in other brain regions such as the striatum. (F) Representative section from a Ctgf-Cre mouse injected with an anterograde virus. AAV expression was restricted to layer VI neurons, and sparse synapses were observed from these cells within the mEC. (G) The axonal projections observed in the hippocampus in **Fig 2.6B** was observed again upon selectively targeting layer VI neurons. Layer VI neuronal projections extended to the CA2 and CA3a regions, where they formed dense synapses (*green*).

Discussion

In this paper, we employed cell type specific viral tracing to dissect the projections between layer II pyramidal, layer II stellate and layer III cells in the superficial layers of the mEC. To avoid confounds due to the presence of Cre expression in the deep layers in both the Ctgf-Cre and Sim1-Cre mice, we decided to only focus on presynaptic projections either within the superficial layers or within the deep layers. Consistent with previous reports, we determined that layer III cells are highly recurrently connected to each other (Winterer et al., 2017), and contrary to previous results (Winterer et al., 2017), we report that they project densely to layer II pyramidal cells. We did not observe presynaptic layer III neurons on the contralateral hemisphere but found red fibers from labelled layer III neurons traveling to the contralateral hemisphere, suggesting that the layer III neurons that receive contralateral layer III projections may correspond to a specific subset that we could not label with our Ctgf-Cre mouse line. Furthermore, we observed that layer II stellate cells project to layer II pyramidal cells in addition to layer III neurons and are currently determining which cells are presynaptic to layer II stellate cells (**Figure 2.7)**. Importantly, all of these local projections occurred along the radial axis of the mEC, with few projections between the dorsal and ventral, or medial and lateral ends of the mEC. When we used the same retrograde virus tracing strategy to label the deep mEC layers, we found sparse projections arising from the superficial layers to the deep layers but observed that neurons in layer Va project to neurons in mEC layer VI. In addition, we observed that neurons in the mEC layer VI send a previously unreported projection to the CA2/ CA3 region of the hippocampus. We propose that this projection may play an important role in modulating several physiological properties that are known to be selectively dependent on this region of the hippocampus, e.g., the initiation of sharp wave ripples (Buzsáki, 2015; Oliva et al., 2016).

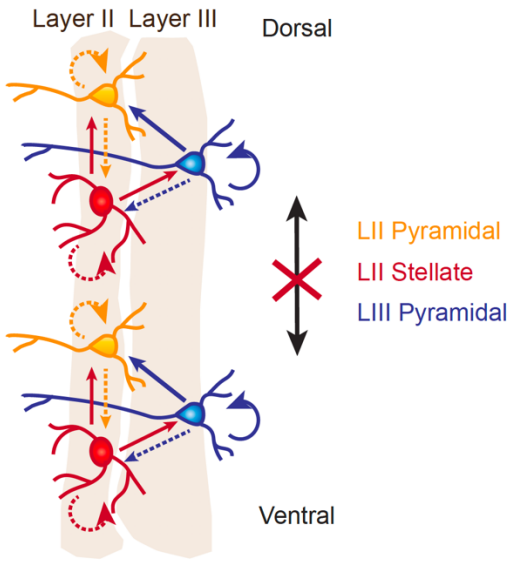

Figure 2.7. Updated schematic summarizing the topography and identity of projections between cell types within the superficial layers of the mEC

Several projections between different cell types were confirmed using cell type specific retrograde tracing (*solid arrows*). We are currently examining other projections, especially with respect to layer II stellate cells (*stippled arrows*). Importantly, we observed module-specific projections between these cell types, such that there was little dorsoventral and mediolateral connections within the mEC.

Notably, there are several reasons why previous patch recording data may not match completely with the data we have obtained from viral tracing. In cases where we observed projections that are previously unreported, e.g., layer III pyramidal to layer II pyramidal cells, these discrepancies may arise from the angle at which the slices were cut, and whether axonal fibers were retained in these slices. Additionally, estimating connectivity using paired recordings in slice often leads to an underestimation of actual connectivity. Another possible cause for discrepancy is the observation that for all the mouse lines, especially the Sim1-Cre and Ctgf-Cre mice, there is some degree of Cre expression in mEC layers outside the layer of interest. While targeted mini-injections helps address this issue, some observed presynaptic cells may arise from starter cells outside of the layer of interest.

For cases where projections have been reported in slice, e.g., layer III pyramidal to layer II stellate cells, but we fail to observe these using viral tracing, the issues likely correspond to limitations with the transgenic mouse lines or the rabies mediated viral tracing method. First, especially in case of the layer II stellate cells, the mouse line we are using belongs to a different strain from that of the other cell types. This could lead to some variation in the projection patterns observed. Second, the rabies virus is known to show a certain degree of tropism and differential uptake depending on the nature of the synapse (Callaway and Luo, 2015). Therefore, some synapses may more preferentially be observed using this method over others.

Finally, there are some other major considerations to bear in mind when interpreting these results. First, there may be some amount of leak TVA expression in non Cre dependent manner that may confound several of these results (Callaway and Luo, 2015; Miyamichi et al., 2013; Seidler et al., 2008; Wall et al., 2010). To address these issues, we are currently confirming the level of leak by repeating the same experiments in wild type mice. Second, the levels of red fluorescent protein from the AAV are generally lower than the green fluorescent protein from the rabies, sometimes making a 'starter' cell appear as a presynaptic cell. Therefore, the counting estimates of 'starter' versus 'presynaptic' cells are only approximate rather than accurate numbers. Lastly, the retrograde transport is known to be incomplete and not label all synapses (Callaway and Luo, 2015), and usually this can be addressed by overexpressing the RVG protein. We are therefore currently also performing a second set of experiments where we are performing the same strategy, but with two AAV viruses – one containing the TVA, and another containing the RVG – at a 1:5 ratio, therefore greatly increasing the availability of the glycoprotein.

Despite all of the above described limitations, rabies-virus mediated retrograde tracing remains an extremely powerful tool to understand the topography and identity of projections between cell types. It overcomes several of the issues associated with performing slice recordings

– it adds more evidence to clear the discrepancies between previous slice recording data, it need not be estimated only in mice at younger ages, it need not be limited to estimating the connectivity of neurons in proximity to each other, and it can gain a better idea of the strength and pattern of projections along different dorsoventral depths of the mEC. Using this method, here, we provide definite evidence that local projections within the mEC superficial layers are organized as columns, similar to other cortical areas. While there have been some reports of columnar projections from the deep to superficial layers (van Haeften et al., 2003; Ohara et al., 2018), this has more extensively been described in this paper specifically for within the superficial layers. Gaining a better understanding of these projections is essential to understand how anatomical connectivity might give rise to functional firing within the mEC. Ultimately, we are optimistic that a combination of slice recordings and virus mediated tracing can provide a better understanding of the organization of circuits within the mEC.

Acknowledgements

This work was supported by a Howard Hughes Medical Institute International Student Research Fellowship to I.Z., an Anandamahidol Foundation Fellowship to V.L., the Whitehall Foundation (20130571, 20140863), a Walter F. Heiligenberg Professorship to J.K.L, and by the National Institutes of Health (NS084324, NS086947, MH100349 and MH108594, NS102915, NS097772).

Chapter 2, in full, is material that is unpublished and coauthored by Zutshi, I, Fu, ML, Lilascharoen, V, Leutgeb, JK, Lim, BK, and Leutgeb, S. The dissertation author was the primary researcher of this material.

III.

Recurrent Circuits within Medial Entorhinal Cortex Superficial Layers Support Grid Cell Firing

"Memory is not what the heart desires. That is only a mirror, be it clear as Kheled-zaram. Or so says the heart of Gimli the Dwarf. Elves may see things otherwise. Indeed, I have heard that for them memory is more like to the waking world than to a dream. Not so for Dwarves."

— J. R. R. Tolkien, Fellowship of the Ring

Abstract

Specialized cells in the medial entorhinal cortex (mEC), such as speed cells, head direction (HD) cells, and grid cells are thought to support spatial navigation. To determine whether these computations are dependent on local circuits, we record neuronal activity in mEC layers II and III and optogenetically perturb locally projecting layer II pyramidal cells. We find that sharply tuned HD cells are only weakly responsive while speed, broadly tuned HD cells, and grid cells show pronounced transient excitatory and inhibitory responses. During the brief period of feedback inhibition, there is a reduction in specifically grid accuracy, which is corrected as firing rates return to baseline. These results suggest that sharp HD cells are embedded in a separate mEC sub-network from broad HD cells, speed cells, and grid cells. Furthermore, grid tuning is dependent on local processing, but also rapidly updated by HD, speed, or other afferent inputs to mEC.

Introduction

The medial entorhinal cortex (mEC) harbors several functional cell types that are thought to be essential for spatial navigation and memory. These cell types include grid cells – cells that fire in striking hexagonally arranged fields (Hafting et al., 2005; Sargolini et al., 2006), head direction (HD) cells – cells that fire only when an animal's head is facing a particular direction (Taube et al., 1990), and speed cells – cells whose firing rates are modulated by the running speed of an animal (Kropff et al., 2015). The co-localization of these functional cell types in the superficial layers (layers II and III) of mEC (Giocomo et al., 2014; Kropff et al., 2015; Reifenstein et al., 2016; Sun et al., 2015), along with the high proportion of grid cells within layer II of the mEC (Sargolini et al., 2006), has led to standard models of grid cell generation which require the integration of HD and speed information within local circuits as well as recurrent connectivity between grid cells (Burak and Fiete, 2009; Burgess et al., 2007; Fuhs and Touretzky, 2006; Giocomo et al., 2011b; Hasselmo, 2008; McNaughton et al., 2006a; Zilli, 2012). While the neural circuit that forwards HD information from the anterior thalamic nucleus via the presubiculum to mEC is well described (Taube, 2007; Winter et al., 2015), the source of the speed signal to grid cells within the mEC remains less certain (Gonzalez-Sulser and Nolan, 2016). Speed information could either be derived from the frequency and amplitude modulation of theta oscillations by running speed(Jeewajee et al., 2008) or from the readout of the firing rate of speed-modulated cells within mEC (Hinman et al., 2016; Kropff et al., 2015). Despite the uncertainty about the source of speed information, HD and speed information have been proposed to be combined into a velocity signal before being forwarded to generate grid cells (Burak and Fiete, 2009; Hasselmo, 2008).

Although the site and mechanism for the processing and integration of speed and HD information remain unresolved, it is assumed that head-direction and speed signals are conveyed by specialized afferent pathways to mEC. Therefore, most investigations on grid generation have thus far focused on brain regions that strongly project directly and indirectly to the mEC.

Accordingly, it has been demonstrated that afferent inputs from the hippocampus (Bonnevie et al., 2013), the medial septum (Brandon et al., 2011; Koenig et al., 2011; Newman et al., 2014) and the anterior thalamic nucleus (Winter et al., 2015) are required for the periodic firing patterns of grid cells. These manipulations were found to have effects on spatial information, speed modulation, theta oscillations, directional tuning, or a combination thereof. Past findings are thus consistent with the general notion that a disruption in either heading or speed information blocks the neuronal computations required for grid firing. However, details on how each of the long-range input streams is combined within local networks remain to be identified. Unexpectedly, experiments that disrupted local circuits within mEC – one which targeted local parvalbumin-expressing interneurons (Buetfering et al., 2014) and the other which targeted stellate cells in layer II (Kanter et al., 2017) – did not observe any effects on grid firing patterns. In addition, a recent study that inhibited mEC PV cells increased firing rates of grid cells predominantly outside of grid fields while grid centers remained aligned (Miao et al., 2017). The limited effects of local circuit manipulations on grid cells therefore raise the possibility that dendritic processing or ion channel composition of a cell predominantly contribute to grid generation, and that grid firing may thus selectively emerge in a particular morphological cell type. Numerous studies have therefore compared the two major morphological cell types in mEC layer II – stellate (LIIS) and pyramidal cells (LIIP). The combined evidence from these studies suggests that grid cells can be found in either population (Domnisoru et al., 2013; Schmidt-Hieber and Häusser, 2013; Sun et al., 2015; Tang et al., 2014). Furthermore, altering cellular properties by knocking out HCN1 channels, which are most abundant in LIIS cells, did not interfere with the generation of grid patterns and only affected grid spacing (Giocomo et al., 2011a). Thus, studies addressing either cellular or circuit computations within the mEC have not clearly determined whether local processing within the mEC superficial layers is required for sustaining grid firing patterns.

To address whether local circuits in the superficial layers support the firing patterns of functional cell types in mEC, we considered the detailed anatomical organization of connections within the superficial layers that were revealed by performing paired recordings in entorhinal slices (see **Figure 3.1a** for a schematic). While LIIP cells were with limited sampling reported to not project to LIIS cells (Couey et al., 2013), recent studies have shown dense direct projections from LIIP to LIIS cells, to other LIIP cells, and to local inhibitory interneurons (Fuchs et al., 2016; Winterer et al., 2017). Particularly remarkable is that synaptic connectivity from LIIP to LIIS exceeds a probability of 10 % and is characterized by exceptionally strong and fast synaptic transmission (Winterer et al., 2017). Reports on the local projections of LIIS cells have also been conflicting (Couey et al., 2013; Dhillon and Jones, 2000; Pastoll et al., 2013), but large scale sampling has confirmed that they neither extensively target LIIP nor LIII pyramidal cells, but rather send dense projections to the deep layers of the mEC (Sürmeli et al., 2015; Winterer et al., 2017). Based on these differences in connection patterns between LIIP and LIIS cells, we reasoned that manipulations of LIIP cells would be particularly effective in perturbing neuronal activity in the superficial layers. We therefore first confirmed that LIIP cells have the majority of their synaptic terminals within mEC superficial layers (Sürmeli et al., 2015) and then optogenetically activated LIIP cells to recruit LIIS cell excitation, and as a consequence of direct and indirect activation of both principal cell types, interneuron driven feedback inhibition that transiently perturbed network activity across layers II and III. We then used this approach to test whether HD and speed tuning is disrupted together with grid firing.

Results

LII pyramidal cells project densely within LII of mEC

To selectively perturb neuronal activity within the mEC superficial layers, we sought to manipulate a cell population that projects predominantly within the superficial layers and has

limited synaptic contacts in other mEC layers and areas outside of mEC. LIIP cells have been shown to project within LII (**Figure 3.1a**), while only sending a minor projection to CA1 (Fuchs et al., 2016; Kitamura et al., 2014, 2015; Sürmeli et al., 2015; Winterer et al., 2017). We therefore

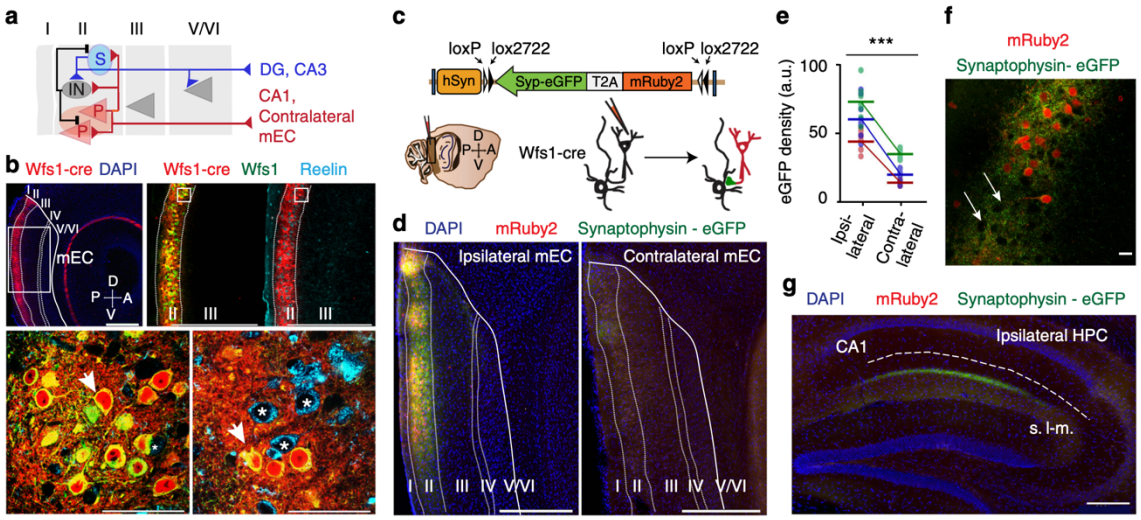

Figure 3.1. LIIP cells project densely within mEC LII.

(a) Schematic describing the local anatomical connections of LII cells (P pyramidal cell, S stellate cell, IN interneuron). (b) Top, Expression of Cre recombinase in a Wfs1-creER mouse is restricted to LII of mEC, as shown by crossing the Wfs1 line to the Ai14 mouse line. Scale bar, 500 µm. Top right, Magnified images (corresponding to the white box to the left) show that Cre expression overlaps with the Wfs1 protein but not Reelin. Bottom, Magnification of Wfs1- and Reelin-stained sections (white boxes in top-right panel) shows Cre expression (red) exclusively in Wfs1+ (green) LIIP cells (yellow when the two labels are merged, arrows) but not in Reelin+ (blue) LIIS cells (asterisks). Scale bar, 20 µm. (c) An AAV construct with a Cre-dependent cassette expressed mRuby2 and Synaptophysin-eGFP, which when activated, resulted in the labeling of cell bodies with mRuby2 and of synaptic terminals with eGFP. (d) Left, Injection in the dorsal mEC of Wfs1-creER mice reveals dense synapses of Wfs1+ cells locally within LII but not extending to other layers of the mEC. Right, The contralateral hemisphere of the same brain has sparse synaptic density. Scale bar, 500 µm. (e) Quantification of eGFP fluorescence intensity reveals that the projections of LIIP cells to the contralateral hemisphere are weaker than those on the ipsilateral side [Wilcoxon matched-pairs signed-rank test, n = 27 ROIs from 3 mice, $W(27) = -378$, $p < 0.001$]. Each color represents a different animal, and individual dots represent different ROIs from each animal. ***$p < 0.001$. (f) LIIP cells (red) synapse densely around all cell bodies within LII. Arrows point to LII Wfs1− cells that are surrounded by LIIP cell synapses. Because LIIP cells occur in patches along LII, these Wfs1− cells are in stellate cell-rich zones between patches. Scale bar, 20 µm. (g) We observed synapses from LIIP cells in CA1 but not in the DG-CA3 region, where LIIS cells are known to terminate, further confirming that the Wfs1 line is selective for LIIP cells. Scale bar, 500 µm.

first examined the density of LIIP cell projections within the superficial layers of entorhinal cortex by using a transgenic mouse line that expresses tamoxifen inducible Cre recombinase protein under the Wolfram syndrome 1 homolog promoter (Wfs1-creER mice). We confirmed the previously reported result that this line exclusively labels LIIP cells, with no overlap with the DG-projecting LIIS cells (Sürmeli et al., 2015) (**Figure 3.1b**). To then compare the relative density of pyramidal cell projections to different targets, we injected a Cre dependent adeno-associated virus (AAV) expressing mRuby2 and synaptophysin linked to eGFP (AAV-hSyn-FLEX-mRuby2-SynapTAG) into the mEC of Wfs1-creER mice (**Figure 3.1c**) to label cell bodies and axons of LIIP cells with the soluble fluorophore mRuby2 (in red) and synaptic terminals with synaptophysin-eGFP (in green). Using this method, we confirmed the previously reported ipsilateral and contralateral projections within the mEC (Fuchs et al., 2016; Kitamura et al., 2014; Sürmeli et al., 2015; Varga et al., 2010; Winterer et al., 2017), but also identified that the ipsilateral projections were far denser (**Figure 3.1d, e**) and had greater spread (mean ± sem, Ipsilateral: 0.2405 ± 0.0223 mm^2, Contralateral: 0.0176 ± 0.0028 mm^2. Wilcoxon matched-pairs signed rank test, n = 9 sections from 3 mice, W(9) = -45, $p = 0.0039$) than the projections to the contralateral mEC. We found that the ipsilateral projections formed a network of synapses within LII where both patches of Wfs1+ cells and neighboring regions with Wfs1- cells appeared to be densely surrounded by synapses of LIIP cells (**Figure 3.1f**). Outside of the mEC, we only observed the previously described projections to CA1 (**Figure 3.1g**) and no projections to any other brain regions. Thus, the dense local connectivity within layer II but not other mEC layers, along with the particularly weak projections to other brain areas, provided an ideal system to specifically manipulate the superficial layers of mEC.

Functional connectivity of LIIP recurrent circuits

To determine whether the dense ipsilateral projections observed with anterograde viral tracing provided functional local control of neuronal activity in the intact brain, we optogenetically

activated LIIP cells while recording single-unit activity from cells across LII and LIII in freely behaving mice. We began by expressing Cre-dependent Channelrhodopsin2 (AAV-EF1α - FLEX-ChR2-EYFP) in the mEC of Wfs1-creER mice. Next, we implanted a movable array consisting of an optic fiber and four tetrodes (optetrode with the tetrodes < 1mm deeper than the tip of the optic fiber) (Anikeeva et al., 2012), which permitted simultaneous single-unit recordings and optogenetic stimulation in the mEC (**Figure 3.2a**). We then performed recordings of LII and LIII cells in an open field arena during baseline sessions without optical manipulations and during stimulation sessions. Throughout the entire stimulation session, LIIP cells were repetitively activated at one of two stimulation frequencies – 8 Hz or 12 Hz. The two distinct frequencies were chosen to control for the possibility that there might be a frequency dependent effect of rhythmic excitation of LIIP cells, especially for frequencies close to theta oscillations (~8 Hz). Moreover, both of these frequencies allowed sufficient time for recovery of cells between light pulses (83.3 ms for 12 Hz, 125 ms for 8 Hz), but also regularly perturbed the network throughout the session. We observed that most cells responded to optogenetic stimulation by increased excitation, synaptic inhibition, or both (**Figure 3.2b, Figure 3S.2**). As expected based on the strong excitatory circuits within LII (Winterer et al., 2017), directly and synaptically activated cells could not be distinguished based on commonly used criteria such as latency or jitter (Anikeeva et al., 2012; Buetfering et al., 2014; Zhang et al., 2013) (**Figure 3S.2**, also see Online Methods). Collectively, excitation was observed in a large fraction of LII cells (~50 %) with the peak latency at ~6-7 ms after light onset.

Because LIIP cells were reported to not project to LIII (Winterer et al., 2017), we analyzed whether LIII cells may be differently affected by the stimulation. Consistent with the limited excitatory connectivity between LII and LIII, only ~12 % of LIII cells were excited (**Figure 3.2c, d, e, Table 3S.1**) while the remainder was predominantly inhibited. Taken together, LIIP cell excitation and the ensuing feedback inhibition altered the firing rates of >85 % of all recorded cells

in LII and LIII. Our strategy thus effectively and selectively perturbed superficial layers in the mEC.

Because the optically activated LII cells are excitatory (Alonso and Klink, 1993; Canto and Witter, 2012; Fuchs et al., 2016; Kitamura et al., 2014; Winterer et al., 2017), we reasoned that the profound inhibition observed across LII and LIII was mediated by synaptically connected interneurons. To test whether a substantial fraction of interneurons responded to the photostimulation, we classified cells as putative interneurons using a combination of average firing rate and waveform shape (**Figure 3.2f**) and found that 23 of 30 interneurons (76.7 %) were excited. Next, we sought to determine whether excitation by LIIP cells was selective to any particular interneuron type. In a previous study, interneurons in the hippocampus have been sub-classified by using the burst index (Royer et al., 2012). However, we could not find any relation between the waveform (**Figure 3.2f**) or burst index (**Figure 3.2g, h**) of interneurons and the type of response they demonstrated, leading us to conclude that various subtypes of interneurons were engaged by our manipulation. Consistent with the hypothesis that LIIP activation led to rapid synaptic excitatory responses across all other LII cells, followed by di-synaptic inhibition from excited interneurons, the latency for excitation was found to precede the latency for inhibition by 3-4 milliseconds (**Figure 3.2i**).

Since our anterograde tracing also revealed sparse synapses from LIIP cells to the contralateral mEC (**Figure 3.1d, e**), we sought to examine the functional relevance of these projections. In a separate subset of mice, we compared the strength of ipsilateral and contralateral stimulation. The response to bilateral stimulation was almost identical to unilateral stimulation (**Figure 3S.3**), which led us to conclude that bilateral manipulations would not perturb the ipsilateral mEC any more effectively than unilateral stimulation. Thus, all further analyses were restricted to datasets with unilateral perturbation.

Figure 3.2. Functional connectivity of LIIP cells.

(a) Schematic describing the recording strategy and behavioral paradigm. (b) Cells were divided into four categories, depending on how they responded to the photostimulation. Example raster plots and peri-stimulus time histograms for each of the categories are shown. Vertical red lines indicate light onset. (c) All recorded mEC LII principal cells divided by response category. Each row is the peri-stimulus firing rate of a single cell, normalized to its peak firing rate (scale, color bar to the right). The cells are sorted by their response latencies. Excited cells have a sharp peak within 10 ms after the light pulse, whereas inhibited cells reduce their firing rate up to ~30 ms after the light onset. Red traces, mean normalized firing rate across all cells within the category (scaled to the red bar on the right). Blue arrow, light onset. (d) Plots as described in c but for cells recorded in LIII. Primarily inhibition was observed in LIII cells, thus the excitatory responses of <15% of cells are not shown. (e) Quantification of responses shows that ~85% of LII and LIII cells were perturbed by the stimulation. (f) Average firing rates on a logarithmic scale versus the peak-valley ratio of the spike waveform of all cells distinguished putative principal cells (red dots) from interneurons. Cells outside of or between the two clusters were excluded from further analyses (sections in green). Thirty putative interneurons were recorded, 26 from LII (circles) and 4 from LIII (diamonds). Color code as in e. (g) Color-coded (maximum, red; minimum, blue) autocorrelograms of all interneurons ordered by their burst index and with the response category of each cell denoted by colored dots on the right (color scheme as in e). (h) The burst index (mean ± sem) of putative interneurons is plotted by response category (color scheme as in e). Response category did not predict burstiness [Kruskal–Wallis test, $H(3) = 3.124$, $p = 0.2097$]. (i) Distribution of the latencies for excited (blue line) and inhibited (gray line) principal cells. Excitation occurred rapidly and was followed by feedback inhibition.

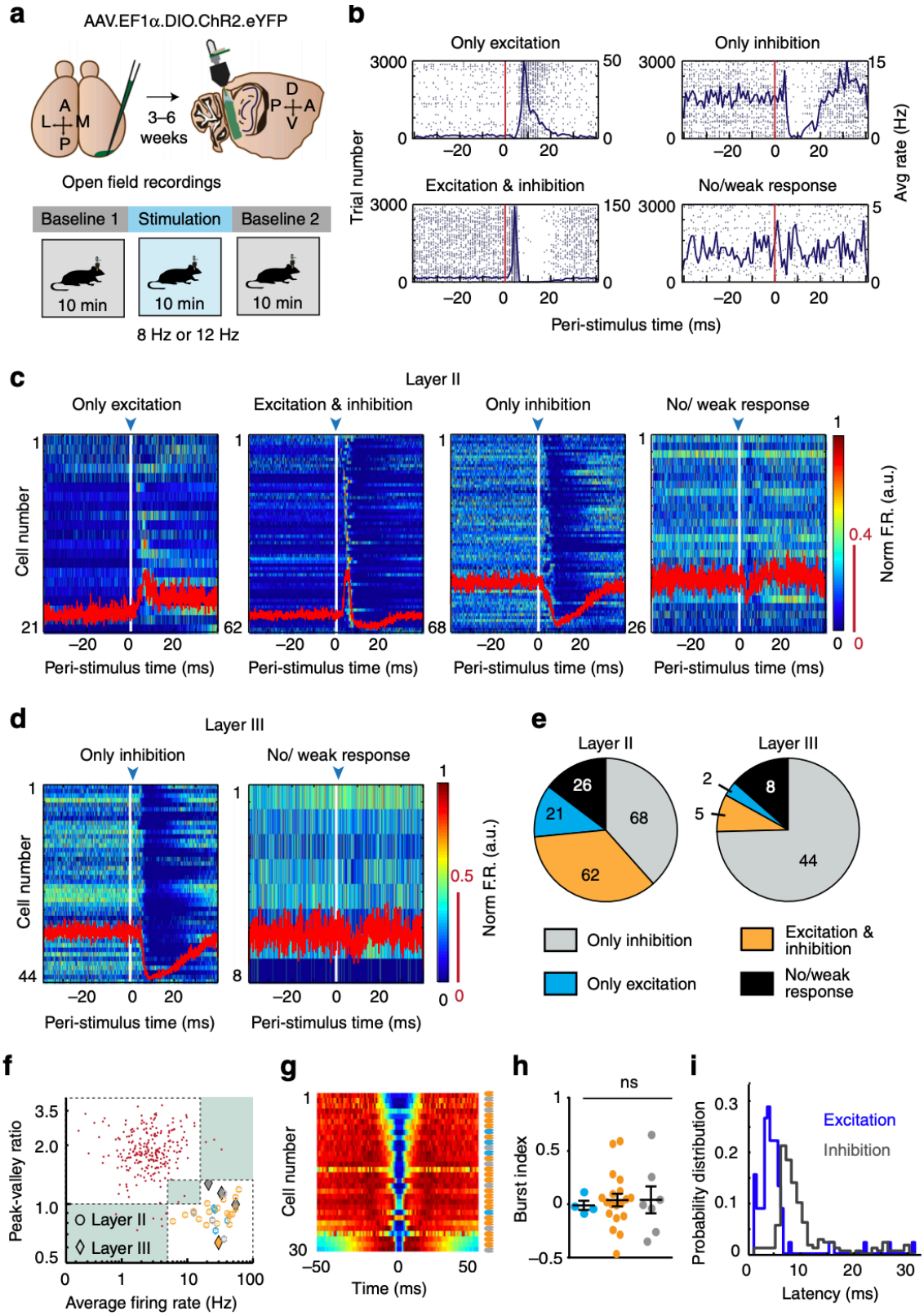
a
AAV.EF1α.DIO.ChR2.eYFP
A
L
M
P
3–6 weeks
D
P
A
V
Open field recordings
Baseline 1
Stimulation
Baseline 2
10 min
10 min
10 min
8 Hz or 12 Hz
b
Only excitation
Only inhibition
Excitation & inhibition
No/weak response
Trial number
Avg rate (Hz)
Peri-stimulus time (ms)
c
Layer II
Only excitation
Excitation & inhibition
Only inhibition
No/ weak response
Cell number
Norm F.R. (a.u.)
Peri-stimulus time (ms)
d
Layer III
Only inhibition
No/ weak response
Cell number
Norm F.R. (a.u.)
Peri-stimulus time (ms)
e
Layer II
Layer III
Only inhibition
Excitation & inhibition
Only excitation
No/weak response
f
Peak-valley ratio
Layer II
Layer III
Average firing rate (Hz)
g
Cell number
Time (ms)
h
ns
Burst index
i
Excitation
Inhibition
Probability distribution
Latency (ms)

LIIP cell activation transiently inhibited speed cells

Activation of LIIP cells resulted in large-scale perturbation of cellular activity within LII and LIII. This response pattern provided us with an opportunity to address whether strong local circuit perturbation in the superficial layers interfered with the firing properties of functional cell types in the same region. We began our analysis with speed cells and compared 10-15 minute sessions with repetitive light stimulation (delivered at 8 Hz or 12 Hz for the entire session duration) to 10-15 minute baseline sessions (without light stimulation) that occurred before and after the light stimulation sessions. Cells were classified as speed cells if their speed score exceeded the 95th percentile of scores from shuffled timestamps (Diehl et al., 2017; Kropff et al., 2015). Using this method, 47 of 266 recorded mEC cells across LII and LIII were identified as speed tuned, with an average firing rate of 12.8 ± 2.36 Hz (mean ± sem, 32 principal cells and 15 interneurons, **Figure 3S. 4a-g**). When analyzing these cells over an entire recording session with repetitive optical stimulation (at 8 Hz or 12 Hz) of LIIP cells, speed tuning was not altered, regardless of the stimulation protocol and whether a cell was excited or inhibited by the perturbation (**Figure 3.3a-c**).

Because our optical manipulation only had measurable effects on firing rates for ~25 ms, we next considered the possibility that speed tuning could only be transiently perturbed. For this analysis, we reasoned that spiking elicited by direct activation of ChR2 trivially alters the firing patterns of cells in the local circuit. However, during the phase when cells rebounded from the subsequent feedback inhibition, we could examine the recovery of information coding by processing of afferent and local inputs to the network. We therefore sorted all speed cells based on their responses to light and asked whether inhibited cells lose their speed tuning during the period of maximum inhibition (I, from the minimum firing rate until each cell regained 50 % of its average baseline firing rate). As a baseline, we downsampled spikes occurring immediately before light onset (Pre) to match the total number of spikes in I. The instantaneous running speeds during each

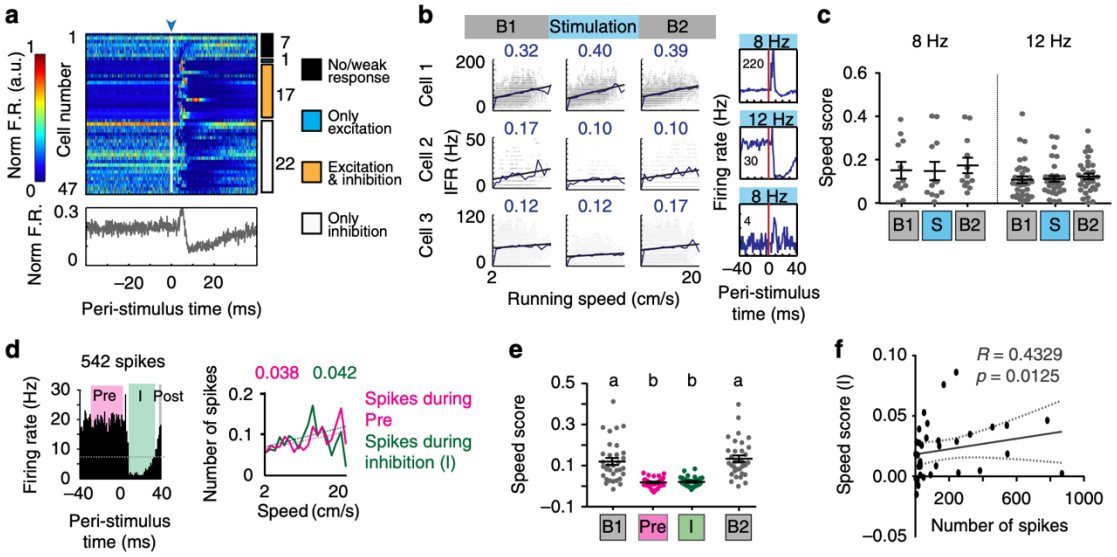

Figure 3.3. Speed cells were transiently inhibited by LIIP stimulation.

(a) Peri-stimulus time plot of all speed cells (32 principal cells, 15 interneurons). Each row is a cell with the firing rate scaled as in the color bar to the left. Cells are ordered by optogenetic response category with the number of cells in each category indicated to the right. The mean normalized firing rate over all speed cells is depicted below the plot, demonstrating a period of inhibition. (b) Example speed cells retained their speed scores (number on top of each plot) during the stimulation session regardless of response category. Optogenetic stimulation frequency is provided on top and peak firing rate is printed within the PSTH plots to the right. (c) Speed scores for stimulation sessions did not differ from baseline sessions. Each dot represents a cell [n = 12 cells for 8 Hz sessions, 33 cells for 12 Hz sessions from 7 mice; two-way ANOVA with repeated measures on one factor, $F(2,86) = 0.2367$, $p = 0.7898$]. (d) Left, PSTH of a speed cell that was transiently inhibited by the optogenetic stimulation. Right, Correlation between instantaneous running speed and either the number of spikes during the period of maximum inhibition (I, green), or an equal number of spikes randomly sampled before light onset (Pre, magenta). Speed scores are shown above the plot. (e) Quantification of speed scores revealed no difference between Pre and I, but both scores were reduced compared to baseline [one-way repeated-measures ANOVA, n = 33 cells from 7 mice, $F(1.858,59.45) = 44.94$, $p < 0.0001$]. Significantly different groups (Tukey's multiple comparisons test, $p < 0.05$) are assigned different letters (a, b). (f) There was a significant correlation between the speed score during inhibition (I) and the number of spikes during inhibition (I), suggesting that the decrease in speed score can be explained by the increased variability from low spike numbers [Spearman's rank correlation, n = 34 cells from 7 mice, $R = 0.4239$, $p = 0.0125$]. Plots in c, e show the mean ± sem.

of these windows were then used to perform a correlation with firing rates in the corresponding window (**Figure 3.3d**). Speed scores did not differ between I and Pre, but were in both cases reduced compared to baseline, suggesting that subsampling to low firing rates is sufficient to lower

the score (**Figure 3.3e**). Indeed, the speed scores during I were correlated to the number of spikes in the window (**Figure 3.3f**). Therefore, the decrease in speed tuning of mEC speed cells did not exceed the level that could be explained by reduced spiking during the inhibition window.

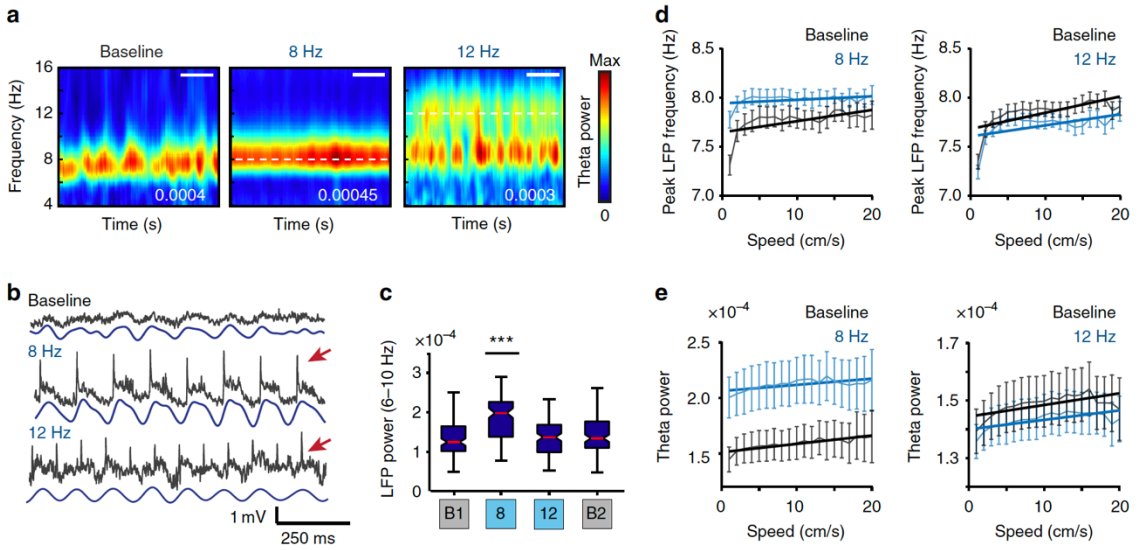

Figure 3.4. Speed modulation of theta oscillations was preserved during LIIP activation.

(a) Spectrograms of wavelet power for an example baseline, 8 Hz, and 12 Hz stimulation session. The peak power is on the bottom right, and the white dashed line highlights the stimulation frequency. Scale bar, 50 s. (b) Example raw (gray) and filtered (blue) LFP traces during baseline, 8 Hz, and 12 Hz stimulation sessions, where population spikes (example shown by a red arrow) distorted the raw LFP signal during stimulation. For 12 Hz stimulation sessions, filtering the LFP between 6 and 10 Hz eliminated distortion of the signal by population spikes. (c) Average wavelet power confirms that endogenous theta power was not altered during 12 Hz stimulation. Light-induced population spikes distorted the signal during 8 Hz stimulation sessions, leading to artificially high LFP power in the theta frequency range [boxes, median ± 25th percentile, whiskers, min. to max.; one-way ANOVA, n (session) = 121 (B1), 37 (8 Hz), 58 (12 Hz), and 120 (B2) across 7 mice, $F(3,335) = 7.001$, $p = 0.0001$]. Tukey's multiple comparisons test, ***$p < 0.001$. (d) Linear regression of running speed versus peak theta frequency between 6 and 10 Hz for baseline (left, gray) or 8 Hz sessions (left, blue) and baseline (right, gray) or 12 Hz sessions (right, blue). The two slopes were not different from each other in either stimulation condition [ANCOVA, 8 Hz: n = 37 sessions across 7 mice, $F(1,36) = 3.407$, $p = 0.0731$, 12 Hz: n = 58 sessions across 7 mice, $F(1,36) = 0.7171$, $p = 0.4027$]. (e) Linear regression of running speed versus mean theta power between 6 and 10 Hz for all baseline (left, gray) or 8 Hz sessions (left, blue) and baseline (right, gray) or 12 Hz sessions (right, blue). The two slopes were not different from each other in either stimulation condition [ANCOVA, 8 Hz: n = 37 sessions across 7 mice, $F(1,36) = 1.461$, $p = 0.2347$, 12 Hz: n = 58 sessions across 7 mice, $F(1,36) = 0.5918$, $p = 0.2928$]. Plots in d, e show the mean ± sem.

Theta oscillations were unaltered by LIIP cell activation

We next asked whether other potential sources of speed information within the mEC could be perturbed during our manipulation. Theta oscillations arising from the medial septal area are modulated by running speed (Jeewajee et al., 2008), and can therefore be a source for speed information. For our analysis of theta oscillations, we had to consider that our optogenetic stimulation generated population spikes in the LFP signal, which were superimposed onto endogenous LFP and did not allow us to measure theta power (6-10 Hz) independently of stimulation effects for 8 Hz stimulation (**Figure 3.4a, b**). For 12 Hz stimulation sessions, however, we could clearly distinguish two separate frequency bands – one at 12 Hz, arising due to the population spikes and another at theta frequencies – and were able to show that there was no detectable increase in the endogenous theta amplitude from population spikes (**Figure 3.4c**). We next performed a linear regression between running speed and either the peak theta frequency (**Figure 3.4d**) or average theta power (**Figure 3.4e**) and found no difference between the slopes of baseline and stimulation sessions for both measurements for 12 Hz sessions. For 8 Hz sessions, population spike artifacts remained in the filtered signal (6-10 Hz) and increased the average theta power, while the power nonetheless remained modulated by running speed to the same extent as during baseline. Theta-related speed information was thus retained in the mEC throughout sessions with local mEC circuit perturbation. In addition, we observed that mEC cells which were strongly modulated by theta oscillations maintained their theta phase preference during inhibition (**Figure 3S.5**).

HD cell tuning was intact during LIIP cell activation

We next investigated whether LIIP cell photostimulation resulted in a disruption of HD tuning. Because the HD cell population in our dataset showed a clear bimodal distribution of tuning width (**Figure 3S.4a, c**), we classified sharply tuned cells (HD score > 0.5, n = 23 cells across LII

and LIII) as narrow HD cells and the less strikingly HD modulated population as broad HD cells (HD score > the 95th percentile of shuffled distributions and < 0.5, n = 58 cells across LII and LIII).

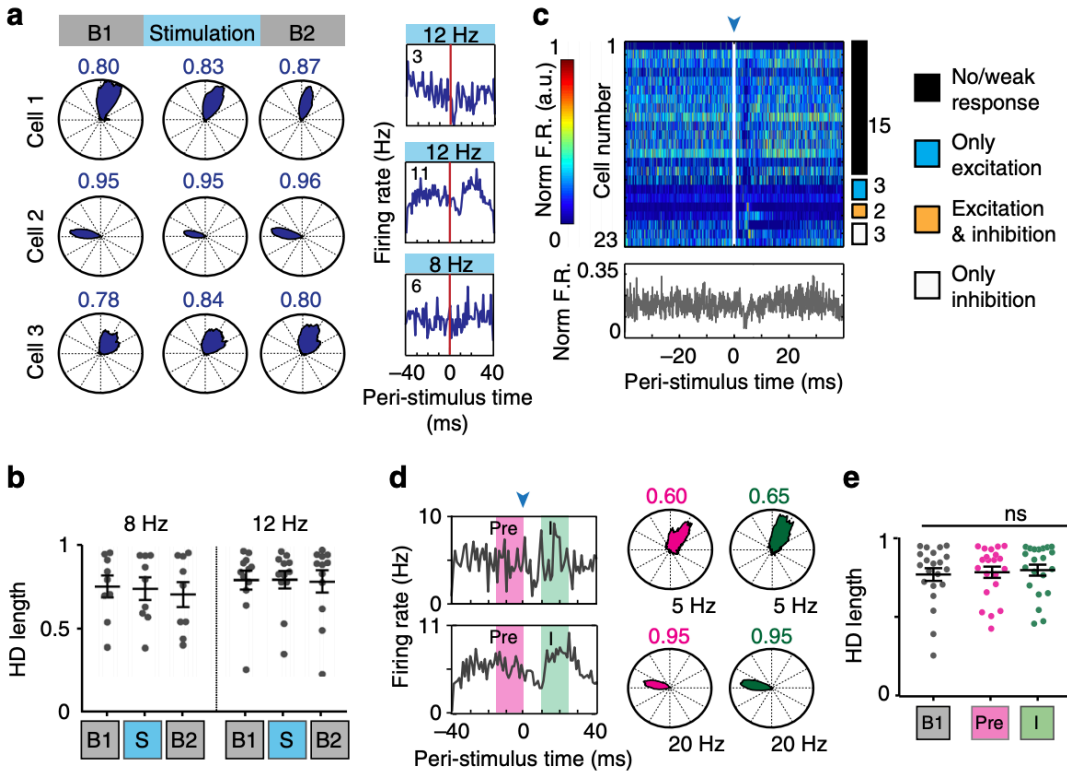

Figure 3.5. Narrow HD cells only weakly responded to optical LIIP activation.

(a) Example narrow HD cells maintained their directional tuning and at most weakly responded to LIIP stimulation (shown in the rightmost plot). The HD score (i.e., mean resultant length of HD tuning) is indicated above each polar plot. (b) There was no reduction in HD score for 8 and 12 Hz stimulation sessions [two-way ANOVA with repeated measures on one factor, n.s. interaction, n = 9 cells for 8 Hz, 12 cells for 12 Hz across 6 mice, $F(2,38) = 0.3363$, $p = 0.7165$]. (c) Peri-stimulus time plot for all HD cells. Cells are ordered by their optogenetic response category with the number of cells in each category indicated to the right. Most narrow HD cells showed weak or no response to the optic stimulation, as can also be seen from the mean normalized firing rate of all narrow HD cells. (d) HD tuning of two example cells when only spikes between 10 and 25 ms after light onset (I, green) and the same number of spikes between 15 and 0 ms before light onset (Pre, magenta) were included. (e) Quantification of HD tuning of all narrow HD cells revealed no difference between the two baseline sessions, and I and Pre windows [one-way repeatedmeasures ANOVA, n = 21 cells from 6 mice, $F(2.199,43.97) = 2.493$, $p = 0.0894$]. Plots in b, e show the mean ± sem.

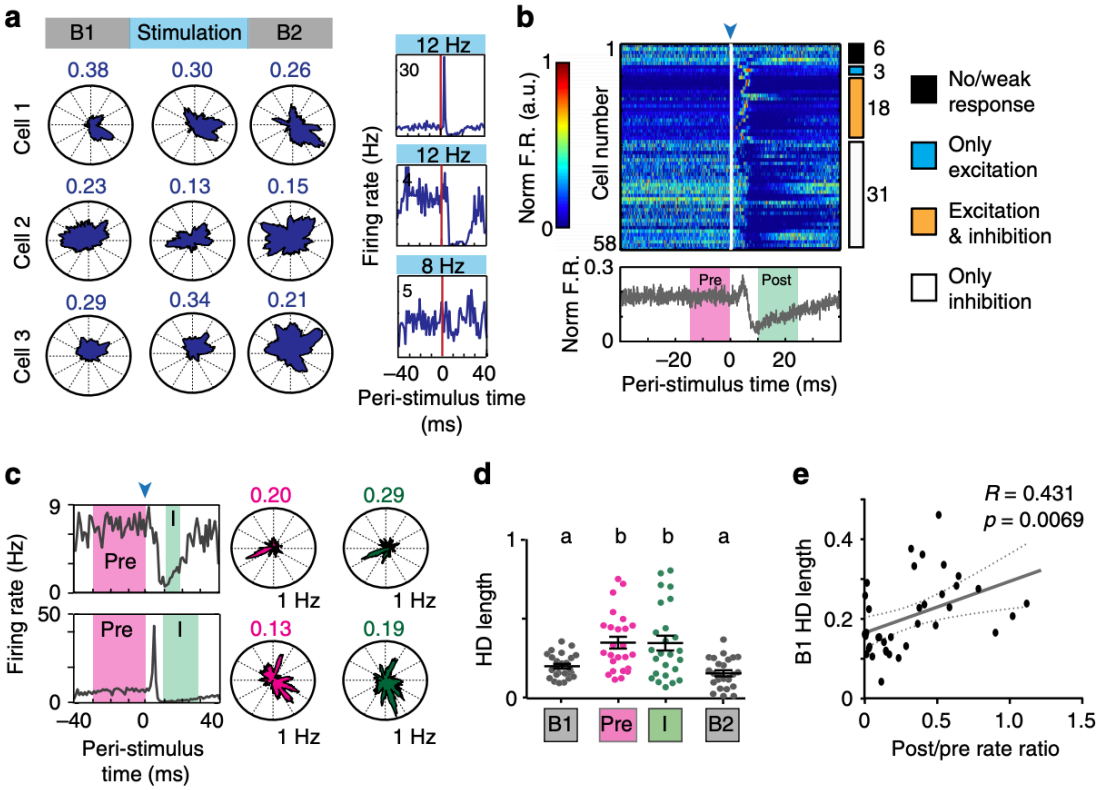

Figure 3.6. Inhibition of broad HD cells did not reduce HD tuning.

(a) Example broad HD cells retained their directional tuning regardless of their response to optical LIIP activation (shown in the rightmost plot). The HD score is indicated above each polar plot. (b) Peri-stimulus time plot for all broad HD cells. Cells are ordered by optogenetic response category with the number of cells in each category indicated to the right. Broadly tuned HD cells displayed heterogeneous responses to stimulation, but a large fraction was inhibited, as also seen in the mean normalized firing rate over all broad HD cells. (c) Examples of broad HD cells that were inhibited by LIIP activation. HD scores were calculated only for spikes during the inhibition period (I, green) and for an equal number of spikes from the period before light onset (Pre, magenta). (d) Quantification of HD tuning of all inhibited broad HD cells revealed no differences between Pre and I periods, but both windows had significantly greater HD tuning than baseline [one-way repeated-measures ANOVA, n = 25 cells from 7 mice, $F(1.8,43.21) = 15.46$, $p < 0.0001$], indicating that HD scores moderately increase when using fewer spikes in the analysis. Significantly different groups (Tukey's multiple comparisons test, $p < 0.05$) are assigned different letters (a, b). The mean ± sem are shown. (e) The baseline HD score of inhibited broad HD cells was correlated with the reduction in firing rate by optical LIIP cell stimulation, measured as the ratio between firing rate after light onset [10 to 25 ms, Post, green in b] and before light onset [−15 to 0 ms Pre, magenta in b]. The results imply that increased baseline HD tuning was related to lower feedback inhibition [Pearson's correlation, n = 38 cells from 7 mice, $R = 0.431$, $p = 0.0069$].

We first examined the effect of stimulation on narrow HD cells. There was no change in HD selectivity for the entire stimulation session compared to baseline sessions, regardless of stimulation frequency and response type (**Figure 3.5a, b**). We next determined whether there was any disruption in the firing properties of these cells on a shorter time-scale. Surprisingly, we found that most narrow HD cells (15 of 23, 65.2 %) only showed weak or no responses to light stimulation (**Figure 3.5c**), while other cells recorded in proximity or simultaneously with narrow HD cells were highly responsive to light stimulation (**Figure 3S.6, Table 3S.2**). Because narrow HD cells were largely non-responsive, we could not use an inhibition window as described for speed cells and instead compared spikes during the time window when other cells in the circuit were maximally inhibited (between 10 to 25 ms after light onset) to an equal number of spikes between 15 and 0 ms before light onset (**Figure 3.5d**). The HD score was not significantly changed even during the smaller time window (**Figure 3.5e**).

Next, we examined the effect of LIIP cell activation on broad HD cells. As for narrow HD cells, HD tuning was stable when averaging across the entire stimulation session (Two-way ANOVA with repeated measures on one factor, n.s. interaction, n = 19 cells for 8 Hz, 33 cells for 12 Hz across 7 mice, $F(2, 100) = 2.192$, $p = 0.1170$, **Figure 3.6a**). However, broad HD cells showed strong responses in firing rate to the photostimulation with approximately 85 % of cells inhibited (**Figure 3.6b**). As for speed cells, we therefore next examined whether HD tuning was affected during the period of maximal inhibition (I) and, for comparison, randomly selected an equal number of spikes from the 30 to 0 ms period before each light pulse (Pre) (**Figure 3.6c**). We observed that broad HD cells were not disrupted in their HD tuning during I compared to Pre (**Figure 3.6d**). Additionally, we found that the baseline HD tuning was higher for cells that received less inhibition (**Figure 3.6e**). These results were also reproduced with a more conservative, 99th percentile threshold to classify broad HD cells (**Figure 3.4h-j**). Together with the finding that sharply tuned HD cells are largely excluded from inhibition, we thus find an inverse relation between the extent

of baseline HD tuning and local feedback inhibition, and that HD tuning curves were preserved irrespective of the level of inhibition.

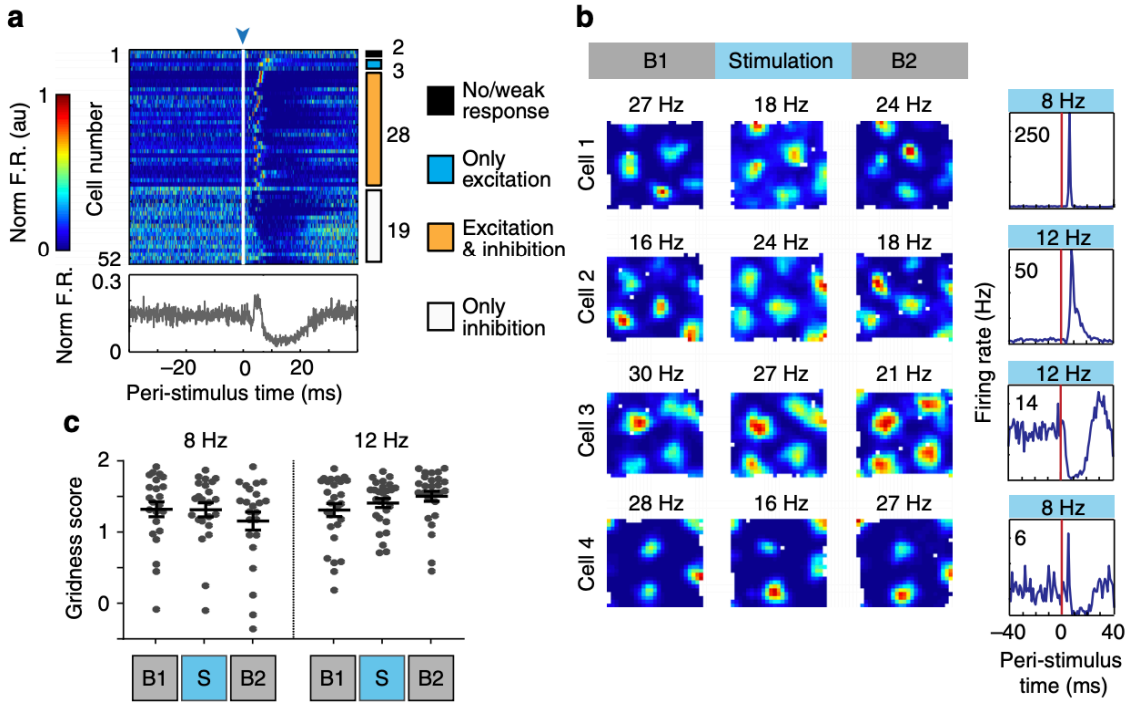

Figure 3.7. Grid cells were inhibited by LIIP cell activation.

(a) Peri-stimulus time plots for all recorded grid cells. Cells are ordered by the response category to optical LIIP activation with the number of cells in each category indicated to the right. Most recorded grid cells (50 of 52) responded to the optical stimulation, and the response typically included a sustained period of inhibition (47 of the 52 grid cells). The mean normalized firing rate over all grid cells is depicted below the plot, demonstrating a sustained window of inhibition. (b) Over the entire stimulation session, example grid cells show preservation of grid fields regardless of their response to the local circuit perturbation (indicated in the leftmost plot). Rate maps are color coded from blue (minimum firing rate) to red (maximum firing rate, provided above each plot). (c) Grid scores remained high during stimulation sessions [two-way ANOVA with repeated measures on one factor, n = 23 cells for 8 Hz, 29 cells for 12 Hz across 3 mice, $F(2,96) = 2.416$, $p = 0.0946$]. Plots show the mean ± sem.

LIIP cell activation led to transient errors in grid firing

Because grid cells are thought to depend on circuits within the mEC that convey direction and speed information, but also on recurrent connections between grid cells(Burak and Fiete, 2009;

Burgess et al., 2007; Fuhs and Touretzky, 2006; Hasselmo, 2008; McNaughton et al., 2006a), it is feasible that grid cells show a more major disruption compared to other cell classes. We identified 52 grid cells [grid scores > 95th percentile of shuffled distribution(Diehl et al., 2017)], all of which were recorded from tetrodes located in LII. We began by examining the responses of grid cells to light pulses (**Figure 3.7a**) and found that most grid cells responded either with excitation and inhibition or with only inhibition, in similar proportions as the entire LII cell population. We first analyzed grid patterns throughout entire recording sessions with light stimulation, and found no obvious disruption in grid firing, regardless of the stimulation frequency and the response type of each cell (**Figure 3.7b, c**).

As a precise measurement of the accuracy of grid patterns during the brief periods of optogenetically induced excitation and inhibition, we calculated the fraction of spikes occurring outside of grid fields compared to the total number of spikes. As expected, only a small fraction (~20 %) of grid cell spikes were outside of grid fields during baseline sessions. Next, we divided grid cells into two non-exclusive groups – cells that were excited (n = 29) and cells that were inhibited (n = 39). For the excited cells, we expected the trivial result that spikes that were elicited as a result of direct optogenetic stimulation would be randomly dispersed because the light stimulation pattern was randomly distributed across open field locations. Accordingly, we found that the out-of-field firing directly due to excitation (spikes between 0-10 ms after light onset) was substantially increased (**Figure 3.8a, b**) and that there was only a small remaining degree of preference for spiking within grid fields (**Figure 3S.7a**).

To examine information coding by local processing, we next examined spikes that occurred during the period of maximal feedback inhibition in the superficial layers. When examining the spatial distribution of these spikes, we found that spike locations during this period were less accurate than those of an equal number of randomly selected spikes from the control period (30 to 0 ms before light onset) (**Figure 3.8c, d**). The accuracy of grid cell spikes rapidly returned to

baseline levels as the grid cells emerged from the period of inhibition (**Figure 3.8e, Figure 3S.7b, c**). To further exclude the possibility that the increase in out-of-field firing emerged as a consequence of directly activating cells, we separately examined grid cells that were only inhibited (n = 16) and found that the reduction in accuracy was equally pronounced in these cells (**Figure 3.8f**). We also examined conjunctive grid by HD cells (n = 10) and determined that grid accuracy but not HD tuning was impaired during inhibition of these cells (**Figure 3S.7f-j**).

To ensure that our finding of transiently increased out-of-field firing was independent of field boundary definitions, we used a second metric for grid accuracy. We calculated the average distance from the closest grid node center for spikes during the window of maximal inhibition (before regaining 50 % of baseline firing rate) and for an equal number of spikes selected from the period before each light pulse (30 to 0 ms). For comparison, we also calculated the mean distance of an equal number of random locations along the path of the animal. These measures were normalized for grid field sizing as described in the Online Methods. We found that there was an increase in the average distance from the center of the node for spikes during inhibition (**Figure 3.9a, b, Figure 3S.7e**). Finally, we tested whether decreased grid accuracy was related to the amount of inhibition a cell received. The spatial displacement of spikes during I showed a weak, but significant correlation with the rate reduction during I (**Figure 3.9c**). Because more inhibited cells contribute fewer spikes to the analysis, we confirmed that the correlation did not simply arise from decreased grid accuracy when fewer spikes are available for the analysis (**Figure 3S.7d**). Taken together, we therefore found that grid accuracy was broadly reduced during the period of feedback inhibition.

Discussion

To test theories that grid cells arise from the processing of direction and speed information by local recurrent circuits in the mEC, we selectively perturbed neuronal activity within the

Figure 3.8. Transient inhibition of mEC superficial layers decreased grid accuracy.

(a) Example grid cell excited by the stimulation. The 376 spikes firing within 10 ms after light onset (E, blue in PSTH) were dispersed in space, while an equal number of randomly selected spikes from before light onset were predominantly located within grid fields (Pre, magenta in PSTH). (b) Increased out-of-field firing of all excited grid cells confirmed the reduced accuracy of ChR2 evoked spikes [one-way repeated-measures ANOVA, n = 29 cells from 3 mice, $F(2.344,65.62) = 51.84$, $p < 0.0001$]. Significantly different groups (Tukey's multiple comparisons test, $p < 0.05$) are assigned different letters (a, b). (c) Example grid cell inhibited by the stimulation. The 69 spikes during inhibition (I, green in PSTH) were less accurate than an equal number of randomly selected spikes from before light onset (Pre, magenta in PSTH). (d) Increased out-of-field firing during maximal feedback inhibition [one-way repeated-measures ANOVA, n = 36 cells from 3 mice, $F(1.721,60.23) = 10.03$, $p = 0.0003$] indicates reduced grid accuracy. Significantly different groups (Tukey's multiple comparisons test, $p < 0.05$) are assigned different letters (a, b). (e) The percentage of spikes outside of grid field boundaries during different inhibition windows (up to 25, 50, 75, and 100% of recovery to baseline rate; I, green) compared to an equal number of spikes from Pre (magenta). Grid firing was restored after cells recovered from inhibition [Post, gray in f]. Wilcoxon matched-pairs signed-rank tests, 25%: $W(32) = -260$, $p = 0.0096$, 50%: $W(39) = -497$, $p = 0.0003$, 75%: $W(42) = -479$, $p = 0.0014$, 100%: $W(44) = -456$, $p = 0.0052$, Post: $W(44) = -150$, $p = 0.3883$. (f) Grid cells that were only inhibited and not excited also demonstrated reduced accuracy during inhibition, suggesting that reduced accuracy was not a direct consequence of ChR2 activation [paired samples t test, n = 16 cells from 3 mice, $t(15) = 3.216$, $p = 0.0058$]. All summary plots show the mean ± sem. $^{**}p < 0.01$, $^{***}p < 0.001$.

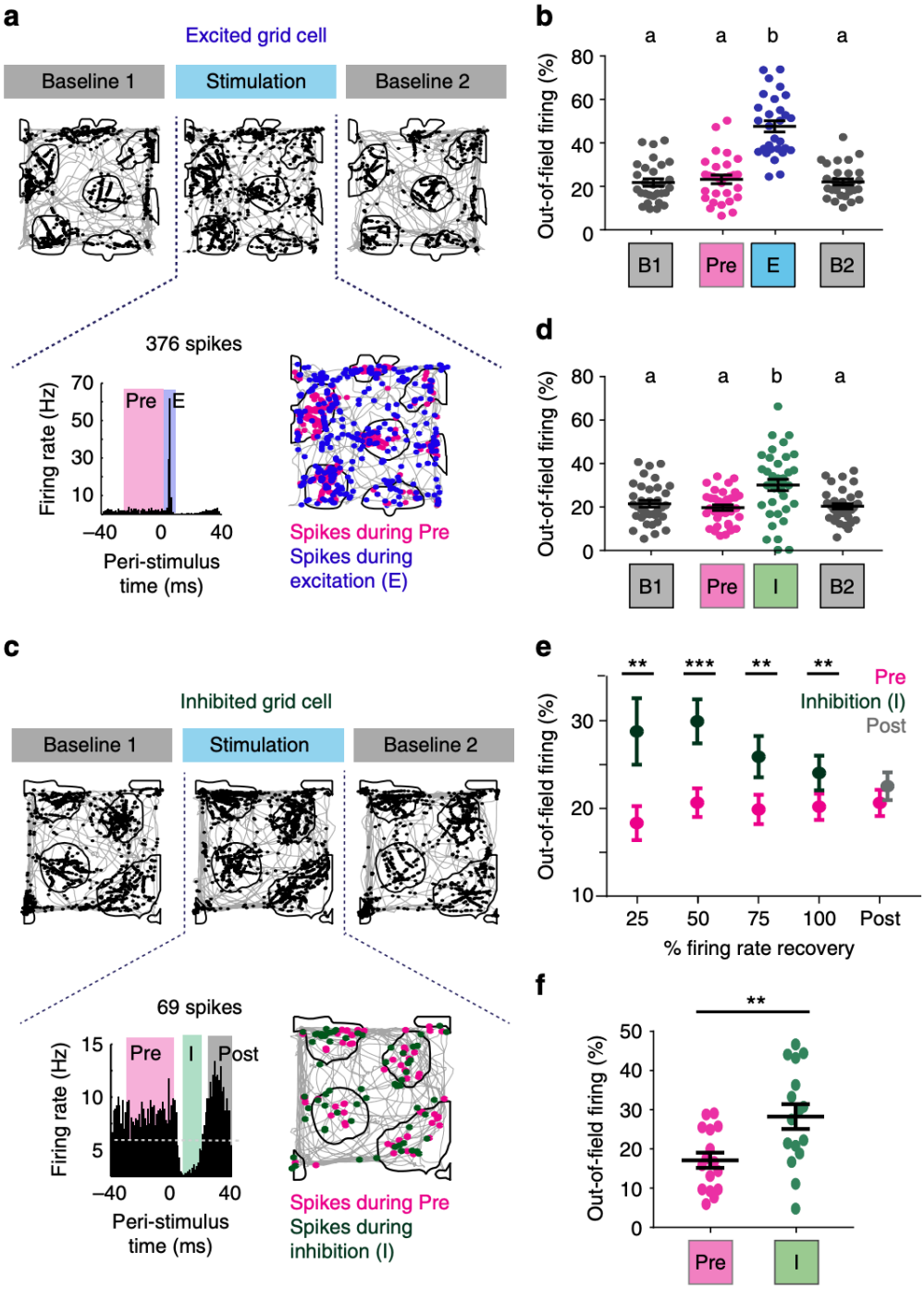
a
Excited grid cell
Baseline 1
Stimulation
Baseline 2
376 spikes
Firing rate (Hz)
70
50
30
10
Pre
E
–40
0
40
Peri-stimulus time (ms)
Spikes during Pre
Spikes during excitation (E)
b
a
a
b
a
Out-of-field firing (%)
80
60
40
20
0
B1
Pre
E
B2
d
a
a
b
a
Out-of-field firing (%)
80
60
40
20
0
B1
Pre
I
B2
c
Inhibited grid cell
Baseline 1
Stimulation
Baseline 2
69 spikes
Firing rate (Hz)
15
10
5
Pre
I
Post
–40
0
40
Peri-stimulus time (ms)
Spikes during Pre
Spikes during inhibition (I)
e
**
***
**
**
Pre
Inhibition (I)
Post
Out-of-field firing (%)
30
20
10
25
50
75
100
Post
% firing rate recovery
f
**
Out-of-field firing (%)
50
40
30
20
10
0
Pre
I

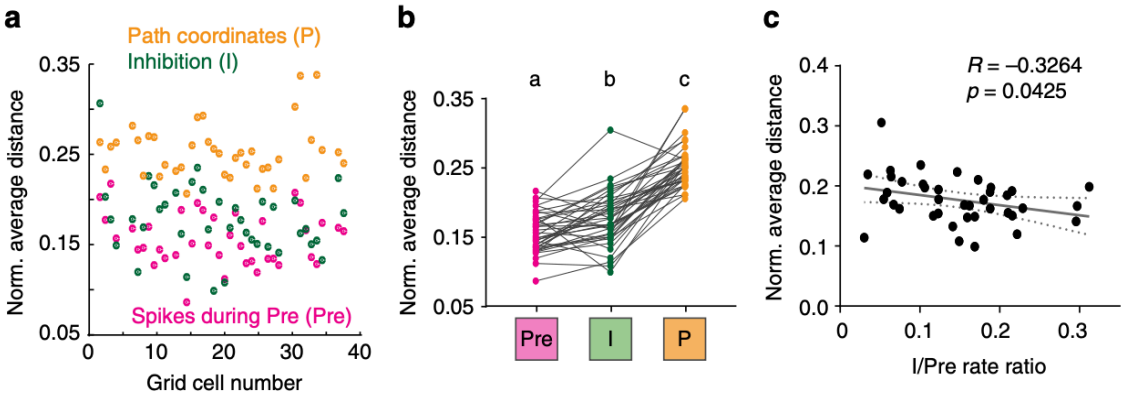

Figure 3.9. Grid cell spikes during inhibition occurred farther from the grid center.

(a) The average distance of each I spike (green dots) from the center of the closest grid node was normalized to the grid spacing for each cell. This distance was compared to the normalized distance of an equal number of Pre spikes (magenta) and an equal number of random locations from the path of the animal (yellow). (b) Spikes during the period of maximal inhibition were farther away from the center of grid fields compared to control spikes but were closer than random locations along the path [one-way repeated-measures ANOVA, n = 39 cells from 3 mice, $F(1.707,64.86) = 137$, $p < 0.0001$]. Significantly different groups (Tukey's multiple comparisons test, $p < 0.05$) are assigned different letters (a, b, c). (c) The normalized distance of I spikes was negatively correlated to the change in the average firing rate between I and Pre, suggesting that errors were larger for cells that were more inhibited [Spearman's rank correlation, n = 39 cells from 3 mice, $R = -0.3264$, $p = 0.0425$]

superficial layers while recording from speed, HD, and grid cells. Consistent with recent results that identified direct excitatory connections between LIIP cells and other LII cells in entorhinal slices (Fuchs et al., 2016; Winterer et al., 2017), we observed synaptic terminals of LIIP cells predominantly within the ipsilateral layer II. As expected from the dense local connectivity of LII cells, optical stimulation in freely moving mice resulted in synchronous excitation that was followed by a period of strong feedback inhibition within layer II, similar to circuit responses observed in several other cortical regions (Liu et al., 2010; Yu et al., 2016). In addition, we also observed that the majority of layer III cells were transiently silenced by feedback inhibition. Although ~85 % of mEC superficial cells were responsive to the perturbation, most sharply tuned HD cells showed no or weak responses to LIIP cell stimulation. In contrast, we found that all other cell classes, including broad HD cells, speed cells, and grid cells were strongly excited and received

feedback inhibition. During the period of inhibition, measurements of HD and speed tuning were only affected to the extent that could be predicted by the reduced spike numbers. In contrast, grid accuracy was reduced beyond the level that was expected from the lower spike numbers during the window of inhibition. However, the location errors in grid cells were brief and not cumulative,

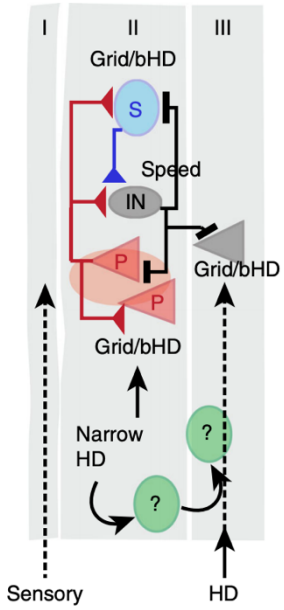

Figure 3.10. Responses of different functional mEC cell types to LII perturbation.

Previous studies using slice electrophysiology have demonstrated that LIIP cells project locally within LII mEC to other LIIP cells, LIIS cells, and local interneurons (also see **Figure 3.1**). In this study, we determined whether these extensive local projections target all functional cell types. Most cell types, including speed cells, grid cells, and broadly tuned HD cells (bHD), were found to show robust excitatory and inhibitory responses to LIIP cell activation. To the contrary, narrowly tuned HD cells only displayed weak responses to the stimulation, indicating that these cells either do not receive local inputs or are coupled to a separate local network within the mEC. Consistent with the strong afferent HD signals to the grid network and the unperturbed local HD signal in narrowly tuned HD cells, HD coding was unaffected by the perturbation, including in broadly tuned and conjunctively tuned HD cells. Similarly, speed coding was only reduced to the extent that was predicted from the firing rate reduction, including in interneurons which showed the highest degree of speed tuning. Despite the minor effects on HD and speed tuning, grid accuracy was reduced during the period of layer LII/III inhibition. Our results thus provide experimental support for the central tenet of most models of grid cell generation, which is that the key computations are performed in local mEC networks that include recurrent connections between grid cells.

which suggests that the processing of HD, speed, and other afferent information was able to rapidly compensate for the perturbed grid tuning in the local circuit (**Figure 3.10**). Together, our results therefore provide experimental support for theories of grid cell generation that have proposed a major contribution of local processing within the superficial layers of mEC.

It is well established that HD tuning is forwarded via the anterior thalamic nucleus and postsubiculum to mEC (van Groen and Wyss, 1990; Taube, 2007; Winter et al., 2015), and we find that afferent HD information is retained in an entorhinal sub-network of sharply tuned HD cells with limited functional connectivity to the majority of principal cells and interneurons. The functional separation of narrow HD cells is even more remarkable when considering that ~85 % of all LII and LIII cells, including broad HD cells, responded to the LIIP cell stimulation. While our results do not identify whether narrow HD cells belong to a particular anatomical cell class, we can conclude that there is not a direct correspondence between narrow HD cells and LIIS cells. First, strong excitatory synapses have been identified between LIIP and LIIS cells (Winterer et al., 2017), which predicts that LIIS cells respond to LIIP cell stimulation. Second, only ~10 % of all LII cells are narrow HD cells while more than 50 % are LIIS cells (Gatome et al., 2010). Third, non-responsive HD cells are also found in layer III. Irrespective of the anatomical identity of narrow HD cells, a local circuit that separately processes afferent HD information further could contribute to extensively integrating HD with grid and speed coding (e.g., in conjunctive grid by HD cells and broadly tuned HD by speed cells). In addition, the local segregation of specialized HD information may result in retained or even enhanced HD coding in conditions when grid firing patterns are compromised, as experimentally shown by manipulating hippocampal projections, septal projections, and local PV inputs (Bonnevie et al., 2013; Brandon et al., 2011; Miao et al., 2017).

Furthermore, the observation that speed coding was not compromised beyond the predicted level suggests that local processing is not required to further amplify or sharpen the rate-coded speed signal in mEC (see **Supplementary Discussion**). In contrast to the retained speed and HD

coding, our results support the notion that grid accuracy is reduced by processing of information within local recurrent networks. Recurrent network models of grid cells have either emphasized direct excitatory connectivity between principal cells or indirect inhibitory connectivity between LIIS cells (Burak and Fiete, 2009; Couey et al., 2013; Fuhs and Touretzky, 2006; McNaughton et al., 2006a; Pastoll et al., 2013), and both connectivity patterns have now been confirmed by pair-wise intracellular recordings from principal cells in the mEC superficial layers (Couey et al., 2013; Fuchs et al., 2016; Winterer et al., 2017). Our manipulation established that cells with both of these connectivity features (i.e., excited and inhibited, only inhibited) were perturbed by LIIP stimulation and that grid networks were not accurate during periods when inputs from other cells in the superficial layers were limited. Processing of intact afferent pathways to the superficial layers during these periods is therefore not sufficient for sustaining grid patterns, which suggests that afferent HD and speed information either needs to be further processed locally or that grid to grid connectivity is essential. If further processing of incoming information to the grid network were to completely explain our results, we would expect that all grid cells would be affected to a similar extent. However, we observed that effects on grid accuracy were most pronounced for grid cells that were most profoundly inhibited, which suggests that synaptic integration at either the level of the grid network or the level of individual grid cells was essential to selectively generate spikes in an accurate grid pattern.

Despite the profound perturbation of neuronal activity in most cells in the superficial layers and the inaccuracy in grid firing during the period of inhibition, we observed that grid location errors were not cumulative but were rather rapidly corrected. The lack of profoundly disrupted grid firing on a longer timescale corresponds to findings from other manipulations of local mEC circuits, which did also not observe that functional mEC cell types are disrupted with analysis over time periods of minutes (Buetfering et al., 2014; Kanter et al., 2017). We propose that effects on grid accuracy are short-lived because of three possibilities. First, under our recording conditions,

afferent information could rapidly reset errors introduced into the firing patterns of grid cells. For example, grid cells are known to be sensitive to changes in visual cues, box shape or box size (Diehl et al., 2017; Hafting et al., 2005; Krupic et al., 2015; Stensola et al., 2012), and it is therefore likely that a stable stream of afferent information from sensory areas, hippocampus, the contralateral mEC, or possibly even HD cells and theta oscillations, which were unaffected by our manipulation, could account for the rapid recovery. A second possibility is that the recovery of recurrent inputs within the local mEC network to baseline firing is sufficient to enable a complete correction in grid cell firing. However, this would nonetheless require that the minor neuronal activity during the period of maximal inhibition retains sufficient information such that an updated stable attractor state can be reinstated in the mEC within about ten milliseconds. Lastly, it is possible that the error correction signal arises from grid modules much further (>1 mm) away from the few modules that we were recording and perturbing. However, this seems unlikely since grid cells across modules have been shown to remap independently of each other (Pilly and Grossberg, 2014; Stensola et al., 2012) which suggests that putative attractor states are distinct for each grid module and do not strongly interact with each other.

Taken together, we find that narrow HD signals form a separate subcircuit within the superficial layers, which points to a network mechanism for separate local processing of afferent HD signals that could explain the persistence of HD signals during manipulations that alter grid firing (Bonnevie et al., 2013; Brandon et al., 2011; Miao et al., 2017). Furthermore, our results suggest computations within recurrent circuits in the superficial layers are critical for determining the precise firing location of grid cells. While processing of afferent information by recurrent circuits between grid cells have been the standard tenet of computational models for grid firing (Giocomo et al., 2011b; Zilli, 2012), our results are a critical experimental confirmation that key computations for grid accuracy are performed within the superficial layers. Finally, our results

provide evidence that, under circumstances of foraging with abundant sensory cues, any local perturbations of position accuracy are corrected on a timescale in the order of milliseconds.

Methods

Approvals: All animal experiments were approved by the University of California, San Diego Institutional Animal Care and Use Committee and conducted according to National Institutes of Health guidelines.

Animals: Wfs1-creERT2 mice were obtained from The Jackson Laboratory [B6.Cg-Tg(Wfs1-cre/ERT2)2Aibs/J, Stock No.:009614]. The expression of Cre recombinase was confirmed by breeding male Wfs1-creERT2 mice with female Ai14 reporter mice, also from The Jackson Laboratory [B6.Cg-Gt(ROSA)26Sor$^{tm14(CAG-tdTomato)Hze}$/J, Stock No.:007914], and checking the expression of at least five mice across different breeding pairs. For viral tracing procedures, we used seven heterozygous Wfs1-creERT2 (4 male, 3 female) mice. We observed no differences in the projection patterns of LIIP cells between male and female. For electrophysiology, seven heterozygous Wfs1cre-ERT2 male mice weighing between 25-32 g were used for the unilateral stimulation experiments. An additional six heterozygous male Wfs1cre-ERT2 mice were used for the bilateral stimulation experiments. All mice were between 4-8 months of age. To obtain Cre expression, mice were given three IP injections of tamoxifen (0.25 mg/g body weight, Sigma-Aldrich, T5648) over 5 days. The tamoxifen was prepared as 20 mg/ml in corn oil (Sigma-Aldrich, C8267) and stored at -20 °C. The mice were housed on an inverse 12 hr light/dark cycle (lights off at 8 am), and all recordings were done during the dark phase. Mice were provided food and water *ad libitum.* They were housed in groups (maximum 5 per cage) before surgery, but were singly housed after the microdrive implant.

Tissue processing and immunohistochemistry: Anesthetized mice were perfused with cold saline solution (0.9 %) followed by cold pre-made 4 % paraformaldehyde in PBS solution (Affymetrix USB). Brains were post-fixed for 24 hours in 4 % paraformaldehyde at 4°C and then transferred to PBS solution and subsequently sagitally sectioned (40-50 μm) on a vibrating blade microtome (Leica, VT1000 S). The sections were either mounted directly on electrostatic slides or transferred to 1x PBS for immunohistochemistry. Slides were coverslipped with DAPI Fluoromount-G (Southern Biotech, 0100-20) and imaged using a virtual slide microscope (Olympus, VS120). Sections from animals that contained tetrode tracks from the electrophysiology were then un-coverslipped, stained with cresyl violet and coverslipped with Permount (Fisher Scientific, SP15500) for better visualization of the tracks.

For sections used for immunohistochemistry, prior to the addition of primary antibodies, the slices were blocked for 1 hour at room temperature (RT) with a blocking solution comprising 10 % horse serum (HS), 0.2 % bovine serum albumin (BSA) and 0.05 % Triton-X in 1x PBS. Slices were incubated overnight at 4 °C with primary antibodies dissolved in a carrier solution made with 1 % HS, 0.2 % BSA, and 0.05 % Triton-X in 1x PBS. After overnight incubation and 4 washes for 10 min each with 1x PBS, the slices were incubated for at least 2 hours at RT with secondary antibodies in carrier solution. Next, the slices were washed four times with 1x PBS, mounted on glass slides and coverslipped with DAPI Fluoromount-G. The following primary antibodies were used, mouse anti-reelin (Millipore Cat# MAB5364, RRID:AB_2179313, 1:1000), mouse anti-reelin (MBL International Cat# D223-3, RRID:AB_843523) and rabbit anti-Wfs1 (Proteintech Group Cat# 11558-1-AP, RRID: AB_2216046, 1:1000). All secondary antibodies (AlexaFluor488 anti-mouse, AlexaFluor405 anti-rabbit, AlexaFluor488 anti-rabbit) were obtained from ThermoFisher Scientific. Sections were imaged using a virtual slide microscope (Olympus, VS120) and higher magnification images were obtained from a confocal microscope using 10x, 20x or 60x magnification lenses (Olympus FluoView, FV1000).

Fluorescence quantification: Sections containing the ipsilateral and contralateral mEC of mice injected with AAV-hSyn-FLEX-mRuby2-T2A-Synaptophysin-eGFP virus were imaged using a virtual slide microscope (Olympus, VS120) at 10x magnification. For accurate comparison, the two hemispheres of each animal (n = 3) were imaged with two laser wavelengths – 532 nm (red) and 495 nm (green) – using the same laser power and exposure time for each hemisphere. Three ipsilateral sections along the medial-lateral extent of the mEC, and three corresponding sections on the contralateral hemisphere were chosen for each animal and subsequently analyzed using Fiji ImageJ(Schindelin et al., 2012). To ensure overexpression of synaptophysin-eGFP within cell bodies on the ipsilateral hemisphere does not artificially elevate the eGFP signal, the red channel (corresponding to cell bodies and axons) was subtracted from the green channel for sections from both hemispheres. These subtracted regions were excluded from further analysis such that only eGFP expressed at synaptic terminals would be used for fluorescence quantification. Three non-overlapping regions of interest (ROIs) within LII were targeted to regions with maximal GFP expression per section, and the fluorescence density (GFP signal/area of ROI) was calculated for each ROI. The average eGFP density for each hemisphere per animal was obtained by averaging the GFP densities from the three ROIs across three sections (total 9 ROIs). Additionally, the spread of eGFP was calculated by applying the same threshold to all ipsilateral and contralateral sections per animal and determining the average area with GFP signal exceeding the threshold.

Injection of viral vectors: All mice were anesthetized with isoflurane (1.5-2.5 % in O_2) and mounted in a stereotaxic frame (David Kopf Instruments, Model 1900). Once unresponsive to toe-pinch, an incision was made, and the skull was leveled to bring bregma and lambda to the same plane. A unilateral craniotomy was made over the mEC (+0.2 AP from the transverse sinus, +3.75 ML from lambda) and a glass pipette containing the virus was slowly lowered into the brain at a 6° angle (towards anterior). For anterograde tracing, AAV-hSyn-FLEX-mRuby2-T2A-

Synaptophysin-eGFP virus (provided by Dr. Byung Kook Lim, titer: ~1.5 x 10^{15}) was injected at two locations (-1.8 DV, and -0.9 DV from the surface of the brain) with 125 nl injected at each site. The pipette was left in place for 5 minutes at the most ventral location, and then brought up to the second injection site for another injection. The injection was administered at a flow rate of 100 nl/min using a microsyringe pump (World Precision Instruments, UMP3 UltraMicroPump). For optogenetic experiments, the same injection strategy was used, but with three 200 nl infusions of AAV-EF1α-DIO-hChR2(H134R)-eYFP (provided by Dr. Byung Kook Lim, titer: ~1.6 x 10^{14}) at each site (-1.8, 1.3, -0.9 DV), either unilaterally or bilaterally. All viruses were packaged into AAV2/DJ serotypes. The constructs were allowed to express for at least three weeks before either a perfusion or a subsequent surgery to implant the mouse with a microdrive.

Microdrive building and surgery: For in-vivo electrophysiological recordings we used a microdrive with four tetrodes, each made of four 17 μm platinum-iridium (90/10 %) wires (California Fine Wire Company). The microdrive was fitted with an optic fiber attached to the tetrode bundle (optetrode(Anikeeva et al., 2012)). We assembled a custom optic fiber using a 200 μm diameter optic fiber (Thor labs, 0.50 NA multimode fiber) glued to a zirconia ferrule (Precision Fiber Products, 230 μm). The tetrodes were cut to end <1 mm deeper than the optic fiber tip in order to ensure light activation of all cells surrounding the recording site. Prior to the surgery, the tetrodes were plated with platinum to lower impedances to 125-325 kΩ at 1 kHz. Mice were prepared for surgery as described above. In order to firmly fix the microdrive and dental cement to the skull, five anchor screws were placed on the skull. A craniotomy was prepared at the implantation coordinates (+0.2 AP from the transverse sinus, +3.75 ML from lambda), and the dura was removed. Tetrodes were placed as close to the transverse sinus as possible and gently lowered ~700 μm into the brain, with the drive positioned at a 6° angle (towards anterior). In mice with bilateral stimulations, an optic fiber cannula was implanted at a depth of 0.8 mm and at a 6° angle

(towards anterior) over the contralateral mEC. The drive was then secured to the skull with dental cement, and the mice were given buprenorphine (0.02 μg/g body weight, subcutaneous) for pain relief. The mice were allowed to recover for 7 days before the start of recordings, and postoperative care was administered every day until the mice were perfused.

Recording procedures and light delivery: Mice implanted with an optetrode were trained to forage freely in an open field (75 cm x 75 cm, black walls with a prominent white cue card) placed in a room with dim lights and several distal cues. Once the mice were familiar with the recording setup, each mouse was run for at least three sessions per day – one baseline, followed by an 8 Hz or 12 Hz stimulation session, followed by a second baseline session. Each session was approximately 10 min long, but could be up to 15 min long, depending on whether the entire box had good coverage by the mouse. Recordings were performed only when well-isolated cells could be observed. Depending on the stability of cells from the previous day, tetrodes were advanced in 50 μm steps at the end of the day to ensure that the same cells were not recorded for more than 2 days in a row. Tetrodes were generally advanced until all tetrodes crossed layer I (characterized by a loss of signal, and an increase in noise), or until the end of the drive was reached (~3 mm). During the recordings, the microdrive was connected through a multichannel, head-mounted preamplifier to a digital Neuralynx recording system (Neuralynx, Bozeman, MT). A pulley system was designed to counteract the weight of the tether and headstage. Unit activity was amplified (5,000-20,000x) and band-pass filtered (0.6-6 kHz) to isolate spikes. Spike waveforms above 35-45 μV were time-stamped and digitized at 32 kHz for 1 ms. Continuous LFP was recorded from each tetrode by band-pass filtering (0.1-900 Hz) and sampling at 32 kHz. Position data of a red and a green LED located on either side of the head-mounted preamplifier were tracked at 30 Hz by a video camera mounted above the experimental area to determine the mouse's *x*-*y* position and head direction.

During optical stimulation, light was delivered to the mEC using a 473 nm wavelength Blue DPSS Laser System through a mono fiberoptic patchcord (Doric Lenses, MFP_200/240/1100-0.22_10m_FC-ZF1.25(F), 200 μm core, 0.22NA) or a branched fiber optic patchcord (BFP(2)_200/240/900-0.22_10m_FCM-2xZF1.25(F)). The output intensity was adjusted to elicit an evident response in the unit recordings while minimizing large population spikes (power was usually maintained at <1 mW at the end of the patchcord). Light was delivered at 8 Hz (either 62.5 ms ON, 62.5 ms OFF, or 10 ms ON, 115ms OFF) or 12 Hz (either 41.7 ms ON, 41.7 ms OFF, or 10 ms ON, 73.3 ms OFF) using the Neuralynx Spectralynx system. We found that altering the light ON duration had no effect on the response, and therefore combined all stimulations performed at a certain frequency, regardless of the duration of the light.

Spike sorting and cluster quality: We used a customized version of the spike sorting software MClust, MATLAB 2009b (Redish, A.D. MClust. http://redishlab.neuroscience.umn.edu/MClust/MClust.html). Clustering was performed manually in two-dimensional projections of the parameter space using waveform amplitude, waveform energy and the peak-to-valley difference. The same cell was tracked across all sessions within a day, but was not tracked across days (<10 % of all cells were recorded for more than one day). Cluster quality was assessed by calculating the L-ratio and isolation distance (**Figure 3S.1**) for each cluster across baseline and stimulation sessions(Schmitzer-Torbert et al., 2005).

Anatomical localization of cells: Based on tetrode tracks observed in cresyl violet sections, recordings for each day were localized to a certain layer of the mEC (**Figure 3S.1**). Because tetrodes in our microdrives were usually only ~100 μm apart and moved parallel to the cortical surface, precise localization to an entorhinal layer was possible in most animals. In the animals where the tetrodes crossed between layers, we localized cells to either layer II or III based on

records of the advancement of tetrodes through the brain. Electrode localization was further confirmed by the presence of population spikes in the LFP during each stimulation session, which were only prominent when the tetrodes were in LII, but not in other layers.

Stimulus response classification: Timestamps of the TTL signal for the onset of each light pulse were used to generate peri-stimulus time rasters (PSTR) and peri-stimulus time histograms (PSTH) for each cell with a time window of ±40 ms and either 0.1 ms or 1 ms time bins. All further analysis of cell responses was performed using either the PSTR or PSTH. Because individual cells could be both excited and inhibited, the two classifications were performed independent of each other (**Figure 3S.2**).

Cells excited by optical stimulation. The average firing rate within the 40 ms time window immediately before each light pulse ($Mean_{pre}$) was first calculated. Next, the firing rate in each 1 ms bin before the light pulse (-40 to 0 ms) was normalized to $Mean_{pre}$, and the bin with the maximum was selected. A cumulative distribution of these maximum baseline values over all cells was then generated. A cell was classified as excited if the normalized peak rate in any bin after the light onset (0 to 40 ms) exceeded the 95th percentile of the baseline maxima. The 95th percentile corresponded to a 1.58 fold increase (**Figure 3S.2a, b**). Once cells were classified as excited, we examined whether it was feasible to distinguish between direct ChR2 activation and indirect activation via synaptic connections with ChR2 excited cells. A parameter commonly used to classify cells as directly excited is their reliability to spike after every light pulse. However, we found that the probability of spiking was strongly correlated with the baseline firing rate of a cell (**Figure 3S.2d, e**). Because of the dependence of spiking probability on an inherent firing property of the cell, we did not consider a biased parameter useful for classification. We next asked whether it was feasible to use spike latency or spike jitter (i.e., the variability of latencies across trials) with the expectation that directly excited cells are characterized by low latencies and low jitter. The latency was defined as the first 0.1 ms time bin when the increase in the firing rate exceeded half of the peak rate after

light onset. For calculation of the jitter, the latency for the cell to first spike was determined (L_i) for each light pulse. If the cell did not spike within 10 ms, the trial was assigned NaN. The jitter was defined as the standard deviation of the latencies across all trials (**Figure 3S.2c**). We found that almost all excited LII cells responded at extremely short latencies and could not be separated into categories based on the latency. Similarly, while the jitter was more variable in our dataset, there was no obvious cutoff (**Figure 3S.2g**). The ambiguity between direct and synaptic excitation is consistent with a recent study that performed paired recordings between LIIP and LIIS cells in entorhinal slices and demonstrated that the latency of synaptic excitation between LIIP and LIIS cells can be as low as 1 ms(Winterer et al., 2017). Therefore, we considered that cells cannot be classified as directly versus indirectly excited, consistent with reports that direct excitation and synaptic excitation are not readily distinguishable in circuits with recurrent connectivity(Beyeler et al., 2016; Roux et al., 2014). However, we used direct and indirect excitation of cells in the mEC superficial layers as an opportunity to elicit feedback inhibition to perturb local circuits, similar to the rationale that has been used for electrical stimulation of recurrent collaterals(Ego-Stengel and Wilson, 2010; Jadhav et al., 2012; Moser et al., 2005; Zugaro et al., 2005).

Cells inhibited by optical stimulation. The baseline firing rate ($Mean_{pre}$) was calculated for the 40 ms window before the light pulse. Next, a 10 ms wide sliding window was advanced with a step size of 1 ms over the 40 ms before light onset, the average within each window was normalized to $Mean_{pre}$, and the window with the minimum normalized rate was selected. A cumulative distribution of these baseline values was then generated over all cells. A cell was classified as inhibited if the mean normalized rate in any 10 ms sliding window after light onset (0 to 40 ms) was less than the 95^{th} percentile of the baseline minima. The 95^{th} percentile corresponded to a decrease to 66 % of $Mean_{pre}$ (**Figure 3S.2h, i**). The latency of inhibition was defined as the 1^{st} bin of the 10 ms window with the minimum firing rate. As expected, the latency for excitation across all cells preceded the latency for inhibition (**Figure 3.2i**).

Interneuron analysis: Interneurons were distinguished from principal cells by using a minimum average firing rate cutoff of 5 Hz and a maximum peak-valley ratio of 1.3 (**Figure 3.2f**). This criterion therefore ensured that putative interneurons had a symmetrical waveform shape with approximately matching peak and valley amplitudes, as would be expected for inhibitory cells. Cells that could not be unambiguously classified were excluded from all further analyses. Interneurons have previously been divided into putative subtypes by their spike-burst magnitude(Royer et al., 2012), and we implemented the same analysis. Briefly, the burst index (BI) of each cell was defined based on the spike time autocorrelogram and these parameters were used to sort interneurons.

Spatial cell classification

Rate maps. The recording box was divided into 3 x 3 cm bins. Firing rate maps were constructed by dividing the total number of spikes in each bin by the total time the animal spent in the same bin. Rate maps were smoothed with a 5 by 5 pixel filter [0.0025 0.0125 0.0200 0.0125 0.0025; 0.0125 0.0625 0.1000 0.0625 0.0125; 0.0200 0.1000 0.1600 0.1000 0.0200; 0.0125 0.0625 0.1000 0.0625 0.0125; 0.0025 0.0125 0.0200 0.0125 0.0025], and bins that were more than 2.5 cm away from the tracked path or had a total occupancy of less than 150 ms were assigned NaNs in the rate map.

Firing field boundaries. For each rate map, field boundaries were defined on the reference map (average map from two baseline sessions and a stimulation session) by building contours from the bin with the maximum firing rate outwards until a threshold value of 0.3 times that peak rate was reached. If any peaks above 2 Hz remained, the procedure was repeated. For cells with multiple fields, contours were then recalculated simultaneously for all fields, such that the edge of each field

was defined as the contour at which the threshold value was reached or where two fields met, whichever came first.

Grid score and spatial auto-correlation. Grid cells were identified by calculating a gridness score (i.e., six-fold symmetry in a cell's spatial autocorrelation) (Koenig et al., 2011). First, rate maps were generated with 1.5 cm x 1.5 cm size bins and used to generate a spatial auto-correlation matrix. An annulus that contained the first hexagon of peaks around the center, but excluded the central peak was then retained from the matrix, and a second correlation was performed by rotating the annulus to different degrees with respect to itself. If there is six-fold symmetry, correlations at relative phase offsets of 30, 90 and 150° would be low, whereas correlations at 60, 120, 180° would be high. The gridness score was calculated as the difference between the average of the first and the average of the second set of values. Finally, we tested whether the score exceeded values from shuffled data (Diehl et al., 2017).

Head-direction score. The head direction of the animal was calculated from the angle between the two diodes in the horizontal plane (Koenig et al., 2011). The number of spikes within each 1° angular bin was divided by the time spent at that angle to generate polar plots. The mean vector length of these plots is the head direction score.

Speed score. Speed cells were classified based on speed scores (Kropff et al., 2015), which were obtained by calculating the Pearson product-moment correlation between the cells' firing rate and the instantaneous running speed in 33 ms bins (corresponding to the acquisition rate of position data). Firing rates were smoothed with a 250 ms wide Gaussian filter, and instantaneous running speed was obtained using a Kalman filter on the position data (Kropff et al., 2015).

Cell type identification. Classification of a cell as either a grid, head direction or speed cell was performed by determining whether the respective score was greater than the 95th percentile of the cell's score from shuffled data (Diehl et al., 2017). Shuffled spike trains for each cell were generated by randomly selecting a value between 20 s and 580 s and by then adding the value to

the timestamp of each spike. Spike times exceeding the total duration of a session were wrapped to the beginning of each session. Shuffling was repeated 1000 times for each cell in each session. In addition, head direction cells were further sub-classified into narrow and broad HD cells based on the finding that there was a clear cluster of narrowly tuned cells with scores > 0.5 (**Figure 3S.4**). Because each cell was recorded for at least three sessions (stimulation as well as baseline before and after stimulation), we had to account for the possibility that a cell was not consistently classified across sessions. To assign a cell to a particular functional cell type, we therefore required that the respective score was above the 95th percentile cutoff in at least two out of the three sessions.

Measuring effects of optical stimulation on spatial firing

Grid cell accuracy. Reduction of grid cell accuracy was measured by calculating the fraction of spikes outside of the grid field boundaries divided by the total number of spikes. This value could be determined over the entire recording session or for particular time intervals with respect to light pulses. For excited grid cells (including both directly and synaptically excited cells), the accuracy of spikes between 0 and 10 ms after light onset was compared to the accuracy of an equal number of randomly selected spikes between 30 and 0 ms before light onset. For inhibited grid cells, a fixed time window could not be used because the pattern of inhibition was less stereotypic than for excitation. For each cell, a window of inhibition was thus selected which began with the minimum firing rate between 0 and 40 ms after light onset and ended when the cell regained a certain percentage of its baseline firing rate (e.g., 50 %). The accuracy of all spikes during the inhibitory window (I) was compared to the accuracy of an equal number of randomly selected spikes between 30 and 0 ms before light onset (Pre).

Distance to grid nodes. The mean Euclidian distance of each spike from the closest grid field centroid was calculated for spikes during the I and Pre periods. For each cell, the Euclidian distance of an equal number of random x-y coordinates from the path of the animal was also

calculated to estimate chance distance estimates. To account for variability in grid field size, these values were normalized by the average grid spacing for each cell (i.e., average distance between the centroids of the cell's grid fields). By normalizing all Pre and I distances by the grid spacing, we could compare the relative change in the distance across grid cells, regardless of their field size. All values that included random sampling were calculated by taking the mean of 50 iterations.

Speed cell accuracy. Speed cell accuracy during stimulation sessions was calculated from a ±40 ms wide PSTR. For inhibited speed cells, the window of maximal inhibition (I) was defined as starting from the time of the minimum in the firing rate until the cell regained to 50 % of its baseline firing rate. For comparison, we also randomly extracted an equal number of spikes between 30 and 0 ms before light onset (downsampled-Pre). For each light pulse, we then performed a linear regression between the number of spikes occurring during I and the running speed closest to the video frame at the center of I as well as between the number of spikes occurring during downsampled-Pre and the running speed closest to the video frame at 15 ms before every light trial. All values that included random sampling were calculated by taking the mean of 50 iterations.

Narrow HD cell accuracy. Because narrow HD cells were generally not responsive to optical stimulation, HD tuning during optical stimulation sessions was calculated using fixed time windows. The HD score was generated for all spikes that occurred between 15 and 0 ms before light onset and for all spikes between 10 and 25 ms after light onset. The latter window was selected because it most closely matched the period when other cells showed maximal inhibition.

Broad HD cell accuracy. Because broad HD cells typically showed inhibition in response to optical stimulation, HD scores for broad HD cells were calculated for the period of maximal inhibition (from the minimum firing rate until the cell regained 50 % of its baseline firing rate) and for an equal number of randomly selected between 30 and 0 ms before light onset. To ensure that down-sampling spikes in the Pre condition did not lead to an artificial reduction in HD tuning, only

cells that had a Pre HD tuning cutoff greater than their shuffled cutoff were included in the analysis (7 cells were excluded by this criteria). All values that included random sampling were calculated by taking the mean of 50 iterations.

LFP analysis and theta modulation. For each session, the local field potential (LFP) from the tetrode with the highest mean power between 6 and 10 Hz was selected for analysis. The raw LFP signal was down-sampled to 1 kHz, and power at all frequencies was calculated using a Morlet wavelet. The average power between 6 Hz and 10 Hz was defined as the theta amplitude.

Theta modulation strength. The instantaneous theta phase was obtained from the Hilbert transform of the filtered signal between 6 and 10 Hz. Using spike and LFP timestamps, we linearly interpolated the firing phase for every spike. Theta modulation strength for each cell was defined as the mean resultant length of the distribution of firing phases. The same procedure was also used to assess spike phase preferences during stimulation. Similar to the analysis of grid and speed cells, the time window of maximum inhibition was identified for inhibited theta modulated cells (mean resultant length > 0.1 in at least 2 out of the 3 sessions). Theta modulation strength and the phase angle were subsequently calculated for spikes during the inhibition window and for an equal number of randomly selected spikes between 30 and 0 ms before light onset. Modulation strength values that included random sampling were calculated by taking the mean of 50 iterations.

Statistics. All statistical tests were conducted using MATLAB r2009b or Graphpad Prism 6. The details of tests used are described with the results. For all comparisons of baseline versus stimulation, paired comparisons or repeated measures tests were performed. Normality for all datasets was tested, and if the normality assumption was violated, an appropriate alternate test was used. For all tests involving a repeated measures ANOVA, sphericity was not assumed and

corrected for by using the Greenhouse-Geisser correction. All post-hoc tests were performed by correcting for multiple comparisons. No statistical methods were used to predetermine sample sizes, but our sample sizes are similar to those reported in relevant previous publications (Buetfering et al., 2014; Chen et al., 2016; Giocomo et al., 2011a). No blinding was used because blinding was not possible with our experimental procedures.

Acknowledgements

We thank G. de Guia for technical assistance with building microdrives. This work was supported by a Howard Hughes Medical Institute International Student Research Fellowship to I.Z., an Anandamahidol Foundation Fellowship to V.L., the Whitehall Foundation (20130571, 20140863), a Walter F. Heiligenberg Professorship to J.K.L, and by the National Institutes of Health (NS084324, NS086947, MH100349 and MH108594, NS102915, NS097772).

Chapter 3, in full, is material as it appears in *Nature Communications*, 2018, Zutshi, Ipshita, Fu, Maylin L., Lilascharoen, Varoth, Leutgeb, Jill K., Lim, Byungkook, Leutgeb, Stefan. The dissertation author was the primary researcher and author of this paper.

Appendix 3.1: Supplemental Figures

Figure 3S.1: Histology allowed for localization of recording sites to mEC LII or LIII.

(a) Fluorescent and brightfield images of all 7 animals for which speed, HD, and grid cells were analyzed. The mouse number is indicated to the top right of each panel along with the mEC layers where recording sites were located. Left of each panel, Sagittal section of the mEC with ChR2 expression in green, and DAPI in blue. Scale bar, 500 μm. Mouse 10 is an example of a Wfs1-cre mouse crossed with an Ai14 reporter line, in which all Wfs1+ cells were labelled red. Overlay of green and red confirms good viral expression and spread. In all other mice, the border between LII and LIII is easily observable by EYFP expression restricted to LII. Middle of each panel, Magnified image of the boxed region from the fluorescent section on the left, with layers of the mEC outlined by stippled lines. Red bars indicate the end of tetrode tracks. Scale bar, 200 μm. Right of each panel, The same section as used for the fluorescent image was stained with cresyl violet and imaged using a brightfield microscope. Scale bar, 500 μm. While the deeper damage along tracks is from advancing tetrodes and the optical fiber, the tears in the tissue were observed to be caused by the postmortem extraction of the implant. Shown are magnified images of the boxed area, with tetrode tracks highlighted by red bars. Scale bar, 200 μm. Based on histological confirmation of tetrode location and the continuous monitoring of tetrode history and depth, almost all cells could be unambiguously localized to either LII or LIII. (b) Examples of cluster isolation and stability. Scatterplots of the spike amplitude (peak-to-valley) on two channels of a tetrode are plotted for three recording sessions – baseline 1, stimulation, and baseline 2. Clusters of three different cells are shown, with their L ratio and isolation distance for each of the sessions provided on the right. (c, d) We ensured that cluster quality was not compromised during optical stimulation sessions by calculating L-ratio and isolation distance which are presented as mean ± SEM of all mEC cells (n = 278 cells from 7 mice) that were included in the analysis. For both metrics, there was no difference in the cluster quality between the three recording sessions (L-Ratio: Kruskal-Wallis test, $H(3) = 3.591$, $p = 0.166$; Isolation distance: KruskalWallis test, $H(3) = 1.692$, $p = 0.4292$).

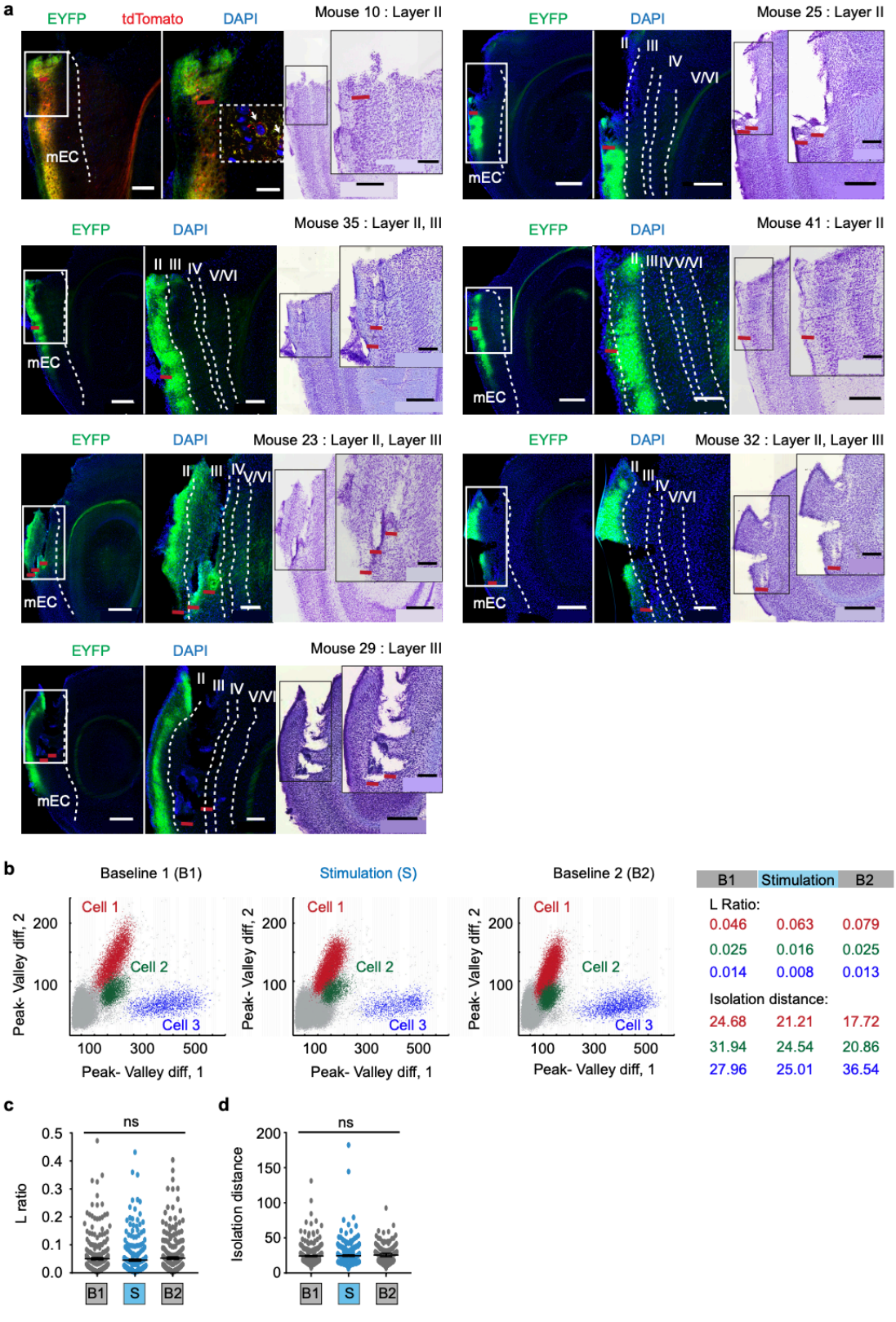
a
EYFP
tdTomato
DAPI
Mouse 10 : Layer II
mEC
EYFP
DAPI
Mouse 25 : Layer II
II
III
IV
V/VI
mEC
EYFP
DAPI
Mouse 35 : Layer II, III
II III IV V/VI
mEC
EYFP
DAPI
Mouse 41 : Layer II
II III IV V/VI
mEC
EYFP
DAPI
Mouse 23 : Layer II, Layer III
II III IV V/VI
mEC
EYFP
DAPI
Mouse 32 : Layer II, Layer III
II III IV V/VI
mEC
EYFP
DAPI
Mouse 29 : Layer III
II III IV V/VI
mEC
b
Baseline 1 (B1)
Stimulation (S)
Baseline 2 (B2)
Cell 1
Cell 2
Cell 3
Peak- Valley diff, 2
Peak- Valley diff, 1
200
100
100
300
500
B1 Stimulation B2
L Ratio:
0.046 0.063 0.079
0.025 0.016 0.025
0.014 0.008 0.013
Isolation distance:
24.68 21.21 17.72
31.94 24.54 20.86
27.96 25.01 36.54
c
L ratio
ns
0.5
0.4
0.3
0.2
0.1
0.0
B1
S
B2
d
Isolation distance
ns
200
150
100
50
0
B1
S
B2

Figure 3S.2: Description of assignment to optogenetic response categories.

(a) Peri-stimulus time histogram (PSTH, 1 ms bins for ± 40 ms before and after light onset) of an example cell. The PSTH shows a fast excitatory response followed by a longer inhibitory response. The baseline firing rate of the cell (Meanpre) was defined as the average firing rate between 40 and 0 ms before light onset. The relative increase in firing rate was then determined for the bin with the highest firing rate (Peakpost, 2.19 for the example) between 1 and 40 ms after light onset. (b) The increase in firing rate that is observed by chance was quantified by determining the maximum relative increase in firing rate during baseline (between 40 and 0 ms before light onset) for each cell (Peakpre, grey bars). The 90th, 95th and 99th percentiles of the baseline distribution over all cells are shown by the black, red, and green vertical lines respectively, and the numbers above each line correspond to the number of cells for which Peakpost (blue bars) exceeded each of these thresholds. For all further analyses that classify a cell as excited, we used the 95th percentile threshold. For visualization, the x-axis was limited to a 10-fold increase from baseline, which excluded 36 cells that were excited more than 10-fold from the display but not the analysis. (c) We examined whether cells could be classified as directly or synaptically excited by generating a peri-stimulus time raster for every light trial using 0.1 ms wide time bins extending to 10 ms after light onset. In addition, the PSTH was calculated and is shown as a line within the plot for each cell. The latency for excitation of each cell was defined as the time to reach half of the peak firing rate. For calculating the jitter, the time until the first spike after light onset (Li) was first determined and the standard deviation of single-trial times to spike was then calculated. For the example provided here, the latency was 5.7 ms while the jitter was 0.85 ms. (d) A third measure commonly used to distinguish direct versus synaptic excitation – the probability (or reliability) to spike in response to each light pulse was also calculated (i.e., the proportion of light pulses that were followed by at least one spike within 10 ms after light). However, this measure proved to be biased because the spike probability was strongly correlated with the baseline firing rate of a cell. Scatter plot of spike probability versus firing rate for principal cells (black) and interneurons (red) with solid regression lines indicating a correlation for both cell types (Spearman's rank correlation, $n = 236$ from 7 mice, $R = 0.5117$, $p < 0.0001$ and Pearson's correlation, $n = 30$ from 7 mice, $R = 0.4278$, $p = 0.0184$, respectively). (e) The same plot as in (d) but magnified for the data within the black box. A clear relationship between spike probability and firing rate was confirmed even for lower firing rate cells. (f) Examples of excited cells (PSTHs in blue), an interneuron (PSTH in red) and a non-responsive cell (PSTH in black), and their respective latencies and jitters. (g) There was no clear boundary in the latency and jitter to allow for a distinction between directly and indirectly excited cells. Therefore, cells were not classified as either directly or indirectly excited. Also shown are interneurons (red) that were indirectly excited after LIIP cell activation. The jitter and latency of these cells are interspersed with those of excited principal cells. (h) Inhibition was calculated by defining Meanpre as in (a) and by then defining Minpost as the lowest firing rate of any 10 ms sliding window between 1 and 40 ms after light onset. The onset of inhibition was the first bin of the 10 ms window with the minimum firing rate. Shown are two examples, one with a purely inhibitory response and one with an excitatory-inhibitory response. (i) The minimum firing rate during baseline (-40 ms to 0 ms) was identified and divided by the mean at baseline (Minpre/Meanpre) for each cell (grey bars). The 90th, 95th and 99th percentiles of the baseline distribution over all cells are shown by the black, red, and green vertical lines respectively, and the numbers above each line correspond to the number of cells for which the minimum between 0 and 40 ms after light onset (Minpost/ Meanpre, yellow bars) was below these thresholds. For all further analyses that classify a cell as inhibited, we used the 95th percentile threshold.

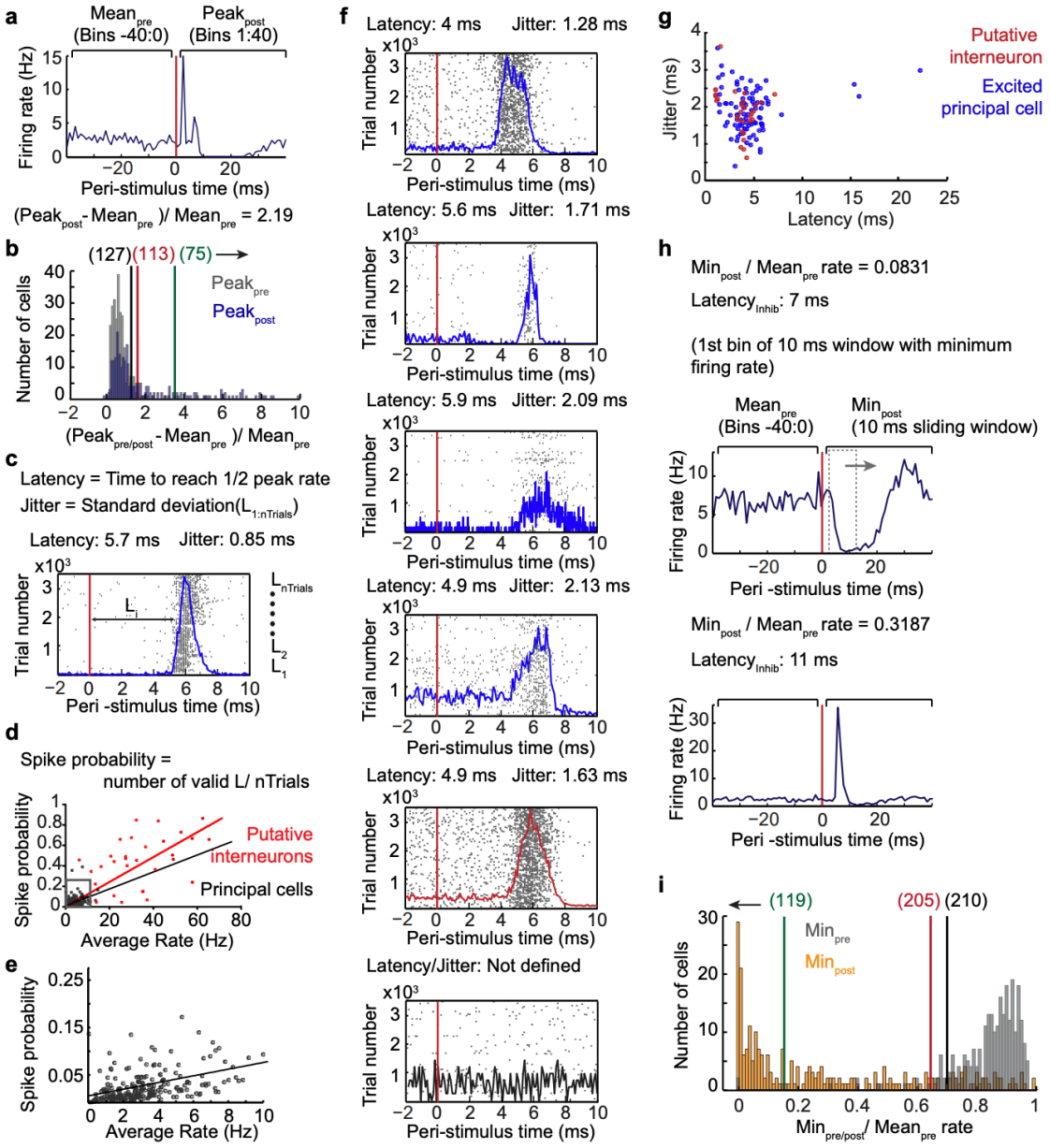
a
Mean pre (Bins -40:0)
Peak post (Bins 1:40)
Firing rate (Hz)
Peri-stimulus time (ms)
(Peak post - Mean pre)/ Mean pre = 2.19
b
(127)(113) (75)
Peak pre
Peak post
Number of cells
(Peak pre/post - Mean pre)/ Mean pre
c
Latency = Time to reach 1/2 peak rate
Jitter = Standard deviation(L 1:nTrials)
Latency: 5.7 ms Jitter: 0.85 ms
Trial number
Peri -stimulus time (ms)
d
Spike probability =
number of valid L/ nTrials
Spike probability
Putative interneurons
Principal cells
Average Rate (Hz)
e
Spike probability
Average Rate (Hz)
f
Latency: 4 ms Jitter: 1.28 ms
Latency: 5.6 ms Jitter: 1.71 ms
Latency: 5.9 ms Jitter: 2.09 ms
Latency: 4.9 ms Jitter: 2.13 ms
Latency: 4.9 ms Jitter: 1.63 ms
Latency/Jitter: Not defined
Trial number
Peri-stimulus time (ms)
g
Jitter (ms)
Latency (ms)
Putative interneuron
Excited principal cell
h
Min post / Mean pre rate = 0.0831
Latency Inhib: 7 ms
(1st bin of 10 ms window with minimum firing rate)
Mean pre (Bins -40:0)
Min post (10 ms sliding window)
Firing rate (Hz)
Peri -stimulus time (ms)
Min post / Mean pre rate = 0.3187
Latency Inhib: 11 ms
i
(119)
(205) (210)
Min pre
Min post
Number of cells
Min pre/post / Mean pre rate

Figure 3S.3: Comparisons between responses to bilateral, ipsilateral and contralateral stimulation revealed only minor effects of the contralateral projections.

(a) Sagittal sections of a representative Wfs1-CreER x Ai14 mouse with ChR2 expression (green) in both hemispheres. Wfs1+ cells are labeled in red. Middle, Magnified image of the boxed region in the image to the left highlights where single unit recordings were performed. White lines indicate the end of tetrode tracks and confirm that recording locations were restricted to LII in this mouse. Across all mice with bilateral expression (n = 6), cells were identified as recorded from either LII or LIII. Scale bar, 500 μm. (b) Schematic depicts experimental design. Mice were bilaterally injected with a Cre-dependent AAV expressing ChR2-EGFP and implanted with an optic fiber cannula over the left hemisphere and an optetrode over the right. While recording from the same set of mEC cells, stimulation was performed bilaterally as well as ipsilaterally and contralaterally from the recording site. (c) Heat maps for mEC LII cells, sorted by excitatory versus inhibitory responses. Each row corresponds to a single cell that is normalized to its peak firing rate. The sorting was performed based on the bilateral condition, and was retained for ipsilateral and contralateral stimulation sessions. The ipsilateral stimulation responses of individual cells were almost identical to the bilateral stimulation. In response to only contralateral stimulation, the cells often did not respond but occasionally showed late latency responses. The colored circles on the right indicate the response category of each cell, according to the legend in (d). (d) The 105 LII cells shown in (c) were assigned to four different categories by their responses to bilateral, ipsilateral and contralateral light stimulation. Stimulation of Wfs1+ cells in the contralateral hemisphere only led to weak and longer latency responses in a few LII cells, consistent with results from viral tracing that showed only sparse projections to the contralateral hemisphere (Fig. 1). (e) Examples of 5 cells that showed the largest amplitude responses to contralateral stimulation, with their bilateral and ipsilateral responses overlaid. In the few cells that responded to contralateral stimulation, the responses were much slower than for ipsilateral stimulation. (f) The same graphs as (c), but for cells recorded in mEC LIII. LIII cells were mostly inhibited by bilateral and ipsilateral stimulation. No responses were observed following contralateral stimulation except for 3 cells which responded by weak inhibition. The colored circles on the right indicate the response category of each cell, according to the legend in (d). (g) Quantification of responses of LIII cells in (f) following bilateral, ipsilateral and contralateral light stimulation. Color code as in (d). (h) Reponses of putative interneurons (classified as in Fig. 2f) to bilateral, ipsilateral, and contralateral stimulation. Strong excitation was only observed for stimulation ipsilateral to the recording site. The colored circles to the right indicate the response category of each cell, according to the legend in (d). (i) Quantification of the responses depicted in (h). Color code as in (d).

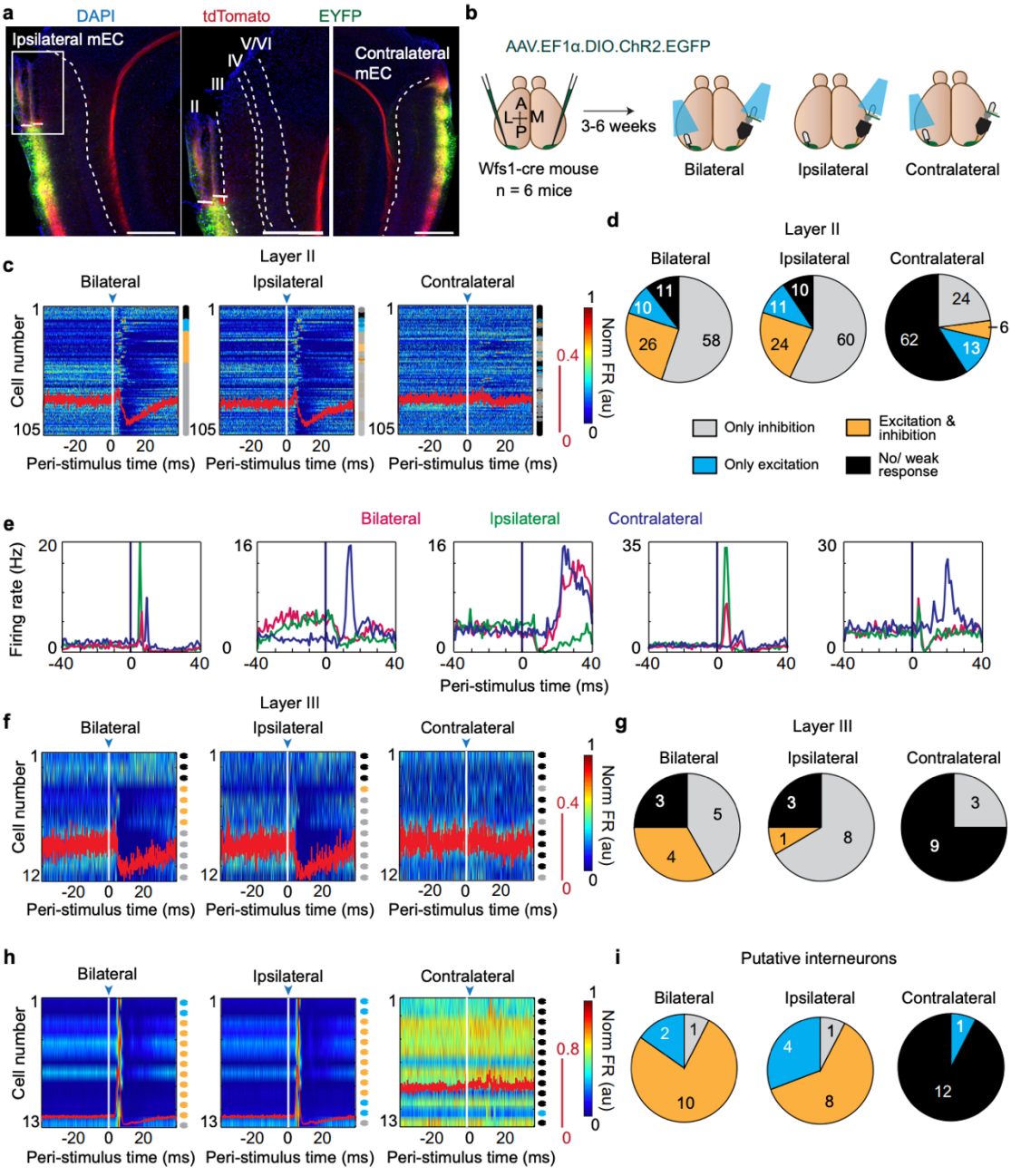
a
DAPI
tdTomato
EYFP
Ipsilateral mEC
V/VI
IV
III
II
Contralateral mEC
b
AAV.EF1α.DIO.ChR2.EGFP
A
L
M
P
3-6 weeks
Wfs1-cre mouse
n = 6 mice
Bilateral
Ipsilateral
Contralateral
c
Layer II
Bilateral
Ipsilateral
Contralateral
Cell number
Peri-stimulus time (ms)
Norm FR (au)
d
Layer II
Bilateral
Ipsilateral
Contralateral
Only inhibition
Excitation & inhibition
Only excitation
No/ weak response
e
Bilateral
Ipsilateral
Contralateral
Firing rate (Hz)
Peri-stimulus time (ms)
f
Layer III
Bilateral
Ipsilateral
Contralateral
Cell number
Peri-stimulus time (ms)
Norm FR (au)
g
Layer III
Bilateral
Ipsilateral
Contralateral
h
Bilateral
Ipsilateral
Contralateral
Cell number
Peri-stimulus time (ms)
Norm FR (au)
i
Putative interneurons
Bilateral
Ipsilateral
Contralateral

Figure 3S.4: Classification of cells into speed, HD narrow, HD broad, and grid categories.

(a) Representative examples of a speed cell, a HD narrow cell, a HD broad cell, and a grid cell. Rate maps are shown with the color scale to the right. The peak rate of rate maps is listed above each plot, and the peak rate of the polar plots is provided below each plot. The HD score is provided above each polar plot in blue. (b, c, d) Scatter plots of the maximum speed, HD and gridness scores of all LII and LIII cells across all sessions versus the 95th percentile of scores from shuffled data. The stippled line indicates the cutoff, and any cell above the cutoff was classified as positive for that score (red). For a cell to be considered positive for a certain category, it was required to be above the cutoff in at least 2 out of the 3 sessions (baseline 1, stimulation, and baseline 2). Thus, grey dots above the line are cells that were above the threshold in only one session. (b) Speed cells have a continuous distribution, yet there are also some extreme examples of speed tuning. (c) Left, HD cells could clearly be divided into two separate categories – HD narrow cells, those with a HD score > 0.5 (red), and HD broad cells, those that had a HD score above the cutoff but below 0.5 (blue). Right, Histogram of the HD scores divided by category demonstrate the bi-modality in HD scores. (d) Grid cells formed a distinct sub-population from non-grid cells. (e) Distribution of grid, border, HD, irregular spatial and non-spatial cells across all 236 principal cells. Any conjunctive HD x spatial cells were counted in their respective spatial category, and not in the broad HD cell category. (f) Distribution of the speed score versus average firing rate for all speed cells. 15 out of 47 speed cells were interneurons, whereas most of the remaining principal cells had conjunctive properties. (g) Magnification of the black boxed region in (f). The conjunctive properties of all speed cells are highlighted according to the color code in (e). (h) Scatter plots of the maximum HD score of all LII and LIII cells versus the 99-percentile of scores from shuffled data. All narrowly tuned head direction cells that were originally classified using a 95th percentile cutoff were also above the 99-percentile threshold. Of the broad HD cells (blue dots), fewer (38 rather than 58) were selected with the more stringent threshold. (i) Peri-stimulus time plot for all broad HD cells that were selected with the 99-percentile cutoff. The overall responses of the cells are similar to those observed with a 95-percentile cutoff (see Figure 6b). (j) Quantification of HD tuning of all inhibited broad HD cells (classified using a 99-percentile cutoff) shows similar results as those observed with a 95-percentile cutoff (One-way repeated measures ANOVA followed by Tukey's multiple comparisons test, n = 18 cells from 7 mice, $F(1.515, 25.76) = 9.958$, $p = 0.0014$). Significant differences between conditions ($p < 0.05$) are denoted by different letters (a, b). All summary plots show the mean ± sem.

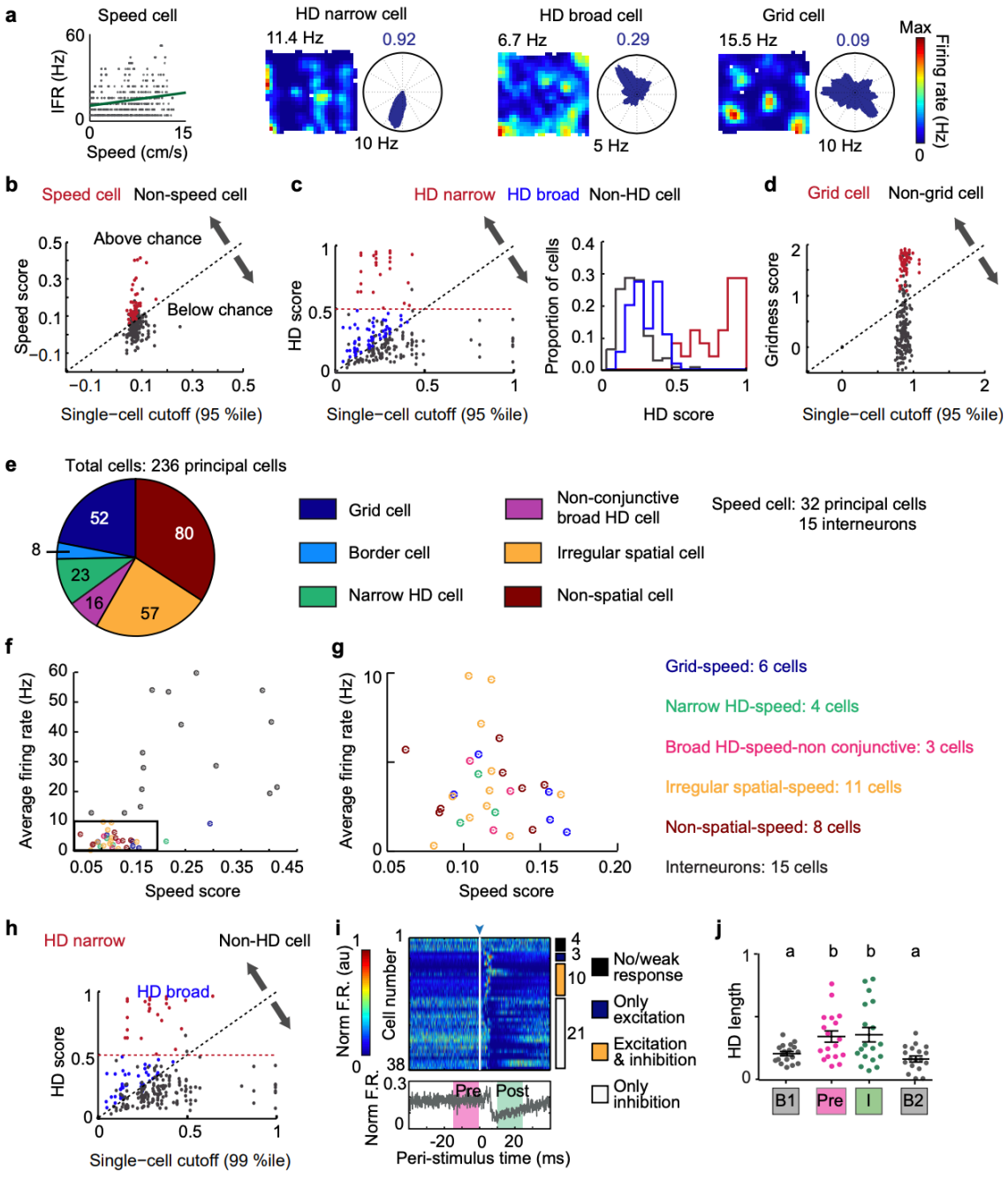
a
Speed cell
IFR (Hz)
60
0
0
15
Speed (cm/s)
HD narrow cell
11.4 Hz
0.92
10 Hz
HD broad cell
6.7 Hz
0.29
5 Hz
Grid cell
15.5 Hz
0.09
10 Hz
Max
Firing rate (Hz)
0
b
Speed cell Non-speed cell
Above chance
Below chance
Speed score
Single−cell cutoff (95 %ile)
c
HD narrow HD broad Non-HD cell
HD score
Single−cell cutoff (95 %ile)
Proportion of cells
HD score
d
Grid cell Non-grid cell
Gridness score
Single−cell cutoff (95 %ile)
e
Total cells: 236 principal cells
52
80
8
23
16
57
Grid cell
Border cell
Narrow HD cell
Non-conjunctive broad HD cell
Irregular spatial cell
Non-spatial cell
Speed cell: 32 principal cells
15 interneurons
f
Average firing rate (Hz)
Speed score
g
Average firing rate (Hz)
Speed score
Grid-speed: 6 cells
Narrow HD-speed: 4 cells
Broad HD-speed-non conjunctive: 3 cells
Irregular spatial-speed: 11 cells
Non-spatial-speed: 8 cells
Interneurons: 15 cells
h
HD narrow
Non-HD cell
HD broad
HD score
Single−cell cutoff (99 %ile)
i
Norm F.R. (au)
Cell number
4
3
10
21
38
No/weak response
Only excitation
Excitation & inhibition
Only inhibition
Norm F.R.
Pre
Post
-20 0 20
Peri-stimulus time (ms)
j
HD length
a b b a
B1 Pre I B2

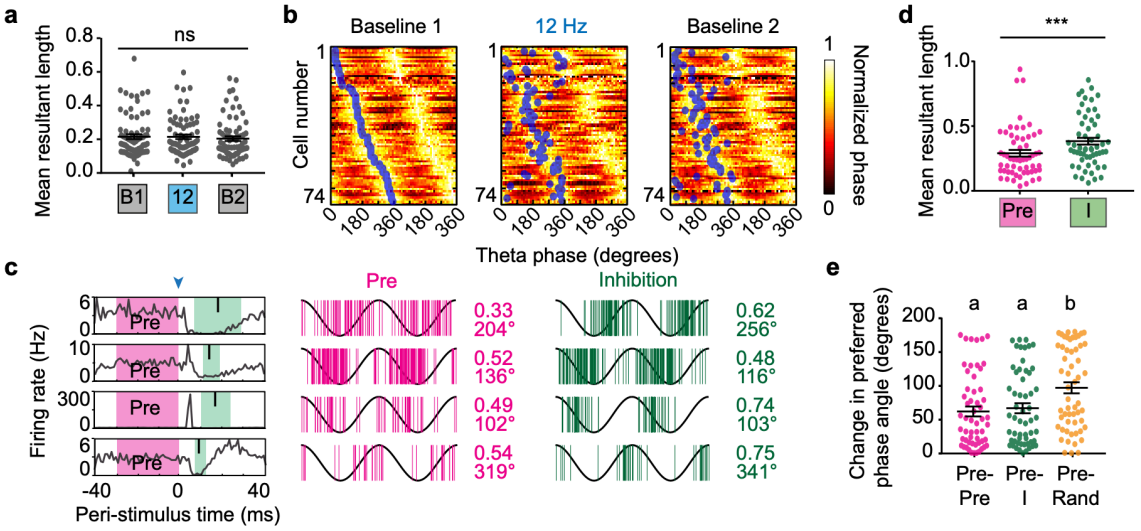

Figure 3S.5: Theta modulation and theta phase preference were preserved during inhibition.

(a) The mean resultant length for spike phase preference of theta-modulated cells (i.e., cells with mean resultant length > 0.1) was unaffected during 12 Hz stimulation sessions compared to baseline (Friedman test, n = 74 cells from 7 mice, FM(3) = 4.649, p = 0.0978). (b) The spike phase distribution of theta modulated cells was examined by ordering cells by their preferred phase angle during the first baseline. Each row corresponds to a single cell and blue circles represent each cell's peak theta phase angle. The order of cells was maintained across sessions. (c) Shown are 4 examples of inhibited theta modulated cells, where spikes during inhibition (until each cell recovered to 50% of its firing rate; I, green) were selected. An equal number of spikes were randomly selected from the period between 30 and 0 ms before light onset (Pre, magenta). The phases of each of the sets of spikes are plotted with reference to two example theta cycles, and the mean resultant length and angle for each cell is provided for Pre (magenta font) and I (green font). (d) Enhancement of theta modulation for spikes during inhibition (spike phase length: Wilcoxon matched-pairs signed rank test, n = 57 cells from 7 mice, W(57) = 815, p = 0.001). (e) The absolute difference in the preferred phase angle was estimated between I versus Pre spikes and, for comparison, between two sets of randomly drawn Pre spikes. The phase difference that could be reached if the phase difference were at chance levels was calculated by comparing Pre versus Pre spikes shuffled for cell identity. While there was some variability in the preferred phase angle between I and Pre, there was no difference to the Pre-Pre controls. For both conditions, the phase angle was more consistent than chance (Friedman test followed by Dunn's multiple comparisons test, n = 56 cells from 7 mice, FM(3) = 12.49, p = 0.0019). Significant differences between conditions ($p < 0.05$) are denoted by different letters (a, b). All summary plots show the mean ± sem. *** $p < 0.001$.

Figure 3S.6: Narrowly tuned head direction cells were recorded simultaneously with other cells that responded to the stimulation.

(a, b) Examples of tetrodes with three simultaneously recorded cells, one of them being a narrow HD cell. Top-left of each panel, Scatterplots of the spike amplitude (peak or peak-to-valley) on two channels of a tetrode, where clusters of the three different cells are shown. Bottom-left of each panel, Spectrogram of the LFP recorded on the same tetrode during the stimulation session, with power in the 12 Hz band arising due to population spikes from LIIP activation. Top-right of each panel, Rate maps and HD polar plots, with the peak rate indicated below the plot for each of the three cells. Rate maps are color coded from blue (minimum firing rate) to red (maximum firing rate). Bottom-right of each panel, PSTH of the corresponding cell during the stimulation session. While the narrowly tuned HD cells showed weak to no responses, other simultaneously recorded cells were robustly activated or inhibited, suggesting that the weak response in narrow HD cells is unrelated to ChR2 expression. (c) Several narrow HD cells were recorded on tetrodes without simultaneously recorded cells. In such cases, we confirmed robust responses to ChR2 stimulation by examining cells that were recorded on the same tetrode on days before and after the narrow HD cell recordings. This analysis confirmed that weak responses of narrow HD cells cannot be explained by weak ChR2 expression. In the example shown here, the HD cell was recorded on day 0. Two cells that were recorded on the day before were strongly inhibited, and one interneuron that was recorded on the day after was strongly excited and inhibited. (d) Spectrogram of the LFP recorded on day 0 from the same tetrode and stimulation session as (c), showing large population spiking activity at 12 Hz, suggesting that the optogenetic stimulation was effective during the session.

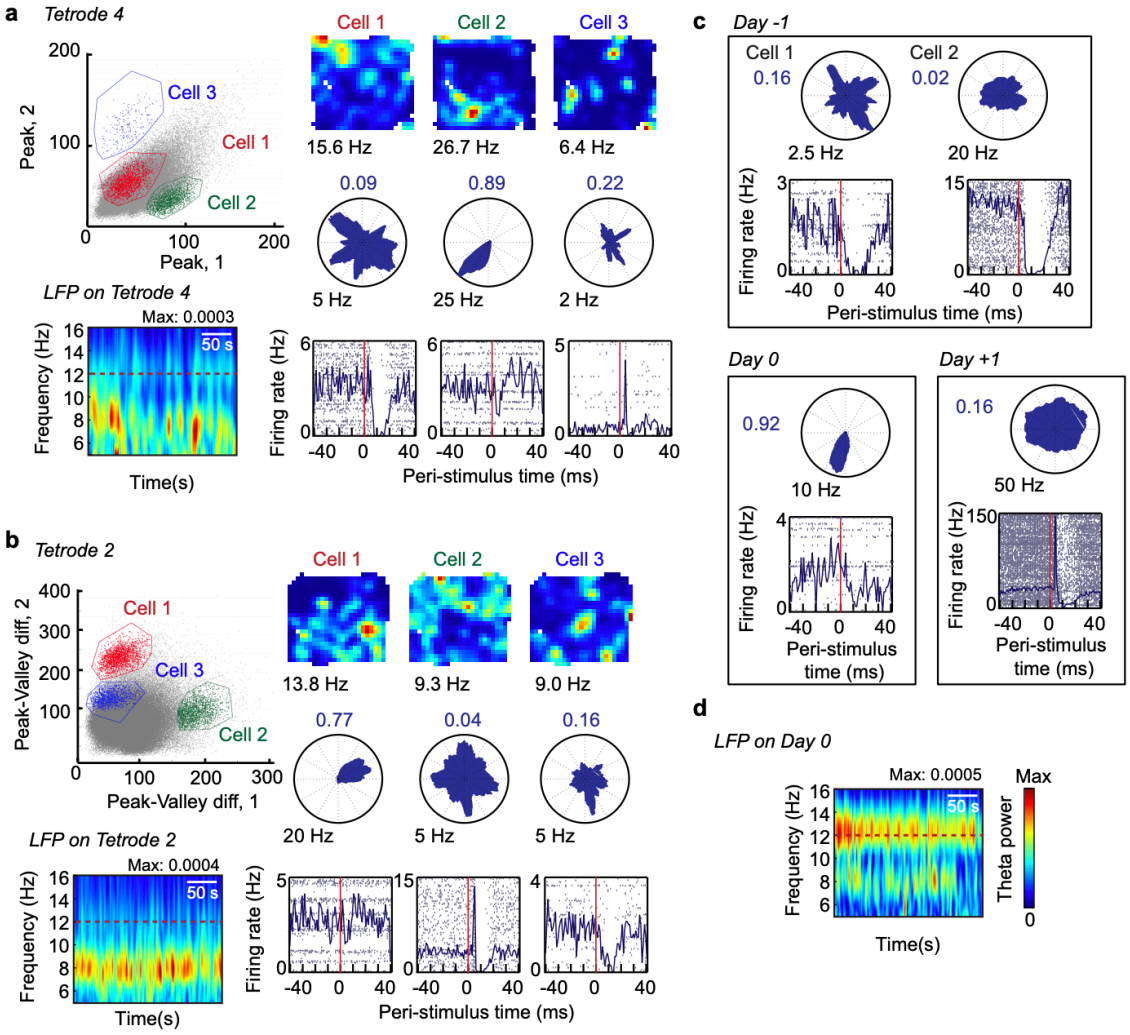
a
Tetrode 4
Cell 1
Cell 2
Cell 3
Peak, 2
Peak, 1
15.6 Hz
26.7 Hz
6.4 Hz
0.09
0.89
0.22
5 Hz
25 Hz
2 Hz
LFP on Tetrode 4
Max: 0.0003
50 s
Frequency (Hz)
Time(s)
Firing rate (Hz)
Peri-stimulus time (ms)
b
Tetrode 2
Peak-Valley diff, 2
Peak-Valley diff, 1
13.8 Hz
9.3 Hz
9.0 Hz
0.77
0.04
0.16
20 Hz
5 Hz
5 Hz
LFP on Tetrode 2
Max: 0.0004
c
Day -1
0.16
0.02
2.5 Hz
20 Hz
Day 0
Day +1
0.92
10 Hz
0.16
50 Hz
Peri-stimulus time (ms)
d
LFP on Day 0
Max: 0.0005
Max
Theta power
0

Figure 3S.7: Grid cell accuracy was transiently reduced during inhibition.

(a) Spikes that occurred during excitation (between 0 and 10 ms after light onset) exhibited substantially increased out-of-field firing (**Figure 3.7d, e**), but this value remained below chance levels, which was calculated by comparison with randomly selected path coordinates (Paired samples t-test, n = 31 cells from 3 mice, $t(30) = 6.676$, $p < 0.0001$). (b) The time window duration until 25%, 50%, 75% and 100% of the baseline firing rate was regained (**Figure 3.8e**). Post refers to the window between 100% firing rate recovery and 40 ms after light onset. One-way repeated-measures ANOVA followed by Tukey's multiple comparisons test, n = 46 cells from 3 mice, $F(1.286, 57.87) = 15.27$, $p < 0.0001$. Significant differences between conditions ($p < 0.05$) are denoted by different letters (a, b, c, d). (c) The total number of spikes that occurred during time windows until 25%, 50%, 75% and 100% of the baseline firing rate was reached (I) and during Post. One-way repeated-measures ANOVA followed by Tukey's multiple comparisons test, n = 50 cells from 3 mice, $F(1.069, 52.36) = 39.7$, $p < 0.0001$. Significant differences between conditions ($p < 0.05$) are denoted by different letters (a, b, c, d, e). (d) Scatter plot of the number of spikes that were included in the 50% inhibition time window, and the normalized average distance of those spikes from the grid node center for each cell. The two values were not correlated, suggesting that spike number did not affect the distance from defined grid nodes (Spearman's rank correlation, n = 39 cells from 3 mice, $R = -0.0443$, $p = 0.7889$). (e) Eight examples of inhibited grid cells that became less accurate during inhibition, and one (Cell 9) that appeared to remain intact. Left of each panel, Path of the animal in grey with the grid field boundaries drawn in black and the centroid of each field denoted by a blue dot. The location of each spike that occurred during the inhibition window is denoted by a green dot. The location of an equal number of randomly extracted spikes from the period between 30 ms and 0 ms before light onset are shown as magenta dots. In yellow, the location of an equal number of randomly selected points along the path of the animal are represented. The average distance of each set of locations from the grid field centroid is provided above each trajectory map. Middle of each panel, Path trajectories and grid field boundaries, with the location of all spikes between 40 and 0 ms before light onset in black. All Pre spikes were a sub-sample of these baseline spikes. Right of each panel, PSTH of the same cell with the inhibition window indicated in green and the baseline window in grey. Light onset is marked by the vertical red line. (f) Peri-stimulus time raster for all grid conjunctive HD cells, ordered by optogenetic response category. The number of cells in each response category is indicated to the right. Most grid by conjunctive HD cells showed excitatory-inhibitory responses, as also seen in the mean normalized firing rate. (g) An example grid x HD conjunctive cell and its response to optogenetic light stimulation. Rate maps are color coded from blue (minimum firing rate) to red (maximum firing rate, provided above each plot). (h) The out-of-field firing percentage of all grid x HD conjunctive cells was increased during inhibition compared to baseline (Paired samples t-test, n = 10 cells from 3 mice, $t(9) = 3.175$, $p = 0.0113$). 3 cells were excluded because they did not have any spikes during 50% recovery of their baseline firing rate. (i) The accuracy of HD tuning of all grid x HD conjunctive cells was not impaired during inhibition (Paired samples t-test, n = 8 cells from 3 mice, $t(7) = 0.4879$, $p = 0.6405$). As in Fig. 6, only cells with a Pre HD tuning above their respective shuffled cutoffs were included for the analysis. (j) The preferred HD tuning angle of all grid x HD conjunctive cells remained comparable during inhibition (Wilcoxon matched-pairs signed rank test, n = 8 cells from 3 mice, $W(8) = 22$, $p = 0.1484$). All summary plots show the mean ± sem. * $p < 0.05$, *** $p < 0.001$.

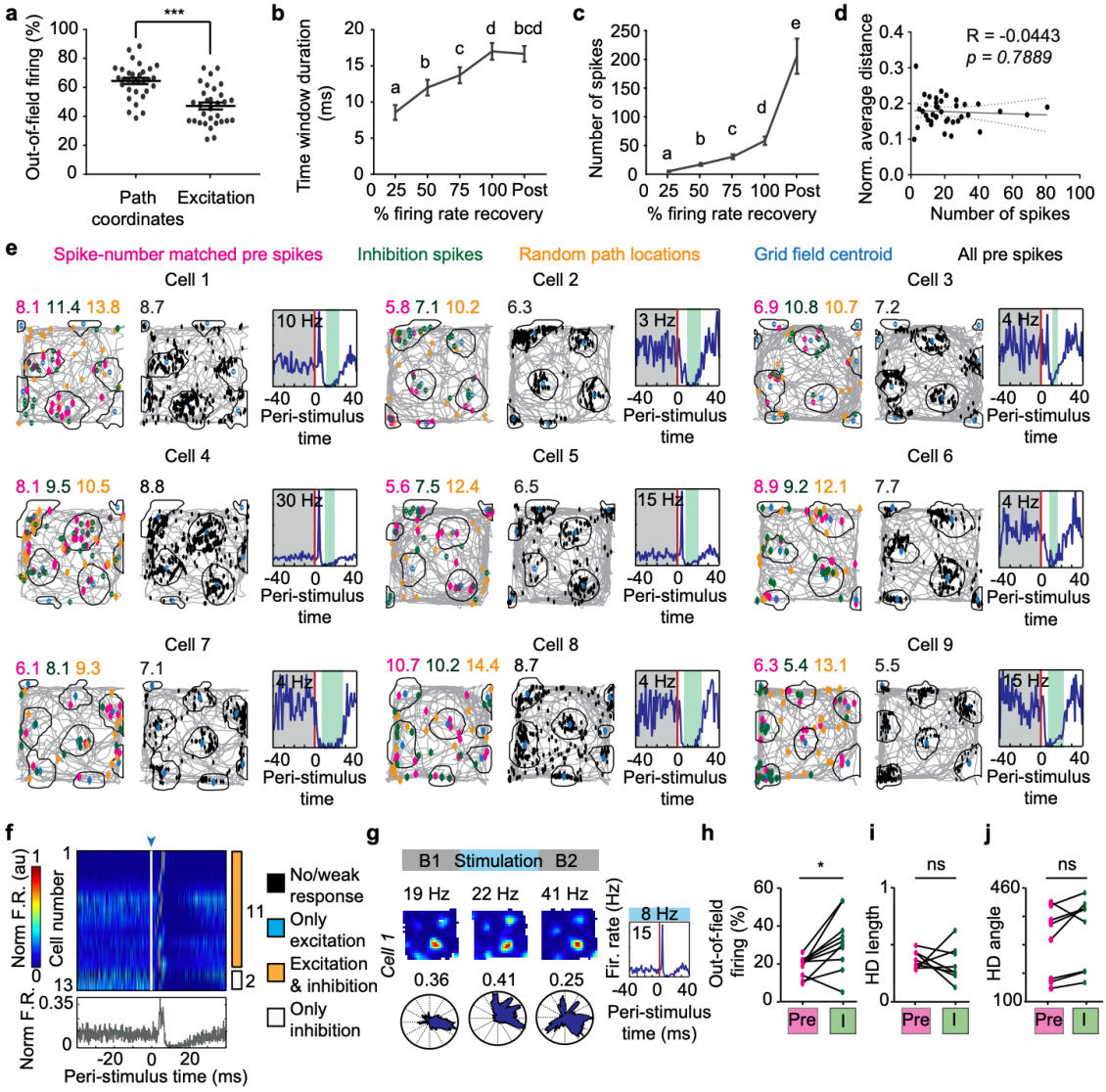
a
Out-of-field firing (%)
***
Path coordinates
Excitation
b
Time window duration (ms)
% firing rate recovery
c
Number of spikes
% firing rate recovery
d
Norm. average distance
R = -0.0443
p = 0.7889
Number of spikes
e
Spike-number matched pre spikes
Inhibition spikes
Random path locations
Grid field centroid
All pre spikes
Cell 1
Cell 2
Cell 3
Cell 4
Cell 5
Cell 6
Cell 7
Cell 8
Cell 9
Peri-stimulus time
f
Norm F.R. (au)
Cell number
Norm F.R.
Peri-stimulus time (ms)
No/weak response
Only excitation
Excitation & inhibition
Only inhibition
g
B1 Stimulation B2
19 Hz
22 Hz
41 Hz
Cell 1
Fir. rate (Hz)
8 Hz
Peri-stimulus time (ms)
h
Out-of-field firing (%)
*
Pre
I
i
HD length
ns
j
HD angle
ns

Appendix 3.2: Supplemental Tables

Table 3S.1: Distribution of recorded LII and LIII cells across all animals.

The total number of well-isolated LII and LIII mEC cells recorded from each animal and the distribution of responses of those cells to stimulation for each animal.

Animal ID	Layer	Only inhibited	Excited and inhibited	Only excited	No response	Total number of principal cells
Mouse 10	II	4	7	9	2	22
	III	NA	NA	NA	NA	0
Mouse 23	II	1	1	0	4	6
	III	7	2	1	2	12
Mouse 25	II	20	19	4	0	43
	III	NA	NA	NA	NA	0
Mouse 29	II	NA	NA	NA	NA	0
	III	14	1	0	1	16
Mouse 32	II	8	3	0	0	11
	III	21	2	0	4	27
Mouse 35	II	11	1	4	19	35
	III	2	0	1	1	4
Mouse 41	II	24	31	4	1	60
	III	NA	NA	NA	NA	0
Total	**II**	**68**	**62**	**21**	**26**	**177**
	III	**44**	**5**	**2**	**8**	**59**

Table 3S.2: Responses of cells recorded from tetrodes before and after narrow HD cells were recorded.

All narrow HD cells were ordered by their inhibitory responses, and the inhibitory responses of any cells recorded on the same tetrode as the narrow HD cell are provided. 'No turns' refers to subsequent/ previous recording days when cells changed due to tetrode drift instead of manual movement of the tetrodes. Red highlighted boxes are responses that were classified as inhibited. Yellow highlighted boxes are tetrodes where no cells before or after the narrow HD cell were recorded. Grey highlighted boxes correspond to HD scores below 0.5. Note that the most inhibited narrow HD cells (Cells 1-3) were also those that did not have consistent HD scores >0.5, suggesting that these cells are less narrowly tuned to HD.

Cell number	HD score			% Reduction in firing rate from baseline	Simultaneously recorded cell?	% Reduction in firing rate of simultaneously recorded cell	Distance from previously recorded cell	% Reduction in firing rate of previously recorded cell	Distance from next recorded cell	% Reduction in firing rate of next recorded cell
	B1	Stim	B2							
1	0.2554	0.5265	0.229	98.71	No	NA	~90 um	25.01	~75 um	64.6
2	0.3921	0.3882	0.543	71.97	Yes	34.6	No turns	42.68	No cells recorded	NA
3	0.6344	0.3477	0.4862	69.23	Yes	26.65	~50 um	50.76	~50 um	51.45
4	0.5406	0.6313	0.4415	45.82	Yes	90.53	No cells recorded	NA	No cells recorded	NA
5	0.6983	0.5704	0.5423	36.75	Yes	94.68	No cells recorded	NA	~ 100 um	17.43
6	0.8039	0.8317	0.8737	36.03	No	NA	~50 um	75.47	No cells recorded	NA
7	0.9005	0.8808	0.8855	33.33	No	NA	~50 um	96.28	~100 um	77.22
8	0.9085	0.9359	0.9363	28.62	Yes	17.04	No cells recorded	NA	~50 um	71.97
9	0.8853	0.9256	Not recorded	28.42	Yes	96.28	No turns	97.5	~50 um	33.33
10	0.7243	0.7723	0.6138	27.54	No	NA	~100 um	88.65	No cells recorded	NA
11	0.9444	0.9283	0.9339	23.94	Yes	71.97	~50 um	28.62	No turns	77.22
12	0.8308	0.9065	0.8803	21.74	No	NA	~50 um	17.43	No turns	99.47
13	0.7933	0.7956	0.7594	20.22	No	NA	~50 um	65.75	~50 um	22.46
14	0.9544	0.9525	0.9605	18.65	No	NA	~150 um	73.15	No cells recorded	NA
15	0.861	0.886	0.9325	17.96	Yes	97.5	~100 um	74.38	No turns	96.28
16	0.6354	0.6084	Not recorded	14.11	Yes	96.28	No turns	97.5	~50 um	33.33
17	0.7067	0.5941	0.4043	13.43	No	NA	~50 um	90.7	No turns	75.84
18	0.9522	0.935	0.9513	13.04	No	NA	No turns	24.29	No cells recorded	NA
19	0.9434	0.9361	0.9311	7.91	Yes	36.75	No turns	93.92	No cells recorded	NA
20	0.7735	0.8119	0.8197	5.21	No	NA	No cells recorded	NA	~100 um	62.27
21	0.8475	0.817	0.7692	5.01	No	NA	~50 um	89.74	~100 um	100
22	0.8405	0.8662	0.8401	4.79	Yes	17.04	No cells recorded	NA	~50 um	71.97
23	0.8834	0.7719	0.9226	1.29	No	NA	~250 um	73.25	No cells recorded	NA

Appendix 3.3: Supplemental Discussion

The finding that HD tuning, theta oscillations and theta modulation of cells were unaffected by our manipulation and that tuning of speed cells was only decreased to the extent predicted by the reduced spike numbers during the period of inhibition, suggests several hypotheses on how local computations may contribute to grid firing. First, intact HD information and intact theta oscillations were not sufficient to preserve grid cell firing patterns, which excludes the possibility that exclusive integration of these two signals could give rise to grid patterns. Instead, our results are more consistent with models that predict that either firing rates or theta modulation of speed cells are locally processed to give rise to grid cells(Burgess et al., 2007; Hasselmo et al., 2007; Kropff et al., 2015). LIIP cells can be considered to be an integral component of the local speed cell circuitry because LIIP cells receive rate-coded speed inputs from glutamatergic cells of the medial septum(Justus et al., 2016) and have been shown to be more speed modulated than other cell types in layer II (Reifenstein et al., 2016; Sun et al., 2015). Our manipulation resulted in a transient but substantial inhibition of speed cells, which reduced speed coding to the extent that could be predicted from the rate reduction. It is nonetheless feasible that running speed could no longer be accurately conveyed by the few remaining speed cell spikes and that the inaccuracy of grid firing emerged from the brief perturbation of the speed signal in LIIP cells. These findings could be perceived as inconsistent with reports that inactivation of the medial septal area disrupts grid firing while not only preserving, but even improving speed tuning in the mEC (Brandon et al., 2011; Hinman et al., 2016; Koenig et al., 2011). However, even though the septal inactivation improved mEC speed tuning on average, it is important to note that the speed tuning of each individual mEC cell changed to different extents. Thus, this manipulation did not merely result in a change in the gain of speed cells, but also scrambled the information. Both the previous and our findings are therefore consistent with the possibility that grid firing becomes inaccurate when relying on integrating speed information from local speed cells.

IV.

Hippocampal Neural Circuits Respond to Optogenetic Pacing of Theta Frequencies by Generating Accelerated Oscillation Frequencies

"Alice: How long is forever? White Rabbit: Sometimes, just one second."

— Lewis Carroll, Alice in Wonderland

Abstract

Biological oscillations can be controlled by a small population of rhythmic pacemaker cells, or in the brain, they also can emerge from complex cellular and circuit-level interactions. Whether and how these mechanisms are combined to give rise to oscillatory patterns that govern cognitive function are not well understood. For example, the activity of hippocampal networks is temporally coordinated by a 7- to 9-Hz local field potential (LFP) theta rhythm, yet many individual cells decouple from the LFP frequency to oscillate at frequencies ~1 Hz higher. To better understand the network interactions that produce these complex oscillatory patterns, we asked whether the relative frequency difference between LFP and individual cells is retained when the LFP frequency is perturbed experimentally. We found that rhythmic optogenetic stimulation of medial septal GABAergic neurons controlled the hippocampal LFP frequency outside of the endogenous theta range, even during behavioral states when endogenous mechanisms would otherwise have generated 7- to 9-Hz theta oscillations. While the LFP frequency matched the optogenetically induced stimulation frequency, the oscillation frequency of individual hippocampal cells remained broadly distributed, and in a subset of cells including interneurons, it was accelerated beyond the new base LFP frequency. The inputs from septal GABAergic neurons to the hippocampus, therefore, do not appear to directly control the cellular oscillation frequency but

rather engage cellular and circuit mechanisms that accelerate the rhythmicity of individual cells. Thus, theta oscillations are an example of cortical oscillations that combine inputs from a subcortical pacemaker with local computations to generate complex oscillatory patterns that support cognitive functions.

Introduction

Neuronal oscillations can arise from rhythmic activity in a small group of pacemaker cells, which impose oscillatory activity onto a broader network (Kleinfeld et al., 2014; Petsche et al., 1962; Saper, 2013). Alternatively, oscillations can also arise from cellular and synaptically driven resonance (Atallah and Scanziani, 2009; Buzsáki and Draguhn, 2004; Goutagny et al., 2009). However, there is limited knowledge on how afferent signals from neuronal pacemakers are combined with local mechanisms to give rise to the diversity of single-neuron activity. Hippocampal theta oscillations are an ideal paradigm to study this interaction, not only because of their functional relevance to memory and navigation but also because they consist of at least two oscillators at closely related frequencies (Buzsáki, 2002; O'Keefe and Recce, 1993; Skaggs et al., 1996). The spiking rhythmicity of individual hippocampal place cells occurs at a frequency that is approximately 1 Hz faster than the ongoing local field potential (LFP) frequency, and, thus, spiking exhibits a systematic phase advance across theta cycles. Theories of phase precession have proposed various mechanisms on how the frequency difference between the field potential and cellular oscillations emerges. This includes models that utilize two oscillators to achieve interference (Magee, 2001; O'Keefe and Recce, 1993) and models that use a single base oscillator in combination with an increasing ramp potential (Harris et al., 2002; Mehta, 2001; Mehta et al., 2002). Despite differences in implementation, all of these models assume that the baseline LFP theta frequency is determined by an external pacemaker. In contrast, one theory of theta generation and phase precession has questioned whether intracellular and extracellular oscillations truly arise

from different sources, and it has raised the possibility that a precisely phase-shifted summation of the faster spiking oscillations can generate the slower LFP in the theta range without an external source to generate a baseline theta frequency (Geisler et al., 2010).

Although mechanisms that support theta generation without external pacemakers have been observed at the cellular level (Alonso and Llinás, 1989) and when only local hippocampal circuits are preserved (Goutagny et al., 2009), it has long been known that long-range projections from the medial septal area to the hippocampus and medial entorhinal cortex are necessary for the presence of high-amplitude theta oscillations in awake, behaving animals. Lesions or inactivation of the medial septal area (MSA) cause a near-complete reduction of the amplitude of hippocampal and entorhinal theta (Brandon et al., 2011; Koenig et al., 2011; Mitchell et al., 1982; Mizumori et al., 1989; Wilson et al., 1978; Yoder and Pang, 2005). In further support of a pacemaker within the septal area, subsets of MSA neurons exhibit rhythmic bursting that is phase locked to hippocampal theta oscillations (Joshi et al., 2017; King et al., 1998; Petsche et al., 1962). Juxtacellular recordings from anatomically identified MSA cells suggest that these cells correspond to parvalbumin (PV)-expressing neurons in the medial septum (Borhegyi, 2004). These septal PV neurons are known to give rise to GABAergic long-range projections that terminate onto hippocampal and entorhinal GABAergic neurons, thus forming a disinhibitory circuit that is well positioned to mediate rhythmic disinhibition in hippocampal principal neurons (Freund and Antal, 1988; Gonzalez-Sulser et al., 2014; Unal et al., 2015).

Persistent theta oscillations are most prominent during locomotion (Vanderwolf, 1969), but they can also be artificially elicited in anesthetized, immobile, or slow-moving mice by rhythmic optogenetic stimulation of the MSA PV neurons or fibers (Bender et al., 2015; Dannenberg et al., 2015). Similarly, rhythmic hippocampal oscillations can also be driven by electrical stimulation of the fornix while the MSA is inactivated (McNaughton et al., 2006b; Shirvalkar et al., 2010) or by nonselective optical stimulation of septal cells (Blumberg et al., 2016;

Robinson et al., 2016). Taken together, these recordings have shown that MSA stimulation can elicit theta-like oscillations in brain states when the theta rhythm is not typically observed. However, if the MSA were the pacemaker for theta oscillations, it would be expected that stimulation does not only artificially add an oscillatory signal but also supersedes the ongoing oscillation. To test this hypothesis, we optogenetically stimulated MSA PV cells while mice were running on a track and while recording hippocampal LFP. In addition, we simultaneously recorded from place cells to examine the effects of optogenetic control of the MSA pacemaker on the oscillation frequency and phase coupling of individual cells. By performing the combined LFP and place cell recordings, we tested whether hippocampal circuits are prewired to generate an upward shift in the cellular oscillation frequency or whether cellular and LFP oscillation frequencies are controlled by separate circuit mechanisms.

Results

Optogenetic stimulation of medial septal PV neurons was sufficient to supersede endogenous theta oscillations.

Optogenetic stimulation of PV neurons in the MSA has been shown to control the hippocampal LFP frequency in anesthetized and immobile/slow-moving animals (Bender et al., 2015; Dannenberg et al., 2015). We began by testing whether using a similar strategy during behavioral states when animals normally generate high-amplitude theta oscillations is adequate for not only driving hippocampal LFP but also superseding theta oscillations that are endogenously generated during movement. Channelrhodopsin (ChR2, 10 mice; oChIEF, 5 mice) was selectively expressed in MSA PV cells using an adeno-associated virus vector (AAV-Ef1a-DIO-hChR2- eYFP or AAV-Ef1a-DIO-oChIEF-mCitrine) in parvalbumin-cre (PV-cre) transgenic mice (**Figure 4.1A**; **Figure 4S.1A**). An optic fiber (200-mm core diameter, 0.48 numerical aperture [NA]) was positioned just dorsal to the MSA for blue light laser stimulation (473 nm) at a total power of ~1–

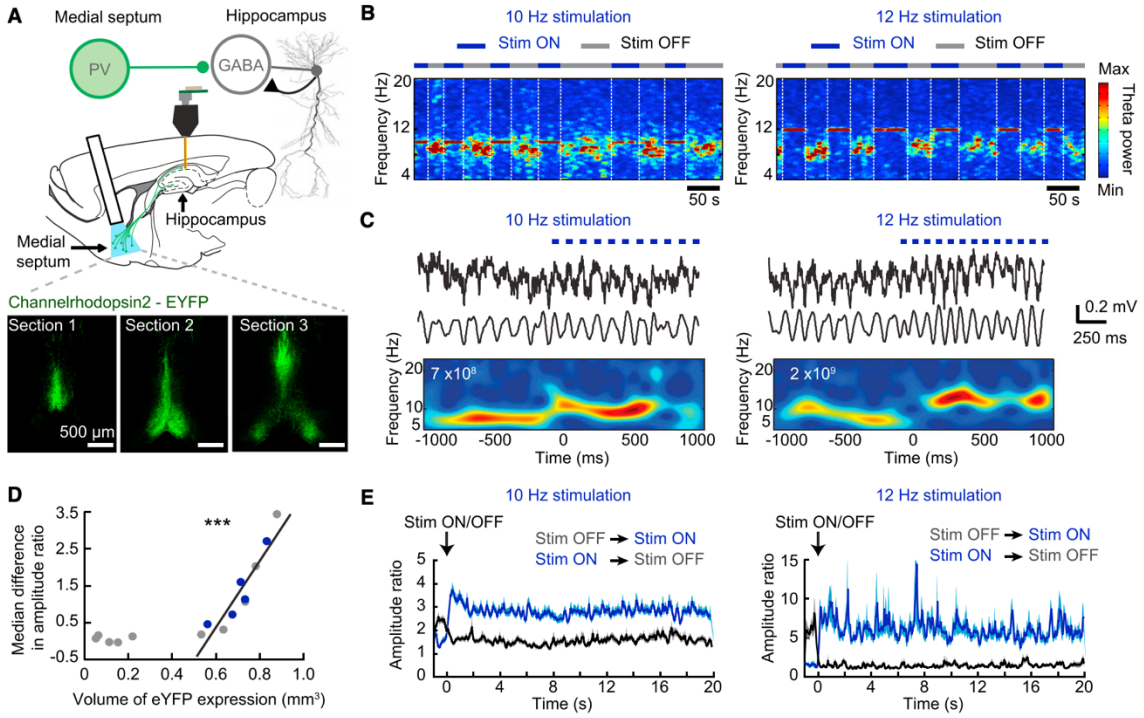

Figure 4.1. Rhythmic stimulation of medial septal PV neurons controls the frequency of theta oscillations in freely behaving mice

(A) Top: Schematic of optogenetic and recording approach during behavior on the rectangle track. Cre-dependent channel rhodopsin (ChR2) or oChIEF was expressed by targeting an AAV to the medial septal area (MSA) of PV-cre transgenic mice. Opsin-expressing PV neurons were optically stimulated while we performed recordings of CA1 cells and LFP. Bottom: Example images demonstrate how virus expression was quantified by determining the area of fluorescence in three sections along the anteroposterior axis of the MSA. (B) Example spectrograms of LFP from the CA1 region of the hippocampus as animals ran around a rectangular track. PV neurons in the MSA were optogenetically activated at either 10 Hz (left) or 12 Hz (right) on every alternate lap. White stippled lines mark the end of each lap. The LFP frequency was completely entrained to the stimulation frequency during light-on laps. (C) Example LFP traces are shown for 1 s before and 1 s after the onset of 10 Hz (left) or 12 Hz (right) optical stimulation of MSA PV neurons. From top to bottom, raw traces, bandpass-filtered (5- to 25-Hz) traces, and a wavelet transform of the traces are shown. Stimulation resulted in an increased LFP frequency within one theta cycle. White text and red color within the plot indicate maximum wavelet power. (D) Scatterplot of the volume of YFP expression in the MSA and the pacing efficiency across all animals. A linear relationship was found once the expression exceeded a minimum threshold (0.5 mm3). The blue dots correspond to mice used for single-unit analyses. (E) The average amplitude ratio of all data collected for 20 s after the onset of stimulation (ON laps, blue traces) and for 20 s after stimulation was stopped (OFF laps, black traces) at 10 Hz (left) and 12 Hz (right). ***$p < 0.001$.

2 mW (32–63.6 mW/mm2) at the tip of the fiber. In addition, a microdrive was implanted so that recording tetrodes could be advanced into the CA1 cell layer to chronically monitor LFP and the spiking of hippocampal pyramidal neurons (**Figure 4S.1B**). Animals were trained to run 10–14 laps counterclockwise on a large rectangular linear track (1.5 3 0.5 m) for sugar pellets provided at one corner (**Figure 4S.2A**). While mice were running, rhythmic blue light stimulation (50% duty cycle) was delivered to the MSA. For analysis of LFP data, we also used periods of stimulation in the home cage.

Septal control of theta oscillations depended on the extent of opsin expression

We performed rhythmic optogenetic stimulation of PV neurons in the MSA at 10 Hz (at the border of the endogenous theta frequency range) and at 12 Hz (beyond the endogenous range) to test whether we could precisely control the frequency of hippocampal field potentials while mice were running on the track. The onset of stimulation immediately caused a change in the frequency of hippocampal LFP oscillations that matched the stimulation frequency and superseded endogenously generated theta oscillations. Moreover, endogenous theta oscillations promptly returned upon the cessation of blue light stimulation (**Figure 4.1B and 1C**; **Figure 4S.1C**). Green and amber light stimulation were used as controls and had substantially less effect on theta oscillations (**Figure 4S.1D**), consistent with weaker activation of channelrhodopsin at these wavelengths (Mattis et al., 2012). In addition, we did not observe detectable pacing of theta oscillations in mice in which the expression level of the viral vectors in the septum appeared weak or absent (**Figure 4.1D**).

To quantify the relation between channelrhodopsin expression and pacing efficiency, we measured the volume of viral expression in the MSA and defined a metric for optogenetic control over theta. For the metric, we computed a wavelet-based amplitude ratio between the power within the endogenous range (7–9 Hz) and the power at the stimulation frequency (9–11 Hz for 10-Hz

stimulation and 11–13 Hz for 12-Hz stimulation) (**Figure 4S.1E**; Methods, quantification of theta pacing). As designed, the amplitude ratio clearly differentiated between stimulation and non-stimulation periods (**Figure 4.1E**; **Figure 4S.1F**). Beyond a minimum threshold for opsin expression, we found a striking linear relation between MSA volume with opsin expression and pacing efficiency (Pearson correlation, n = 10, R = 0.93, p = 0.0001) (**Figure 4.1D**). We also found no relationship between either the anteroposterior or dorsoventral position of the optic fiber and pacing efficiency (Pearson correlation, anteroposterior: n = 10, R = 0.33, p = 0.36; dorsoventral: n = 10, R = 0.069, p = 0.85) (**Figure 4S.1G and 4S.1H**). All animals that were included in subsequent analysis showed opsin expression levels in the MSA that resulted in a minimum pacing efficiency (increase in amplitude ratio of at least 0.3 compared to no stimulation).

Theta frequency was controlled by septal stimulation while theta amplitude remained modulated by running speed

Even in animals with substantial control of LFP oscillations, we noted variability in the amplitude of paced oscillations. Because pacing of PV cells during urethane anesthesia has been reported to lead to more consistent amplitudes (Dannenberg et al., 2015), we reasoned that the variability in the awake animal may be due to the running speed of the animal. With the high-temporal resolution of wavelet analysis, it was feasible to analyze the frequency and power as a function of the instantaneous running speed (computed from position sampled at 30 Hz). The wavelet analysis revealed that the LFP frequency was locked to the stimulation frequency at all running speeds but that power increased with running speed to the same extent as in no-stimulation controls (analysis of covariance [ANCOVA], 10 Hz: n = 42 sessions, $F(1,1674) = 3.5$, p = 0.06; 12 Hz: n = 39 sessions, $F(1,1551) = 2.62$, p = 0.1055) (**Figure 4.2**). The amplitude of theta oscillations thus remained subject to endogenous modulation by the running speed of the animal, while external optogenetic modulation of MSA PV-expressing neurons efficiently set the frequency of theta

oscillations. These results are consistent with models of theta generation in which the septum dictates theta frequency while cortical and/ or cholinergic inputs determine the amplitude of theta oscillations (Buzsáki, 2002; Schlesiger et al., 2015; Yoder and Pang, 2005).

Because stimulation of GABAergic septal terminals in hippocampus has previously been reported to decrease running speed (Bender et al., 2015), we next tested effects of our optical septal stimulation on movement. We observed an apparent increase in movement speed at the onset of light stimulation on the track, but control analysis revealed that the increase incidentally emerged from the condition that the animal is required to move across a boundary to initiate the light stimulation at the beginning of the lap (**Figure 4S.2A and 4S.2B**). To further confirm that light onset, when not conditional on animal movement, does not result in altered running speed, we performed recordings in the home cage where light stimulation was turned on and off at regular intervals irrespective of the animal's behavior (**Figure 4S.2C**). Under these conditions, theta frequency was effectively controlled by the stimulation, but effects on movement speed were not observed (**Figure 4S.2D and 4S.2E**). We also addressed whether the efficiency of pacing is dependent on the running speed, and we found that, at 10 Hz, pacing by MSA stimulation was particularly effective at rest and low running speeds, consistent with previous reports that theta can be paced optogenetically in this state (Bender et al., 2015; Blumberg et al., 2016) (**Figure 4S.2F**). However, at 12 Hz in the home cage and at both stimulation frequencies on the track, the pacing efficiency was found to be similar across all running speeds (**Figure 4S.2G**).

Place coding by individual hippocampal cells remained intact during optogenetic pacing of hippocampal theta oscillations

After confirming that septal stimulation resulted in pacing of theta-like oscillations, we examined the effect of pacing on the spiking activity of CA1 pyramidal cells. We optogenetically stimulated the medial septum on alternate laps to compare the same cells in light-off versus light-

on trials. This design allowed for spatial firing patterns, oscillatory patterns, and phase precession of the same set of neurons to be examined with and without stimulation. A lap-by-lap analysis of spatial maps showed a substantial but reversible spatial reorganization between stimulation and no-stimulation laps (repeated-measures one-way ANOVA, rate map stability, 10 Hz: n = 150 cells, $F(1.9, 288.9) = 121.7$, $p < 0.0001$; 12 Hz: n = 116 cells, $F(1.9, 221.8) = 105.7$, $p < 0.0001$) (**Figure 4.3A–3D**; **Figure 4S.3A and 4S.3B**).

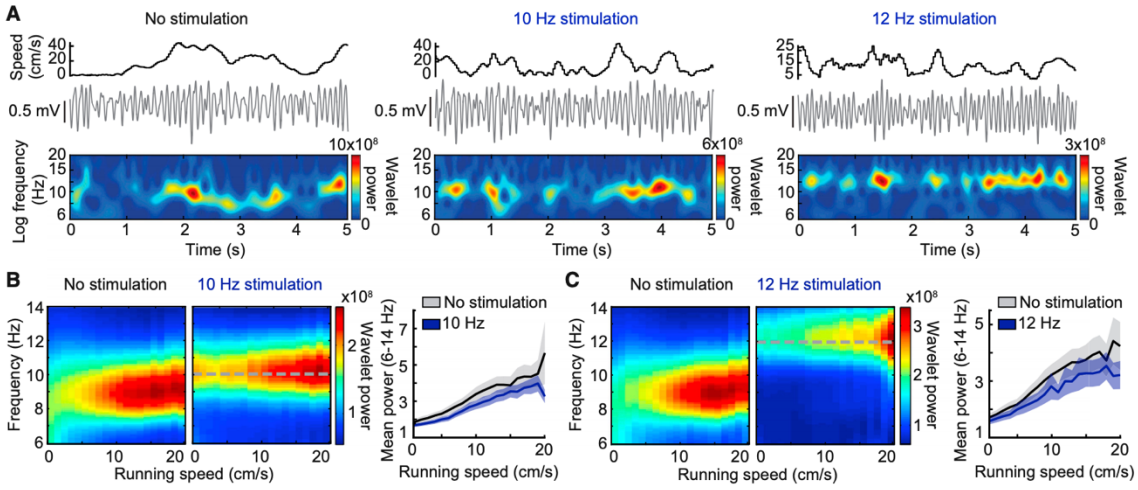

Figure 4.2. Theta amplitude increases with running speed during pacing

(A) Hippocampal LFP and wavelet power are displayed as a function of running speed for periods without stimulation, of 10-Hz stimulation, and of 12-Hz stimulation of septal PV neurons. Note that the wavelet power was highest during periods with fast running speeds in both baseline and stimulation conditions. (B and C) Left: Mean spectrograms over all recording sessions show the amplitude and frequency distribution across running speeds. Right: Mean (±SEM) normalized power of theta oscillations (averaged over 6–14 Hz) is plotted by running speed. Stimulation controlled the frequency, but it did not preclude the modulation of theta amplitude by running speed during either (B) 10- or (C) 12-Hz stimulation.

Figure 4.3. Spatial firing is preserved during optogenetic pacing of theta oscillations

(A and B) Example place fields on the track are shown for (A) 10-Hz and (B) 12-Hz stimulation sessions. Left: Path in gray with the cell's spikes overlaid as red dots, the same cell's rate map over the entire session (arrow shows the direction of running), and the cell's linearized rate map averaged independently for stimulation and no-stimulation laps are shown. The peak rate of the cell is indicated above the map. Right: Rate map of the same cell for individual stimulation ON and OFF laps is shown. Lap number is to the left of each rate map. The spatial firing patterns of the cells reliably switch back and forth between the light-on and light-off conditions. (C) A correlation matrix was computed to determine the stability of place cells across multiple laps in a session. Odd-numbered laps are light ON and even numbered laps are light OFF. The chessboard appearance of the matrix shows that rate maps were stable within light-on and light-off trials but reorganized between the two. (D) Mean (±SEM) stability of rate maps. Within light-off and within light-on stability was higher than stability between conditions. Significantly different groups are assigned separate letters (a, b, and c). (E) The firing properties of place cells (mean firing rate, peak firing rate, and number of place fields per cell) showed minor differences between no-stimulation and stimulation trials, but importantly, the spatial information of cells was not affected despite remapping during stimulation. Histograms depict mean ± SEM. (F) The positions of the fields along the linear track for all cells that were recorded during baseline and stimulation laps. Cells are ordered by their position on the track independently for the no-stimulation and the stimulation conditions. Fields were distributed along the entire track in all conditions. *$p < 0.05$ and **$p < 0.01$.

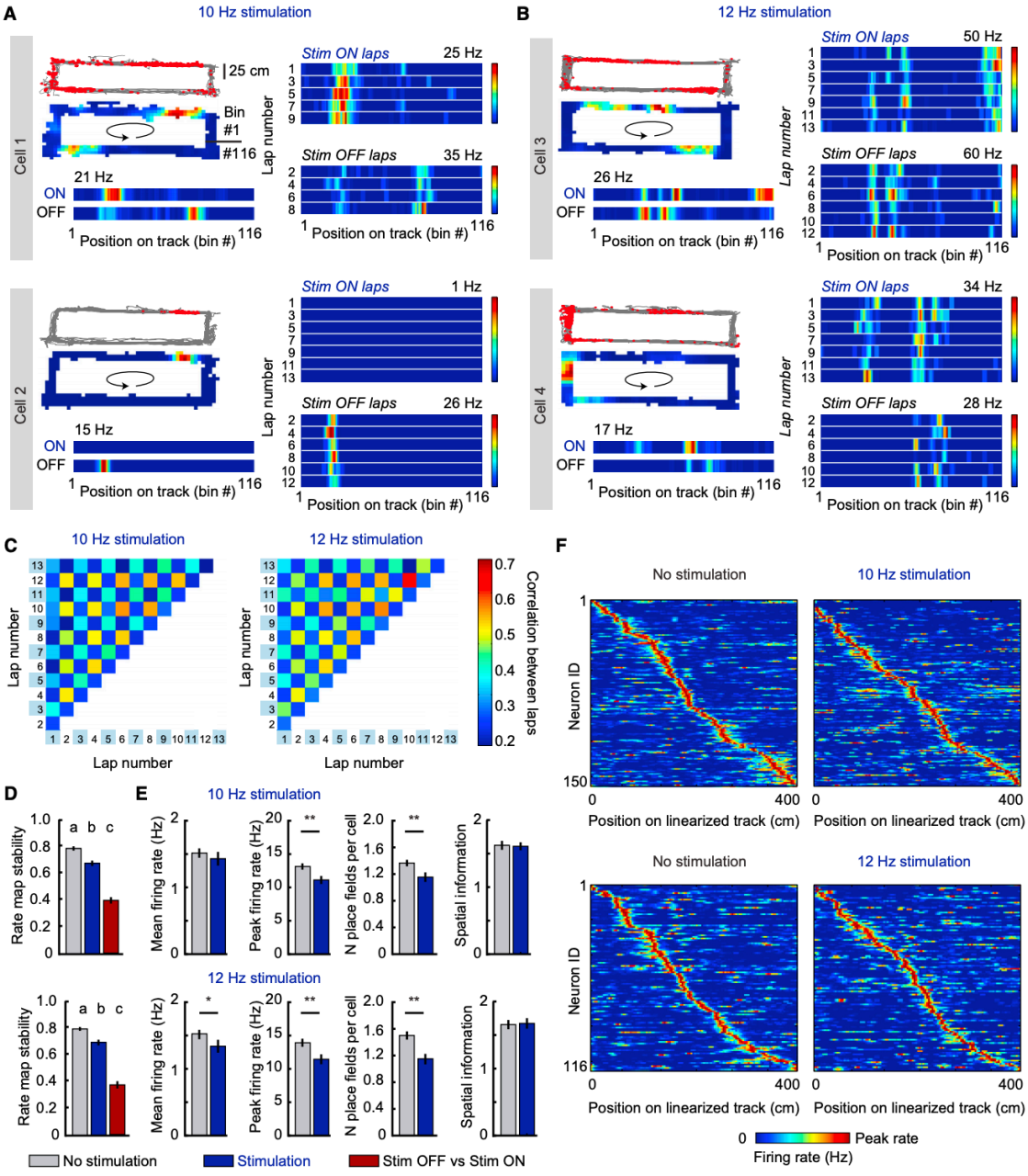
A
10 Hz stimulation
Cell 1
25 cm
Bin #1
#116
21 Hz
ON
OFF
Position on track (bin #)
Stim ON laps
25 Hz
Stim OFF laps
35 Hz
Lap number
Cell 2
15 Hz
1 Hz
26 Hz
B
12 Hz stimulation
Cell 3
26 Hz
Stim ON laps
50 Hz
Stim OFF laps
60 Hz
Cell 4
17 Hz
34 Hz
28 Hz
C
10 Hz stimulation
12 Hz stimulation
Lap number
Correlation between laps
D
Rate map stability
a b c
E
Mean firing rate (Hz)
Peak firing rate (Hz)
N place fields per cell
Spatial information
No stimulation
Stimulation
Stim OFF vs Stim ON
F
No stimulation
10 Hz stimulation
12 Hz stimulation
Neuron ID
Position on linearized track (cm)
Peak rate
Firing rate (Hz)

To determine whether this reorganization was a result of altered theta oscillations or a consequence of blue light shining into the animal's eyes during periods of optogenetic stimulation, we repeated the same paradigm in mice (n = 3) injected with a virus expressing cre-dependent GFP in the MSA. Recordings of CA1 cells in these control mice revealed that hippocampal neurons remapped to the same extent as in opsin-injected mice, while there were no optically mediated changes in their hippocampal LFP patterns (**Figure 4S.3C–4S.3F**). Therefore, differences in place fields between light-off and light-on trials arose due to sensory-mediated remapping. As expected for remapping, field locations differed but the spatial properties of the set of active cells in each condition (light-on versus light-off) remained otherwise largely unchanged. Compared to laps with no light stimulation, hippocampal neurons in opsin-expressing mice retained similar spatial coding properties and firing rates during stimulation at 10 and 12 Hz, although there were minor differences of mean rate at 12 Hz and of peak rates and the number of fields per cell at both stimulation frequencies (Wilcoxon matched-pairs signed-rank test, 10 Hz: n = 150 cells, mean firing rate, $p = 0.095$; peak firing rate, $p = 0.004$; number of fields, $p = 0.009$; spatial information, $p = 0.91$; 12 Hz: n = 116 cells, mean firing rate, $p = 0.02$; peak firing rate, $p = 0.003$; number of fields, $p = 0.0001$; spatial information, $p = 0.70$) (**Figure 4.3E**). Note that the preserved firing rates at 10 Hz and the minor decrease at 12 Hz imply that the average number of spikes per cycle decreased during optically driven compared to endogenous theta. In addition, place fields tiled the entire track for both baseline and stimulation laps (**Figure 4.3F**; **Figure 4S.3G and 4S.3H**). Thus, the preservation of spatial coding allowed us to examine the precise timing of place cell firing without the need to correct for potential confounds from differences in place field size. However, in order to account for the spatial reorganization, place field boundaries were identified independently for light-on and light-off conditions.

The frequency of spiking rhythmicity partially scaled with optogenetically induced theta oscillations

We next analyzed the relation between place cell spiking and the optogenetically controlled hippocampal LFP. First, we did not find any difference in the spiking phase preference or mean resultant length of the cells' spiking between endogenous or optically paced theta oscillations for 10-Hz stimulation and only a minor increase in the mean resultant length for 12-Hz stimulation (10 Hz: n = 210 cells, mean phase, no stimulation, 209.2 ± 8.3 degrees, stimulation 201.8 ± 8.3 degrees, Wilcoxon matched-pairs signed-rank test, p = 0.60; mean resultant length, no stimulation, 0.11 ± 0.006, stimulation, 0.12 ± 0.005, Wilcoxon matched-pairs signed-rank test, p = 0.36; 12 Hz: n = 165 cells, mean phase, no stimulation, 216.8 ± 8.7 degrees, stimulation, 225.1 ± 8.50 degrees, Wilcoxon matched-pairs signed-rank test, p = 0.999; mean resultant length, no stimulation, 0.11 ± 0.007, stimulation, 0.13 ± 0.008, Wilcoxon matched-pairs signed-rank test, p = 0.013) (**Figure 4S. 4A**).

To then examine whether septal PV stimulation exhibited control of the rhythmic frequency of place cells, we calculated the spike-time autocorrelation for each neuron, and we used a fast-Fourier transform to obtain the predominant frequency (**Figure 4.4A**). As previously reported for controls [7], the modulation frequency of the majority of principal cells (~65 %) was accelerated with respect to the endogenous LFP frequency during light-off laps. With light stimulation, there was an increase in the proportion of cells oscillating within 1 Hz above the optogenetically paced LFP frequency (10- to 11-Hz band for 10-Hz stimulation: 30% during stimulation versus 16% during no stimulation; 12- to 13-Hz band for 12-Hz stimulation: 25% during stimulation versus 11% during no stimulation) (**Figure 4.4B and 3.4C; Figure 4S.4B and 4S.4C**). These shifts in the frequency of a subset of the principal cells while their overall distribution remained broad were in contrast to a more consistent shift in the frequency of interneurons to oscillation bands slightly above the stimulation frequency (10 Hz: from 0% to 83.3% in the 10- to 11-Hz band; 12 Hz: from

Figure 4.4. The oscillation frequency of hippocampal neurons is accelerated compared to the LFP frequency during optogenetic pacing of theta-like oscillations

(A) Left: Spike time autocorrelation of two example cells (gray, no-stimulation laps; blue, stimulation laps). Right: Power calculated from the spike-time autocorrelation of the same cells shows an accelerated frequency in the stimulation condition. Variability in spiking occasionally resulted in additional oscillation peaks below the theta range, but peaks within the theta range were consistently observed. (B) Color-coded power (blue to red) calculated from the autocorrelation function of individual pyramidal cells during no-stimulation laps is compared to the mean LFP frequency (black dots). Most cells (i.e., those with peak power to the right of the black dots) were spiking rhythmically at frequencies higher than the LFP frequency during no-stimulation laps. During stimulation, the oscillation frequency of a subset of principal cells was accelerated compared to the stimulation frequency. (C) The peak frequency of each cell (blue dots) during no-stimulation laps is plotted against its peak frequency during stimulation laps. The red dotted line highlights the stimulation frequency. (D) Same as (A) but for an example interneuron recorded from the CA1 pyramidal cell layer. The rhythmicity of the interneuron was accelerated by the stimulation. (E) Same as (B) but for interneurons. Most interneurons were strongly entrained to frequencies higher than the LFP frequency during 10- and 12-Hz stimulation. (F) Phase precession slopes of three example cells during no-stimulation laps (top) and 10-Hz stimulation laps (bottom). Precession was calculated with reference to endogenous frequency during no-stimulation laps and with reference to the paced frequency during stimulation laps. For each cell, the linearized rate map on the track is provided to the right with the field used for calculating phase precession marked by a black bar. Cell 3 is an example of a field that remaps to a new location during stimulation and where the new field reliably phase precesses. Significantly negative slopes are highlighted by noting the slope in red font. (G) Top: Histogram depicting the slopes of all fields during no-stimulation laps (gray), overlaid with only the significant slopes in black. Bottom: Histogram depicts the slopes of all fields during 10-Hz stimulation laps (gray), overlaid with only the significant slopes in blue. (H and I) Same as (F) and (G), respectively, but for cells recorded during 12-Hz stimulation sessions.

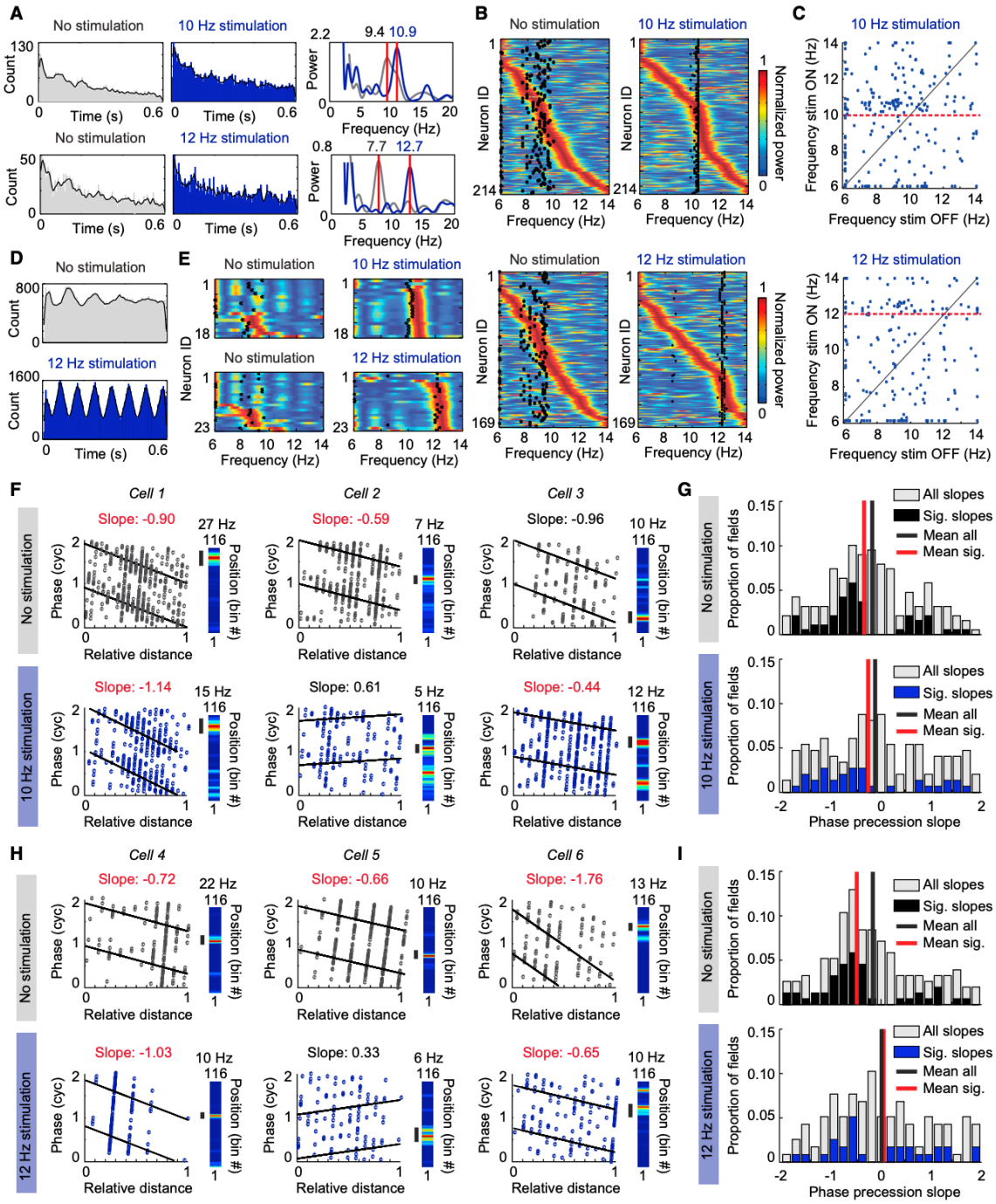
A
No stimulation
10 Hz stimulation
12 Hz stimulation
Count
Time (s)
Power
Frequency (Hz)
B
Neuron ID
Frequency (Hz)
Normalized power
C
Frequency stim ON (Hz)
Frequency stim OFF (Hz)
D
E
F
Cell 1
Cell 2
Cell 3
Slope: -0.90
Slope: -0.59
Slope: -0.96
Slope: -1.14
Slope: 0.61
Slope: -0.44
Phase (cyc)
Relative distance
Position (bin #)
G
All slopes
Sig. slopes
Mean all
Mean sig.
Proportion of fields
Phase precession slope
H
Cell 4
Cell 5
Cell 6
Slope: -0.72
Slope: -0.66
Slope: -1.76
Slope: -1.03
Slope: 0.33
Slope: -0.65
I

0% to 78.3% in the 12- to 13-Hz band) (**Figure 4.4D and 3.4E**; **Figure 4S.4D and 4S.4E**). We thus found that the acceleration was more consistent for interneurons in the pyramidal cell layer than for the population of pyramidal cells.

Importantly, these results also demonstrate that the cumulative proportion of principal cells that were spiking at frequencies above the predominant LFP frequency was lower during optogenetic stimulation compared to no stimulation (10 Hz: 56% during stimulation versus 66% during no stimulation; 12 Hz: 32% during stimulation versus 63% during no stimulation) (**Figure 4S.4C**), which would predict that phase precession with reference to optically driven oscillations is reduced. We therefore next examined whether hippocampal neurons retained phase precession in conditions with accelerated LFP frequency. We found that the average slope of phase precession was negative during no-stimulation laps but that phase precession was, on average, not retained during rhythmic optical stimulation at either 10 Hz (fields with significant slopes: no-stimulation laps, n = 54/207, stimulation laps, 36/175; mean ± SEM of all slopes: no-stimulation laps, 0.19 ± 0.07, one-sample t test against slope of zero, $t(188) = 2.84$, $p = 0.005$, stimulation laps, 0.08 ± 0.09, one-sample t test, $t(148) = 0.93$, $p = 0.35$) or 12 Hz (fields with significant slopes: no-stimulation laps, n = 48/174, stimulation laps, 29/133; mean ± SEM of all slopes: no-stimulation laps, 0.18 ± 0.08, one-sample t test, $t(153) = 2.25$, $p = 0.026$, stimulation laps, 0.01 ± 0.10, one-sample t test, $t(115) = 0.078$, $p = 0.94$) (**Figure 4.4F–4I**). Because cells no longer showed a consistent relation to LFP during 10- and 12-Hz stimulation, it can be expected that the temporal organization among the cells in the population is substantially disrupted.

Discussion

We investigated how hippocampal circuits responded to the pacing of theta oscillations by rhythmic optogenetic stimulation of MSA PV neurons. We found that stimulation controlled the frequency of hippocampal theta throughout the entire range of running speeds in freely moving

mice. The finding that septal pacing of only PV neurons could supersede the endogenous theta oscillator is the most definite evidence so far for the hypothesis that these neurons function as a pacemaker for theta oscillations in the hippocampus. Interestingly, we also found a dissociation between the control of theta frequency and theta amplitude. The amplitude of the oscillations remained modulated by running speed (Rivas et al., 1996) while the frequency was optogenetically controlled. Most strikingly, analysis of the firing patterns of hippocampal CA1 cells revealed complex interactions between the neuronal pacemaker for theta oscillations and local hippocampal computations. Rather than phase locking to the septal stimulation, a subset of hippocampal principal cells and most interneurons in the pyramidal cell layer responded with accelerated oscillation frequencies compared to the optogenetically imposed oscillation frequency. Taken together, our findings show that the MSA PV cells set the base frequency for LFP theta oscillations while local hippocampal mechanisms generate partially accelerated rhythmic spiking frequencies in response to oscillatory subcortical input to the network.

In agreement with previous studies, we confirmed that hippocampal theta oscillations could be controlled by stimulation of septal long-range projections to the hippocampus. However, previous studies showed these effects in anesthetized, headfixed, or immobile/slowly moving mice (Bender et al., 2015; Dannenberg et al., 2015; Fuhrmann et al., 2015; Vandecasteele et al., 2014) or in rats only during immobility/slow movement (Blumberg et al., 2016) or while the endogenous septal oscillator was not active (McNaughton et al., 2006b; Shirvalkar et al., 2010). The previous studies therefore showed that septal stimulation is sufficient for eliciting hippocampal LFP oscillations, but the conclusion that the septum is the pacemaker for endogenous theta oscillations requires that ongoing theta oscillations can be reliably occluded by septal stimulation. Here we show that it is possible with ChR2 and oChIEF expression in a high fraction of septal PV cells to fully pace oscillations at any running speed, which strongly suggests that we had control over a key element of the endogenous oscillator. In particular, the effectiveness of optogenetic pacing

increased with increasing volume of medial septal opsin expression, which indicates that increasingly complete septal control over oscillations can supersede other endogenous oscillatory inputs to hippocampus, such as from the supramammillary nucleus. While we identified that control over frequency can be gained by stimulation of MSA PV cells, the relation between oscillation amplitude and the animal's running speed was not altered. The dissociation between frequency and amplitude is consistent with the possibility that amplitude is not controlled by PV cells but rather by cholinergic mechanisms or entorhinal inputs, or a combination thereof (Bragin et al., 1995; Lee et al., 1994; Schlesiger et al., 2015; Yoder and Pang, 2005). Furthermore, the retained relation between oscillation amplitude and running speed, while we applied rhythmic optical stimulation during a wide range of speeds, also indicates that there were minimal indirect or circuit effects of our manipulations on neural mechanisms that control amplitude.

In addition to finding that septal PV neurons controlled hippocampal LFP frequency, we also found that the rhythmic stimulation generated an upward shift in the cellular oscillation frequency, which was more pronounced for interneurons than for principal cells. An elegant theoretical model by Geisler et al. (Geisler et al., 2010) proposed that there is a direct coupling between the lower LFP frequency and the somewhat higher oscillation frequency of individual hippocampal cells. In their model, they considered that the next subpopulation of active hippocampal cells is activated with a delay, which adds to the cycle time of the cellular oscillator such that a secondary LFP oscillation with a longer cycle time and thus a lower frequency emerges. Although our findings are not consistent with the proposed dependence of the slower on the faster oscillator, we find effects in the reverse direction, with the slower frequency as the primary frequency, which then engages local mechanisms that generate a coupled but accelerated secondary oscillation in interneurons and a small subset of principal cells. Furthermore, the retention of a broad range of frequency differences between the LFP and the remaining principal cells also shows that septal pacing does not simply result in the phase locking of hippocampal principal cells, in

contrast to what has been shown when local hippocampal PV cells or long-range GABAergic projections from entorhinal cortex are directly optogenetically stimulated (Melzer et al., 2012; Royer et al., 2012). It can, therefore, be inferred that the preserved wide range of oscillation frequencies, along with the emergence of upward-shifted oscillations in only a subpopulation of cells while LFP oscillations are paced, is likely the result of the indirect targeting of principal cells by septal afferents through multiple local interneuron types in different hippocampal subregions (**Figure 4S.4F**) (Freund and Antal, 1988; Frotscher and Léránth, 1985; Joshi et al., 2017; Unal et al., 2015).

The decoupling of cellular oscillators from a single pacing frequency raises the question about the nature of the local cellular or circuit mechanisms that give rise to the second oscillation frequency. One of the early models for phase precession (Harris et al., 2002; Magee, 2001; Mehta, 2001; Mehta et al., 2002) proposed that the accelerated frequency can emerge by combining a base inhibitory oscillation with a ramping excitation in excitatory cells. A prediction of the model is that it allows for oscillatory inhibition to generate an accelerated frequency for any cell that shows ramping excitation. Together with intracellular recording studies that showed that intracellular membrane potentials ramp up as a cell's place field is traversed (Harvey et al., 2009), our results support that this class of models may apply to the small subpopulation of principal cells that was accelerated beyond the optical stimulation frequency. However, intracellular recordings did not only show excitatory ramps but also revealed membrane potential oscillations that were tightly phase locked to the precise spike timing of the cells (Harvey et al., 2009). Because our optogenetic pacing frequency differed in most cases from the frequency of the cellular oscillations, the pacing could not have directly imposed oscillations that are synchronized with the spike timing of hippocampal principal cells. The observed dissociation between spike timing and the stimulation frequency thus suggests that intracellular oscillations are generated more indirectly than by direct coupling to the septal pacemaker. For example, once time differences in spiking compared to the

base frequency have emerged in a subset of principal cells, these oscillatory inputs could be propagated within the entorhino-hippocampal network through inhibitory interneurons, such that a combination of ramping inputs and oscillatory interference determines spike timing (Harvey et al., 2009; Jaramillo et al., 2014; Leung, 2011).

While many of the local circuit and cellular mechanisms for generating neuronal oscillations remain to be determined, our findings establish that two separate types of oscillations emerge within the hippocampus. Only the LFP frequency, which is thought to arise from synaptic currents (Einevoll et al., 2013), strongly depended on the pacemaker input from medial septal GABAergic cells. At the same time, the synaptic oscillations that were phase locked to the stimulation frequency did not result in a phase locking of interneurons within the CA1 cell layer but rather in a consistent acceleration of these cells. The emergence of dual oscillations with a faster cellular than LFP frequency is consistent with the possibility that dendrite-targeting interneurons are paced by the subcortical inputs while interneurons within the cell layer continue to mediate feedback inhibition of principal cells and, thus, remain synchronized to the local cellular oscillations (**Figure 4S.4F**). Taken together, our results therefore support both dual oscillator and ramping models of phase precession and that the complexity of the endogenous oscillation patterns may emerge from interactions between both mechanisms. Furthermore, we show that only the synaptic oscillations are directly controlled by the septal pacemaker while more complex local oscillatory patterns in CA1 are only indirectly and partially controlled by these inputs. These results do not only advance our understanding of the emergence of complex biological oscillators but also indicate that optogenetically controlling theta oscillations leaves many aspects of hippocampal circuit function intact. Such retained network behavior while artificially controlling a neural pacemaker has important implications for the potential use of brain stimulation therapies to treat memory disorders, and it suggests that improvements may in particular be achieved when returning the system to a state during which multiple oscillators can effectively interact. For example, theta

oscillation frequency in animal models of Alzheimer's disease differs from controls (Goutagny et al., 2013), and our data suggest that artificial stimulation of the medial septum could restore an important aspect of the complexity of cortical oscillations in the theta frequency band.

Methods

Experimental model and subject details: Eighteen male parvalbumin-cre transgenic mice (129p2-Pvalbtm1(cre)arbr/J, obtained from Jackson Laboratories), 2-6 month old, weighing 25-35 g, were subjects in this study (10 ChR2, 5 oChIEF, 3 GFP). Animals were housed individually in Plexiglas cages, maintained on a 12-h light/12-h dark cycle at >90 % of the ad libitum weight, and given free access to water. All surgical and experimental procedures were approved by the Institutional Animal Care and Use Committee at the University of California, San Diego and conducted according to NIH guidelines.

Surgery: Animals were implanted with a 16-channel microdrive aimed at the hippocampus and a fiber optic aimed at the medial septal area. Anesthesia was induced with a mixture of 3 % vaporized isoflurane in oxygen, and buprenorphine (0.02 mg/kg) was then administered for analgesia. Animals were continuously monitored for the level of anesthesia and were generally maintained at 1.5-2.0 % isoflurane for the duration of surgery. One anchor screw that was positioned just anterior and lateral to lambda was used as a recording ground. A Hamilton syringe or a glass pipette was used to deliver two 400 nL bolus injections of a cre-dependent viral vector (AAV1.EF1a.DIO.hChR2(H134R)-eYFP.WPRE.hGH, AAVDJ.EF1a.DIO.oChIEF-mCitrine, or AAVDJ.EF1a.DIO.eGFP) into the MSA (AP: +1.0 mm, ML: 0.7 mm, DV: 4.8 mm and 4.2 mm; angled 10 degrees medially). A custom assembled fiber optic was then lowered to a position just dorsal to the medial septum and secured in place to the anterior anchor screws (AP: +1.0 mm, ML: 0.7 mm, DV: 3.5 mm, angled 10 degrees medially). To implant the microdrive, a craniotomy was

performed directly above the right hippocampus (AP: 1.9 mm, ML 1.8 mm), and the dura was removed. The microdrive was lowered to make contact with the dorsal surface of the brain and Neuroseal was applied to the remaining brain surface. The microdrive was then secured to the skull with a thick layer of dental acrylic. Tetrodes were lowered ~0.5 mm below the dorsal surface at surgery. Animals were sutured if necessary and were returned to their home cage for monitoring. Animals were allowed five days of recovery prior to behavioral testing.

Neurophysiology equipment and recordings: Single-units and local field potentials were recorded using the chronically implanted microdrive, which contained four recording tetrodes (bundles of four 17 micron platinum-iridium (90/10%) wires). Tetrodes were gradually lowered to the CA1 pyramidal cell layers by rotating a thumb screw on the microdrive. A preamplifier (unity-gain operational amplifier located on the head stage) and tether connected the microdrive to a digital data acquisition system (Neuralynx, Inc.). A pulley-system was designed to counteract the weight of the tether and headstage. For single-units, recording tetrodes were targeted to the CA1 pyramidal layer. Signals were amplified (5,000-20,000 x) and bandpass filtered (600-6,000 Hz) to isolate spiking events. Spike waveforms above a trigger threshold (25-55 mV) were time-stamped and digitized at 32 kHz for 1 ms. LFP signals were band-pass filtered (0.1-9,000 Hz), sampled at 32,000 Hz, and amplified (5,000-20,000 x; Neuralynx, Bozeman, MT).

Experimental design: Recordings were conducted as animals ran 10-14 laps counterclockwise on a rectangle track. The rectangle track [150 3 50 cm with a track width of 10 cm] was constructed of black Plexiglas. Translucent guiderails (3 cm) were installed and a thin rubber sheet was applied to the track floor. The track was positioned in the center of a cue-rich room that contained a white light in one corner to serve as an orienting landmark. Following

recovery from surgery, animals were trained daily on the track for a minimum of one week prior to recordings while tetrode tips were gradually advanced to the CA1 pyramidal cell layer.

Position estimation: To track the position of the animal during each recording session, a ceiling-mounted video camera detected an array of light emitting diodes (LEDs) mounted on the recording head stage just above the head of the animal. The position of the LEDs was sampled at 30 Hz and the rat's x-y coordinate was calculated as the centroid of the LED array. Up to five consecutive missing samples, due to occlusion of the LEDs or reflections in the environment, were replaced by linear interpolation of position before and after the lost samples.

Optogenetic laser stimulation: A fiber optic patch cord was secured to the recording tether and connected to an OEM diode pumped steady state laser (DPSS, 473 nm wavelength). The DPSS laser was triggered with a TTL sent directly from a custom microprocessor controlled by MATLAB through the Neuralynx NetCom development library. To control the output of the laser based on the animal's position on the track, position data collected by Cheetah was passed directly into the MATLAB environment. The entire maze was divided into 116 3.5 cm-wide bins. A custom script determined whether the animal crossed a user-defined boundary on the track. Based on these calculations, the MATLAB script would then turn the laser on and off every alternate lap. Either 10 Hz or 12 Hz-stimulation was performed during each recording session. Laser stimulation was performed at a total power of ~1-2 mW (32-63.6 mW/mm2) at the tip of the fiber. Light power above 2 mW did not further increase the efficacy of theta pacing.

Postmortem confirmation of recording locations: Tetrodes were not moved after the final recording session. Animals were overdosed with Sodium Pentobarbital and perfused intracardially with phosphate-buffered saline and then 4 % formaldehyde. Brains were extracted and stored in 4

% formaldehyde at 6°C for at least 24 hours. Approximately 24 hours prior to slicing, brains were transferred into a 30 % sucrose solution for cryoprotection. A microtome was used to obtain coronal sections through the MSA and hippocampus. Hippocampal tissue was mounted on glass slides and stained with cresyl violet. Tetrodes that recorded well-isolated neurons were confirmed to have terminated in or near the principal cell layer of region CA1 (**Figure 4.S1B**). Medial septum tissue was mounted using VectaShield medium and imaged. Fluorescent microscopy confirmed that viral vector expression was robust and restricted to the MSA (the lateral septum does not contain PV-expressing neurons) and that the tips of fiber optics were just dorsal to or within the medial septum in animals with robust viral expression (**Figure 4.1A and 3.1D, Figure 4.S1A, 3.S1G, and 3.S1H**).

Quantification of viral vector expression and optic fiber placement: Sections containing the MSA of mice injected with a cre-dependent viral vector (AAV1.EF1a.DIO.hChR2(H134R)-eYFP.WPRE.hGH or AAVDJ.EF1a.DIO.oChIEF-mCitrine) were imaged using a virtual slide microscope (Olympus, VS120) at 10x magnification using the same laser power and exposure time. Three sections (0.24 mm apart) along the antero-posterior extent of the MSA were chosen for each animal and subsequently analyzed using Fiji ImageJ. One region of interest (ROI) was drawn around the medial septum, and two ROIs were drawn around the diagonal band of Broca in each hemisphere. The area of virus expression was calculated by subtracting the background from each image and calculating the area of opsin expression above a threshold of 0. The volume of opsin expression was then calculated by adding the area across the three sections per animal and multiplying by the distance between the sections. In addition, the depth of the optic fiber was determined from the section with the tip of the optic fiber cannula by calculating the distance from the top of the cortex to the tip of the optic fiber cannula.

Single unit identification: Methods for cluster cutting and cell tracking were the same as described previously (Brandon et al., 2011). Briefly, single-units were manually isolated offline using MClust, MATLAB 2009b (Redish, A.D. MClust. http://redishlab.neuroscience.umn.edu/MClust/MClust.html). Neurons were separated based on the peak amplitude, peak-to-valley amplitude, and energy of spike waveforms. Evaluation of the presence of biologically realistic inter-spike intervals, temporal autocorrelations, and cross correlations was used to confirm single-unit isolation. Neurons that were not separable in cluster space were removed from the analysis.

Amplitude ratio score: Local field potentials (LFPs) obtained from the hippocampus were referenced to ground. For each experiment, LFP from the tetrode with the highest mean power between 5-10 Hz was selected for analysis. A Morlet wavelet was used to compute the power across frequencies. LFP was downsampled to 500 Hz, and an amplitude ratio (**Figure 4.1E, Figure 4.S1E**) was calculated, defined as the ratio of power within a ± 1 Hz band of the stimulation frequency to power in the endogenous frequency band of 7-9 Hz. This permitted a sample-by-sample metric for determining the efficacy of optogenetic control of the LFP oscillation frequency.

Place field characterization: Position on the rectangular track was linearized into 116 3.5 cm-bins for analysis of spatial properties of hippocampal neurons. Rate maps were then computed as the number of spikes per time spent in each spatial bin and were smoothed by a pseudo-Gaussian kernel with a standard deviation of 1 bin. Spatial information was calculated as,

$$I = \sum_{i=1}^{N} p_i \frac{F_i}{F} \log_2 \frac{F_i}{F},$$

where I is the spatial information in bits/spike, pi is the probability of occupancy in bin I, Fi is the mean firing rate for bin I, and F is the mean firing rate. Rate map stability was determined by

calculating the correlation between rate maps for the 1st half of trials compared to the 2nd half of trials. Place fields were defined as cells that had a peak spatial firing rate greater than 5 Hz, and maintained > 20 % of the peak rate for at least 20 cm and less than 140 cm. Cell were classified as principal cells if they had an average firing rate < 5 Hz, and as interneurons if their average firing rate exceeded this threshold.

Single-cell temporal autocorrelations and frequency: For each cell, spike times were binned at a sampling rate of 500 Hz. The temporal autocorrelation between spike times was calculated from the resulting vector. The power spectrum of the temporal autocorrelation was obtained via the Chronux function mtspectrumumc() using a padding factor equal to six powers of 2 over the sample size. The single-cell frequency was then taken as the frequency with maximum power in the 6-14 Hz range.

Theta phase detection and phase precession analysis: We used a waveform-based estimation of theta phase as described in ref. (Belluscio et al., 2012). For each tetrode in the CA1 cell layer, the LFP signals were bandpass filtered between 1-60 Hz and used to find peaks, troughs, and zero crossings. Theta peaks were defined as 0 degrees, troughs as 180 degrees, and zero crossing as 90 and 270 degrees. We then interpolated phase values between these phase quadrants. Using these phase values, phase precession was then analyzed as described in detail in ref. (Schlesiger et al., 2015). Briefly, place fields were normalized between 0 and 1 from the beginning to end of the field. A circular-linear regression was then generated for spikes occurring within the bounds of the place field, and the slope of the regression line is reported. Data was analyzed separately for when laser stimulation was on or off, and analysis included within-session comparisons between 10 Hz-stimulation laps and no-stimulation laps or a comparison between 12 Hz-stimulation laps and no-stimulation laps. The data that are reported in the main text used

boundaries of ± 2.0 cycles to constrain the circular-linear regression, as in ref. (Schlesiger et al., 2015). We also repeated the analysis with the more conservative boundaries of ± 1.1 and ± 1.6 cycles and obtained matching results irrespective of the choice of parameter value (boundary of ± 1.1, 10 Hz: fields with significant circular-linear regression: no stimulation laps, n = 44/207, stimulation laps, 22/175; mean ± SEM of all slopes: no stimulation laps, 0.10 ± 0.05, one-sample t test against slope of zero, $t(167) = 2.24$, $p = 0.026$, stimulation laps, 0.06 ± 0.05, one-sample t test, $t(129) = 1.41$, $p = 0.16$; boundary of ± 1.1, 12 Hz: fields with significant circular regression values: no stimulation laps, n = 35/174, stimulation laps, 23/133; mean ± SEM of all slopes: no stimulation laps, 0.17 ± 0.05, one-sample t test, $t(142) = 3.62$, $p = 0.0004$, stimulation laps, 0.09 ± 0.06, one-sample t test, $t(102) = 1.61$, $p = 0.11$; boundary of ± 1.6, 10 Hz: fields with significant circular-linear regression: no stimulation laps, n = 47/207, stimulation laps, 31/175; mean ± SEM of all slopes: no stimulation laps, 0.13 ± 0.06, one-sample t test against slope of zero, $t(176) = 2.29$, $p = 0.023$, stimulation laps, 0.08 ± 0.07, one-sample t test, $t(136) = 1.15$, $p = 0.25$; boundary of ± 1.6, 12 Hz: fields with significant circular regression values: no stimulation laps, n = 42/174, stimulation laps, 27/133; mean ± SEM of all slopes: no stimulation laps, 0.17 ± 0.06, one-sample t test, $t(148) = 2.62$, $p = 0.009$, stimulation laps, 0.08 ± 0.07, one-sample t test, $t(105) = 1.055$, $p = 0.29$).

Quantification and statistical analysis: All statistical comparisons were calculated using MATLAB r2015b. Wilcoxon's paired, two-sided sign rank test (signrank, MATLAB) was used when comparing firing properties between no-stimulation and stimulation conditions. This test does not assume normality. An analysis of covariance (ANCOVA) test was performed to test for changes in speed modulation of theta power across running speed. Two-sided one-sample t tests were used to compare phase precession slopes to the null hypothesis that the slope is equal to zero.

Acknowledgements

We thank Dr. B.K. Lim for providing viruses for the optogenetic experiments. We also thank C. Hyde, J. Davis, V. Yazdani, and G. DeGuia for technical assistance. This work was funded by NIH FMH096531A to M.P.B.; Howard Hughes Medical Institute International Student Research Fellowship to I.Z.; NIH R01 MH100349 to J.K.L.; and Whitehall Foundation 2012-0685 and NIH R21 MH100354, R01 NS102915, R01 NS097772, and R01 NS084324 to S.L.

Chapter 4, in full, is material as it appears in *Current Biology*, 2018, Zutshi, Ipshita, Brandon, Mark P., Fu, Maylin L., Donegan, Macayla L., Leutgeb, Jill K., Leutgeb, Stefan. The dissertation author was a primary researcher and author of this paper.

Appendix 4.1: Supplemental Figures

Figure 4S.1: Histology of viral-induced expression, tetrode recording locations and quantification of pacing efficiency.

(A) Representative coronal section through the MSA with the end of the optic fiber track marked by a white arrow. The depth of the optic fiber (stippled white line) was measured for each animal. (B) Tetrode recording tracks for two representative mice. All tracks were confirmed to terminate in the dorsal CA1 region. Black arrows point to the tetrode track in the hippocampus and red lines demarcate the final position of the tetrode tip. (C) Optogenetic pacing is effective across a broad range of frequencies. Optogenetic stimulation was performed on the rectangle track in 1 Hz steps (from 1-20 Hz) for a duration of 5 seconds per step. The color-coded frequency spectrum demonstrates a near one-to-one relation between stimulation frequencies >6 Hz and LFP frequencies, but endogenous theta frequency was predominant during stimulation at lower frequencies. (D) Green and amber laser stimulation was used to control for the possibility that light stimulation would exert unspecific control over hippocampal theta oscillations. Left: Wavelet spectrograms of green and amber light stimulation confirm a lack of hippocampal theta pacing. Right: Amplitude ratios did not differ between baseline and stimulation with green or amber light. (E) Schematic depicting the calculation of the amplitude ratio. Using the wavelet- based power, the ratio between the endogenous band (violet stripe, 7-9 Hz) and the stimulation band (red stripe, 11-13 Hz for 12 Hz stimulation) was calculated on a moment by moment basis for stimulation (blue line) and no stimulation (black line) periods. The red bar that is highlighted by the black arrow denotes the difference in the median amplitude ratio between no-stimulation and stimulation periods. (F) CDF plots highlight that amplitude ratios were substantially increased during optogenetic stimulation at 10 Hz and 12 Hz across all mice combined. (G) Scatter plot of the anteroposterior (AP) position of the optic fiber (from bregma) and the pacing efficiency for each animal. Blue dots correspond to the mice that were used for single unit analyses, and red dots were the mice with low virus expression, which were not included in the correlation analysis because pacing would not be expected in these mice for any fiber position. (H) Scatter plot of the depth of the optic fiber (from brain surface) and the pacing efficiency for each animal. Blue dots and red dots as in G.

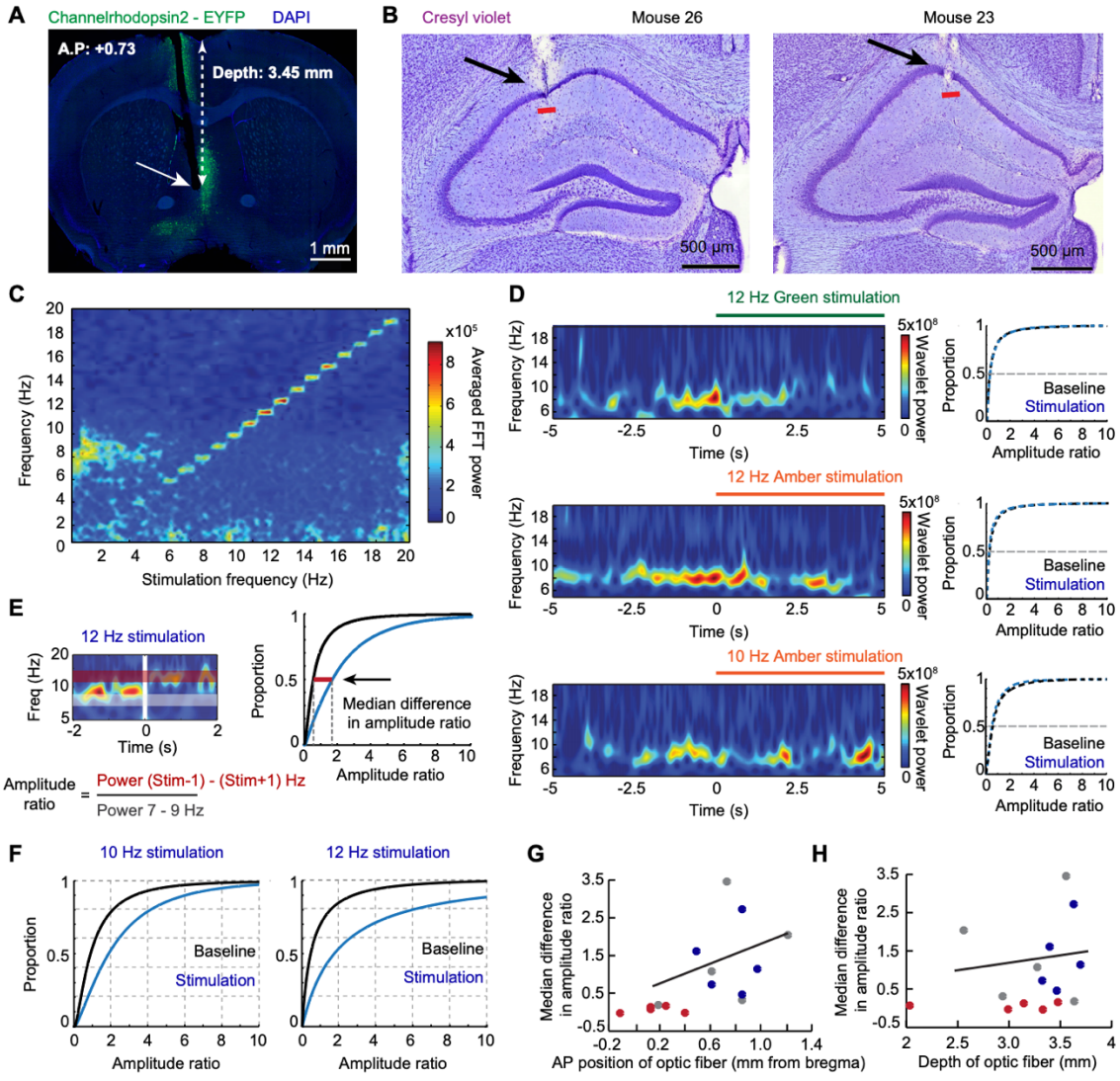
A
Channelrhodopsin2 - EYFP
DAPI
A.P: +0.73
Depth: 3.45 mm
1 mm
B
Cresyl violet
Mouse 26
Mouse 23
500 µm
500 µm
C
Frequency (Hz)
Stimulation frequency (Hz)
x10^5
Averaged FFT power
D
12 Hz Green stimulation
12 Hz Amber stimulation
10 Hz Amber stimulation
Frequency (Hz)
Time (s)
5x10^8
Wavelet power
Proportion
Amplitude ratio
Baseline
Stimulation
E
12 Hz stimulation
Freq (Hz)
Time (s)
Proportion
Median difference in amplitude ratio
Amplitude ratio
Amplitude ratio = Power (Stim-1) - (Stim+1) Hz / Power 7 - 9 Hz
F
10 Hz stimulation
12 Hz stimulation
Proportion
Baseline
Stimulation
Amplitude ratio
G
Median difference in amplitude ratio
AP position of optic fiber (mm from bregma)
H
Median difference in amplitude ratio
Depth of optic fiber (mm)

Figure 4S.2: Effects of optogenetic stimulation of MSA PV neurons on running speed and theta oscillations.

(A) Schematic of the circular track used for behavior. Animals were trained to run around the track to obtain a reward in one corner, while light stimulation was turned on or off at the marked site on every other lap. Black arrow shows the direction of running. The site that is demarcated by the red arrow (control zone) was used for analysis shown as a red line in (B). (B) Running speed over time is shown for laps when the stimulation was turned on (blue) and laps when the stimulation was turned off (black) across all mice. In both cases, there was an apparent increase in running speed when the light turned on/off (time 0). To test whether the increase resulted from the requirement that the animal always had to be moving across a boundary for the laser status to change, we selected an arbitrary boundary along the track (control zone in A) and calculated the running speed relative to the time when the animal crossed into the control zone. An apparent increase in running speed was found even in this case, confirming that the observed changes in running speed emerged from the criterion that movement across a boundary was required to change the laser status. (C) Because behavior on the track required a contingency for laser stimulation to turn on (i.e., crossing a boundary), we also performed recordings in the home cage with optical stimulation at fixed intervals (5 s ON, 25 s OFF). As for the track, example spectrograms of recordings in the home cage show that the LFP power shifted to the stimulation frequency during this paradigm. (D, E) Left, Average running speed aligned to the 5-s light stimulation at 10 Hz and 12 Hz. There was no change in the running speed upon light onset (blue, light on period). Right, Average amplitude ratio aligned to the 5-s light stimulation at 10 Hz and 12 Hz. Onset of rhythmic optical stimulation led to a rapid and reversible shift of the LFP frequency. (F) Scatter plot of the amplitude ratio versus running speed at stimulation onset during recordings in the home cage (Spearman rank correlation, 10 Hz stimulation: $n = 127$ stimulation onsets, $R = -0.25$, $p = 0.005$; 12 Hz stimulation: $n = 125$ stimulation onsets, $R = -0.025$, $p = 0.78$). (G) Scatter plot of the amplitude ratio versus running speed at stimulation onset during recordings on the track (Spearman rank correlation, 10 Hz stimulation: $n = 241$ stimulation onsets, $R = 0.011$, $p = 0.86$; 12 Hz stimulation: $n = 226$ stimulation onsets, $R = -0.047$, $p = 0.48$).

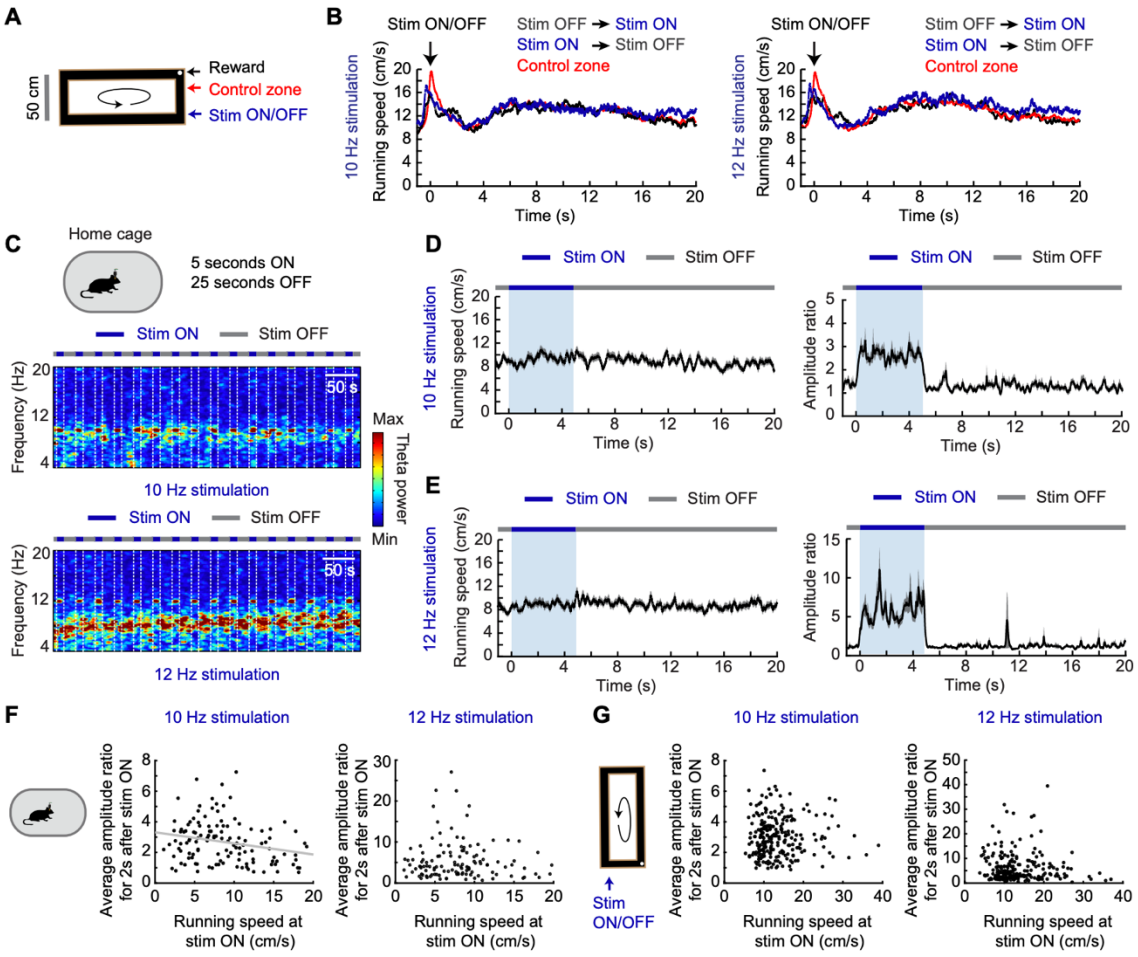
A
50 cm
Reward
Control zone
Stim ON/OFF
B
Stim ON/OFF
Stim OFF → Stim ON
Stim ON → Stim OFF
Control zone
10 Hz stimulation
12 Hz stimulation
Running speed (cm/s)
Time (s)
C
Home cage
5 seconds ON
25 seconds OFF
Stim ON
Stim OFF
Frequency (Hz)
50 s
Max
Theta power
Min
10 Hz stimulation
12 Hz stimulation
D
E
Amplitude ratio
F
G
Average amplitude ratio for 2s after stim ON
Running speed at stim ON (cm/s)
Stim ON/OFF

Figure 4S.3: Place cells reversibly reorganized in response to blue light stimulation in mice with septal oChIEF expression and in GFP controls.

(A, B) Examples of place cells that were recorded during both 10 Hz and 12 Hz stimulation sessions from oChIEF injected mice. The cells reorganized reversibly and similarly during stimulation compared to no stimulation, regardless of the stimulation frequency. Each subplot shows a lap-by-lap linearized rate map for the cell during light-on and light-off conditions with the average linearized rate map across all trials in the same condition on the bottom. The peak rate of the color scale to the right is provided on top of the plots. (C) The recording paradigm used for the 3 mice injected with a Cre-dependent virus expressing GFP was identical to the paradigm used for mice with oChIEF expression. As expected for GFP expression, the spectrogram depicts no change in the LFP frequency during light stimulation at either 10 Hz or 12 Hz. (D) CDF plots show that there was no change in the amplitude ratio between no stimulation and stimulation sessions for GFP control mice. The curves overlap so precisely that they are difficult to disambiguate. (E) Example place cells show a reversible reorganization of their spatial fields in response to 10 Hz and 12 Hz stimulation in the control mice, suggesting that place field remapping is independent of changes in theta oscillations. (F) The firing properties of place cells (rate map stability, mean firing rate, peak firing rate, number of place fields per cell, and spatial information) were affected similarly during light stimulation in GFP mice as during light stimulation in oChIEF mice (also see Fig. 3), suggesting that partial remapping was sensory-driven by the visibility of blue light during stimulation periods (Repeated measures one way ANOVA, rate map stability, 10 Hz: $n = 99$ cells, $F(1.868, 183.1) = 64.49$, $p < 0.0001$; 12 Hz: $n = 90$ cells, $F(1.992, 173.3) = 57.2$, $p < 0.0001$; Wilcoxon matched pairs signed rank test, 10 Hz, mean firing rate: $p = 0.147$; peak firing rate: $p = 0.825$; number of fields: $p = 0.0002$; spatial information: $p = 0.013$; 12 Hz: mean firing rate: $p = 0.369$; peak firing rate: $p = 0.258$; number of fields: $p = 0.0002$; spatial information: $p = 0.725$). Histograms depict mean ± SEM. Significantly different groups are assigned separate letters (a, b, and c). *$p < 0.05$, ***$p < 0.001$. (G, H) Linearized firing rate maps for all cells that were recorded during no-stimulation and stimulation laps from the oChIEF injected mice. While cells were reordered separately for the no-stimulation and stimulation condition in **Figure 4.3F**, the cells are ordered here by their position on the track in the no-stimulation laps, and the same order was maintained for the stimulation laps.

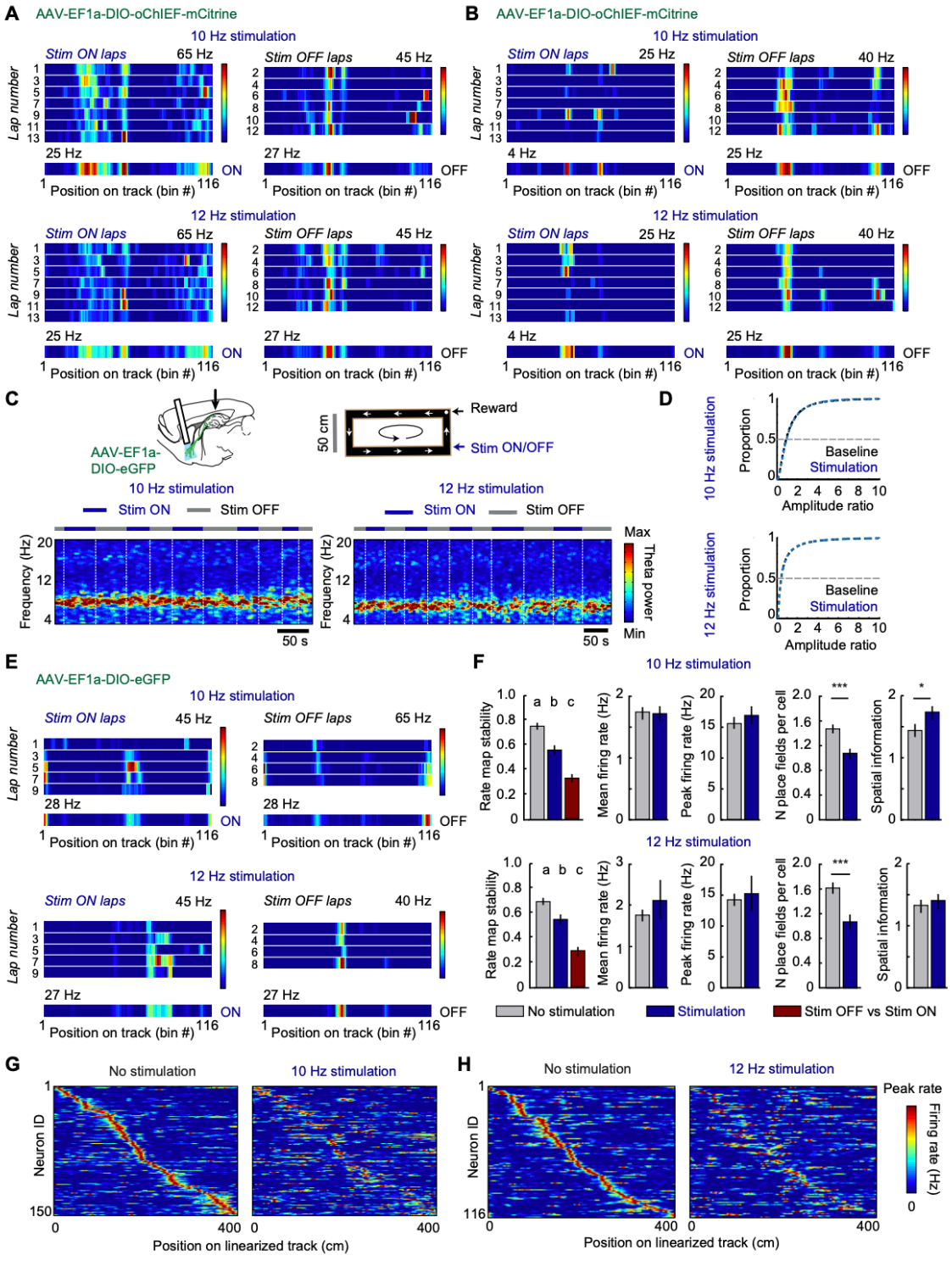
A
AAV-EF1a-DIO-oChIEF-mCitrine
10 Hz stimulation
Stim ON laps
65 Hz
Stim OFF laps
45 Hz
Lap number
25 Hz
ON
27 Hz
OFF
Position on track (bin #)
12 Hz stimulation
B
AAV-EF1a-DIO-oChIEF-mCitrine
25 Hz
40 Hz
4 Hz
C
AAV-EF1a-DIO-eGFP
50 cm
Reward
Stim ON/OFF
Stim ON
Stim OFF
Frequency (Hz)
Max
Theta power
Min
50 s
D
10 Hz stimulation
12 Hz stimulation
Proportion
Baseline
Stimulation
Amplitude ratio
E
AAV-EF1a-DIO-eGFP
28 Hz
F
Rate map stability
Mean firing rate (Hz)
Peak firing rate (Hz)
N place fields per cell
Spatial information
No stimulation
Stimulation
Stim OFF vs Stim ON
G
No stimulation
10 Hz stimulation
Neuron ID
Position on linearized track (cm)
H
12 Hz stimulation
Peak rate
Firing rate (Hz)

Figure 4S.4: Theta phase and theta frequency spiking properties of CA1 principal cells and interneurons during optogenetic pacing of MSA PV neurons.

(A) The mean phase and mean resultant length of spiking at theta frequencies did not differ between no-stimulation and 10 Hz-stimulation laps. During 12 Hz-stimulation laps, there was a minor increase in the mean resultant length, while the mean phase was not different. *$p < 0.05$. (B) Histograms depicting the distribution of peak frequencies (in the 6-14 Hz range) of CA1 principal cell spiking during no-stimulation versus stimulation laps. Without stimulation, there was an over-representation of frequencies above the endogenous theta frequency. During stimulation, the most common frequency was above the stimulation frequency. Note that low theta rhythmicity often results in the detection of a peak at the lower boundary of our detection range (i.e., 6-7 Hz). (C) Probability distribution of the difference between the peak frequency of CA1 pyramidal cell spiking (measured from the autocorrelogram of each cell) and the peak LFP frequency. Control (red) is the cellular oscillation frequency during no stimulation minus 10 Hz (top) or 12 Hz (bottom). (D) Same as B, but for CA1 interneuron spiking. Most interneurons accelerated their frequency compared to the stimulation frequency. (E) Same as C, but for CA1 interneurons. Most cells fired ~0.5-1 Hz faster than the ongoing LFP frequency during stimulation trials. Also see Fig. 4E. (F) Schematic of projections from the MSA to the hippocampal CA1 area. While cholinergic projections from the MSA terminate in the vicinity of the pyramidal cell layer, GABAergic septal neurons are known to project broadly throughout stratum oriens (s.o.), stratum pyramidale (s.p.), and stratum radiatum (s.r.) and are known to terminate on various interneuron subtypes, including those that preferentially target dendritic regions (Freund and Antal, 1988; Frotscher and Léránth, 1985; Joshi et al., 2017; Unal et al., 2015). Septal control over rhythmic synaptic activity in the dendritic regions while the oscillation frequency of CA1 cells is controlled by feedback circuits between principal cells could explain the direct control of the LFP frequency by septal stimulation while the cellular oscillation frequency is simultaneously accelerated. MSA, medial septal area; EC, entorhinal cortex; IN, interneuron; BC, basket cell; ACh, Acetylcholine; PV, Parvalbumin; s.o., stratum oriens; s.p., stratum pyramidale; s.r., stratum radiatum; s.l.m., stratum lacunosum-moleculare.

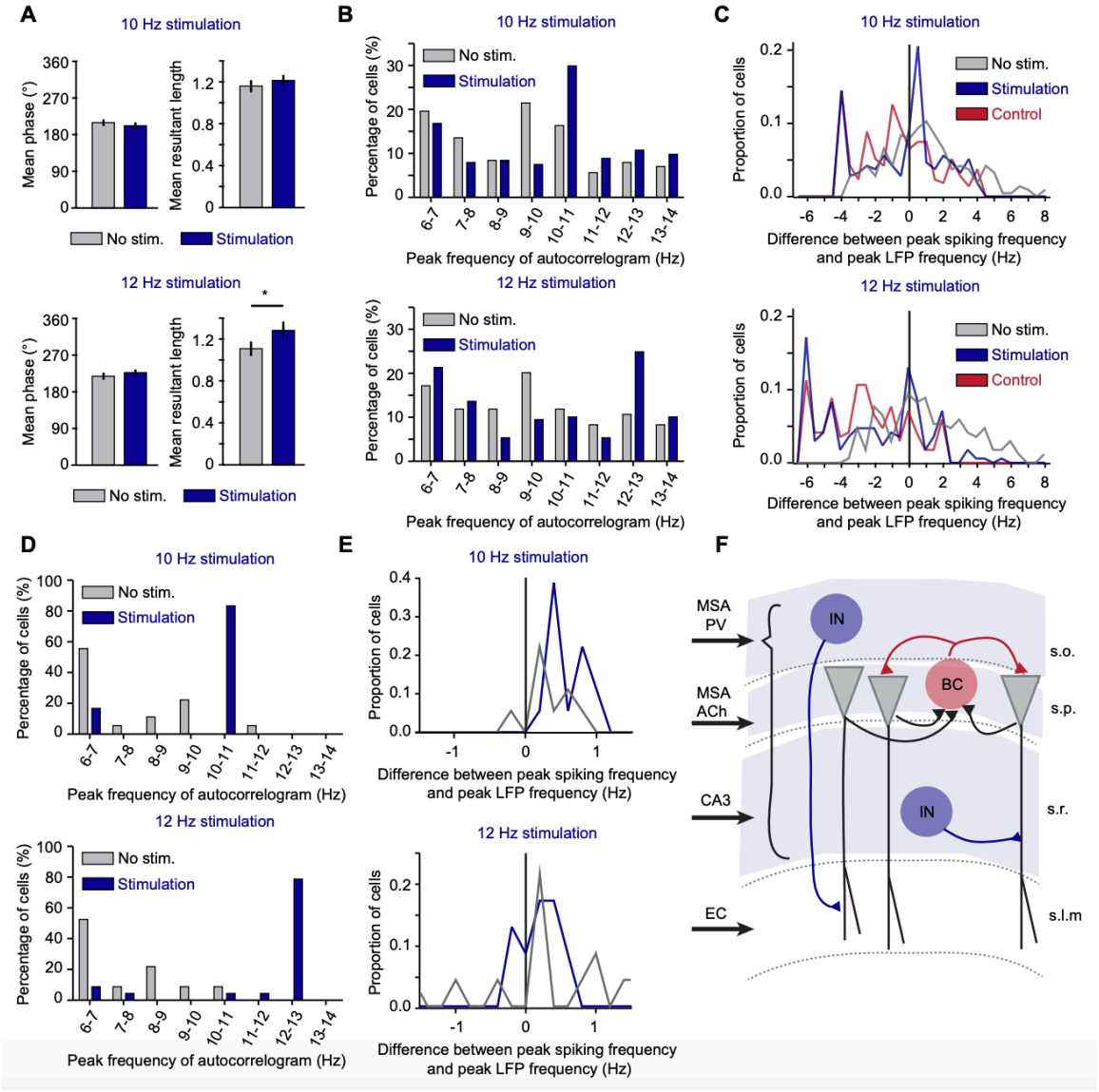
A
10 Hz stimulation
Mean phase (°)
Mean resultant length
No stim.
Stimulation
12 Hz stimulation
*
B
10 Hz stimulation
Percentage of cells (%)
Peak frequency of autocorrelogram (Hz)
12 Hz stimulation
C
10 Hz stimulation
Proportion of cells
Control
Difference between peak spiking frequency and peak LFP frequency (Hz)
12 Hz stimulation
D
10 Hz stimulation
12 Hz stimulation
E
10 Hz stimulation
12 Hz stimulation
F
MSA PV
MSA ACh
CA3
EC
IN
BC
s.o.
s.p.
s.r.
s.l.m

V.

Theta Sequences of Grid Cell Populations Can Provide a Movement-Direction Signal

"The mind is not a book, to be opened at will and examined at leisure. Thoughts are not etched on the inside of skulls, to be perused by an invader. The mind is a complex and many-layered thing."

— J.K. Rowling, Harry Potter and the Order of the Phoenix

Abstract

It has been proposed that path integration in mammals is performed by the convergence of internally generated speed and directional inputs onto grid cells. Although this hypothesis has been supported by the discovery that head direction, speed, and grid cells are intermixed within entorhinal cortex and by the recent finding that head-direction inputs are necessary for grid firing, many details on how grid cells are generated have remained elusive. For example, analysis of recording data suggests that substituting head direction for movement direction accrues errors that preclude the formation of grid patterns. To address this discrepancy, we propose that the organization of grid networks makes it plausible that movement-direction signals are an output from grid cells and that temporally precise grid cell sequences provide a robust directional signal to other spatial and directional cell types.

Introduction

Grid cells in the medial entorhinal cortex (mEC) were discovered by examining the firing patterns of entorhinal cell populations that project to hippocampal place cells (Fyhn et al., 2004; Hafting et al., 2005). As a consequence, the initial focus of computational models was on the spatial

information that entorhinal grid cells could provide to hippocampal place cells or, more generally, to a map-like representation of the environment (McNaughton et al., 2006a; Solstad et al., 2006). However, the tessellating nature of grid cells also suggested that they may not only be the source of spatial information for a map-based navigation system, but that they might themselves be at the core of a specialized path integration-based navigation system, which is particularly well suited to code for locations and distances in the absence of prominent landmarks (Burgess et al., 2007; Hafting et al., 2005; McNaughton et al., 2006a).

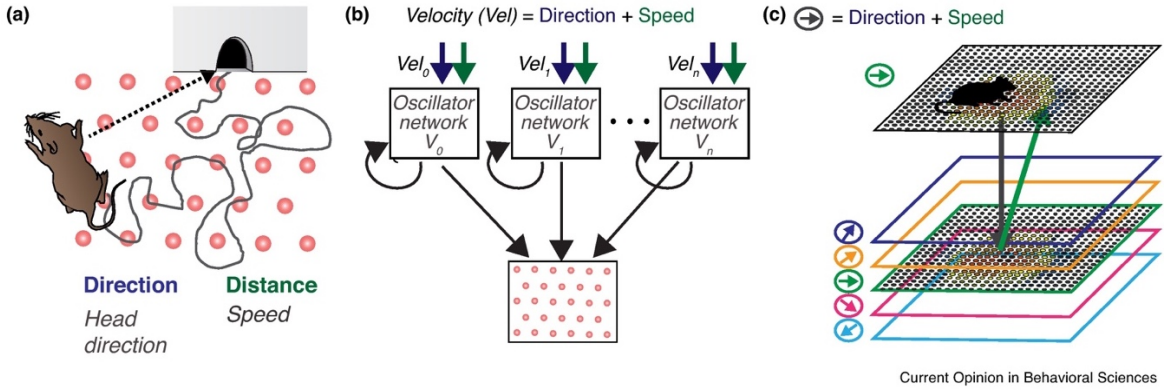

Figure 5.1: Multiple mechanisms for the implementation of path integration.

(a) Path integration mechanisms for mammalian species such as rodents, who forage under conditions with sparse visual and landmark cues, have been proposed to predominantly rely on internally generated estimates of speed and direction. The internal direction and distance estimates are integrated by grid cells, which could provide a path-integration based estimate of the current position. Here, direction signals are assumed to be provided by internally generated head direction cells, and distance is computed using internally generated speed signals that also manifest within the brain. (b) One major class of grid cell generation models are the oscillatory interference models (Burgess et al., 2007; Zilli and Hasselmo, 2010). In this class of models, signals are integrated by velocity-controlled oscillators that receive head direction and speed inputs. Grid cells receive information from multiple oscillators that each respond to a different direction. Coincident peak phases of activity result in grid cell firing, whereas cells remain silent when the oscillators are out of phase with each other. Adapted from (Zilli and Hasselmo, 2010). (c) The other major class of grid cell generation models are continuous attractor network models, which generate grid patterns from local recurrent network connectivity. Depicted here is one such implementation (McNaughton et al., 2006a). Excitatory and inhibitory connections between cells lead to a 'bump' of focused activity in the network, which is gradually moved in the cell sheet by directional and speed signals. Adapted from (McNaughton et al., 2006a).

Updating of current location by direction and speed signals

Path integration (or dead reckoning) requires that direction and speed (or distance) signals are integrated to update the current position in relation to a reference position (Wolf, 2011). Computational models of grid cells therefore began to examine neuronal mechanisms that are capable of generating grid patterns from the convergence of speed and direction inputs (**Figure 5.1**). The integration of these two types of afferent signals was initially proposed to be performed within single grid cells (Burgess et al., 2007), but implementation of these computations in neuronal networks was also considered for a number of reasons. First, the reliance of brain systems on internally integrated movement signals is limited by error accumulation, which can be effectively reduced by combining individual noisy signals into a larger network (Zilli and Hasselmo, 2010). Second, experimental work identified that head-direction cells, conjunctive grid by direction cells, and speed cells provide local inputs to grid cell networks (Kropff et al., 2015; Sargolini et al., 2006), which is consistent with a number of feedforward and/or recurrent neural network architectures that combine inputs of these cell types with local network computations (Giocomo et al., 2011b; Zilli, 2012). For example, based on the finding that head direction cells and conjunctive direction by grid cells are preferentially found in deep layers and that grid cells without directional preference are found in layer II (Sargolini et al., 2006), many models explicitly include connectivity between different cell types within mEC to perform network computations (Tocker et al., 2015).

Because the implementation of neuronal computations that give rise to grid cells has been extensively considered and reviewed (Giocomo et al., 2011b; Zilli, 2012), we will focus on recent progress in identifying potential sources for directional and speed signals to grid cells as well as on recent work that has challenged the assumption that head-direction signals can be used interchangeably with movement-direction information in grid cell models (Raudies et al., 2015). Furthermore, based on work that has not identified any substantive movement-direction signals in mEC (Raudies et al., 2015), we consider the possibility that movement direction coding is only

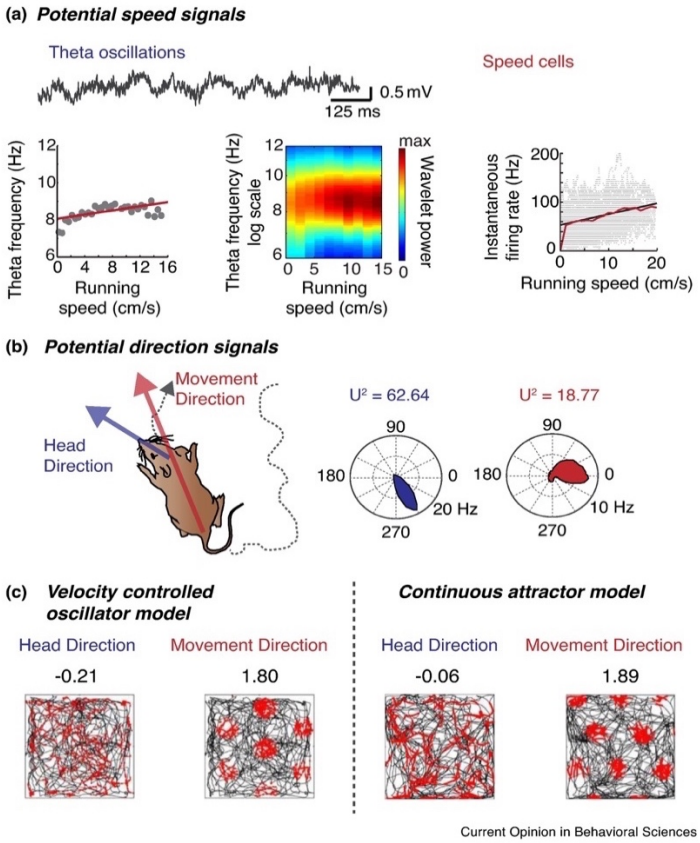

Figure 5.2: Sources of speed and direction information for path integration in rodents.

(a) Speed information is internally represented in rodents by at least three possible mechanisms. *Left*, the frequency of theta oscillations is modulated by the running speed of an animal. *Middle*, in addition to changes in theta frequency, the amplitude or power of theta oscillations is also positively correlated with increasing running speed, as depicted in the spectrogram where power is shown on a scale from blue to red. *Right*, speed cells have been found in mEC (Kropff et al., 2015). As shown in the example, most speed cells increase their firing rate with increased running speed. (b) Movement direction is assumed to resemble head direction signals, which are found in several brain areas, including mEC. However, the schematic on the left depicts how for every instant during foraging, head direction can be distinct from the direction of movement. As a result of this incongruity, a single cell that is strongly tuned to the head direction of an animal (blue) provides a conflicting and more broadly tuned signal for movement direction (red). Watson U^2 measures are provided above each polar plot. Note that the strength of movement tuning in the example is exceptionally high compared to other mEC cells. Adapted from (Raudies et al., 2015). (c) Using pure head direction signals, instead of movement direction signals in grid cell models results in the rapid breakdown of grid cells due to the disparity between the two signals. Shown here are two examples of grid cells that were reconstructed with either a velocity-controlled oscillator model or a continuous attractor network implementation (see **Figure 5.1**). Gridness scores for each example are provided on top of each plot. Neither model supports grid cell generation when a head direction signal is provided, which suggests that head direction cannot substitute for movement direction in path integration computations. Adapted from (Raudies et al., 2015).

weakly provided as an input to grid cells and emerges as a robust temporal code from grid cell network activity. This mechanism implies that directional information is also an output from grid cells while many standard grid cell models only consider it as an input (Finkelstein et al., 2016).

Head-direction signals are not sufficient as ongoing inputs to grid networks

Each grid cell generates neuronal activity at multiple, regularly arranged spatial locations (Hafting et al., 2005). When these spatial firing patterns are updated over seconds and minutes by path integration, the internally generated running speed and direction signal both need to be highly accurate. For the speed signal, three possible sources have been identified as highly correlated with running speed and could therefore each provide a reliable speed input (Hinman et al., 2016; Jeewajee et al., 2008; Kemere et al., 2013; Kropff et al., 2015) (**Figure 5.2**). As a directional signal for grid cells, sharply tuned head-direction cells, which arise from the processing of signals from vestibular nuclei, have been considered as a reliable source (Taube, 2007). Even though head direction is known to be reliably represented in the brain, there is limited knowledge on the modulation of the head-direction code by additional internal directional movements, such as eye movements or rotation of the head with respect to the body axis. For example, deviation of the head angle from the body axis could be derived from the disparity in optic flow that arises as a consequence of the mismatch between head and movement direction (Raudies et al., 2015) or, more directly, from proprioceptors in neck muscles. Based on studies that detected a movement direction signal in the medial septal area (King et al., 1998; Welday et al., 2011), it is possible that integration occurs in subcortical areas, but again, these studies have not explored to what extent head direction and movement direction are coded jointly or separately.

Because of the uncertainty in where and how a movement-direction signal is coded in the brain, many computational models have used the head-direction signal interchangeably with a movement-direction signal, based on the assumption that the head direction is a good

approximation for movement direction. However, it has recently been found in analytical work that grid patterns can only emerge when using the recorded movement direction of the animal as an input to computational networks, but not when substituting the recorded head direction of the animal (Raudies et al., 2015). Alternatively, computational models have proposed that directional information is received from stripe cells (Burgess et al., 2007; Grossberg and Pilly, 2012). However, the proportion of stripe cells is low (Krupic et al., 2012) and their existence is controversial because they could be obtained from the incomplete separation of the spike patterns of two grid cells (Navratilova et al., 2016).

The broad use of a head-direction signal in models for grid generation is also motivated by the presence of head direction cells and of conjunctive head-direction by grid cells in mEC, which has been taken as evidence that head-direction signals are integrated into the local neuronal codes (Sargolini et al., 2006). Furthermore, recent experimental evidence has shown that the grid network depends on input from the brain's head-direction system (Winter et al., 2015). Although these findings can be interpreted as supporting the notion that head-direction input is critical for grid generation, these data need to be reconciled with the finding that head-direction coding is not sufficient for maintaining grid patterns (Raudies et al., 2015). Several possibilities are mentioned here which are not mutually exclusive. First, movement and head-direction may be jointly coded and may thus not have been independently manipulated (Winter et al., 2015). Second, manipulations of thalamic head-direction may have resulted in minor effects on theta oscillations. Theta oscillations are, in turn, known to contribute to speed as well as to directional coding (Hinman et al., 2016; King et al., 1998; Welday et al., 2011), such that speed and head-direction coding may again not have been independently manipulated. Third, manipulations of thalamic nuclei resulted in reduced firing rates of entorhinal cells, which in turn, is expected to result in diminished grid patterns in many computational models that rely on afferent and recurrent connectivity (Giocomo et al., 2011b; Zilli, 2012). Although the diminished grid coding after inactivation of the head-

direction system therefore strongly implies head-direction coding in grid generation, the finding of a strong disparity between the movement and head direction code (Raudies et al., 2015). raises the possibility that the head-direction code would need to be complemented by other directional signals or additional sensory pathways to correct for the moment-by-moment errors that arise from exclusively relying on head-direction inputs.

Where and how could a movement-direction signal be generated?

The finding that a movement-direction signal is required for grid cell generation by path integration, along with limited evidence for movement-direction coding by entorhinal cells (Raudies et al., 2015). raises the question about the nature and origin of the movement-direction signal (or a signal that corrects the disparity between head-direction and movement-direction) in mEC. Although a movement-direction signal could emerge from directionally tuned coupling of oscillations in the medial septal area (King et al., 1998; Welday et al., 2011) or from not-yet-identified sensory processing of proprioceptive and/or optic flow information, we propose that an alternative hypothesis should also be considered. A robust movement-direction signal could be obtained from the readout of temporal sequences of grid cell activation (**Figure 5.3**). In particular, the modular arrangement of grid cells results in a limited number of grid cell sequences that are associated with each movement direction such that a finite set of grid sequences can be combined to represent a particular direction **(Figure 5.3)**. Because the highly modular organization of mEC grid cell populations is a prerequisite of the proposed mechanism, we will give a brief overview of the modular grid cell organization and then describe in more detail how the regularity within each module supports the readout of movement-direction information.

Modular organization of the grid network

Grid cells have been estimated to be organized into less than ten modules per hemisphere (Stensola et al., 2012). The modules are topographically organized with partial anatomical overlap between two adjacent modules. Each module consists of grid cells with similar field size, grid spacing and grid orientation. Modules with smaller grid spacing and grid field size are more dorsal within mEC, while those with larger grid spacing and grid field size are generally more ventral. The only parameter that varies between grid cells within a module is the spatial firing phase, such that all firing peaks between pairs of grid cells are offset by a fixed distance (**Figure 5.3**). The common grid spacing and orientation as well as the phase offset between different grid cells in a module are not only preserved within an environment, but also across environments. In correspondence with these experimental findings, the organization of grid cells into populations with equal spacing is a foundational feature of many computational network models for grid cell generation (Burak and Fiete, 2009; Fuhs and Touretzky, 2006). For models in which grid patterns initially emerge separately in individual cells, common orientation can be added through connectivity between grid cells (Zilli, 2012).

While the organization of grids into modules with equal spacing and orientation makes the organization of grid cells extremely intriguing (Hafting et al., 2005; Stensola et al., 2012), the regularity has also been found to somewhat hamper the readout of location information from populations of grid cells. If only reading information from a single grid module, the equal spacing and orientation implies that the population code of grid cells in the module repeats at the scale of the grid spacing within the module (**Figure 5.3**). The ambiguity about spatial location can be resolved by reading from multiple grid modules (Solstad et al., 2006; Stemmler et al., 2015), by using the recently discovered rate code within grid cells (Diehl et al., 2017), or by using the spatial and rate code of the large spatial non-grid population in mEC (Diehl et al., 2017; Kanter et al., 2017). In contrast, if grid cells within a module are used to read out a movement-direction code,

Figure 5.3. A finite number of grid cell sequences is associated with each movement direction.

(a) In a lattice of grid field peaks, grid peaks that belong to the same grid cell are shown with a consistent symbol (e.g., red solid circle; the stippled lines between grid peaks of this cell illustrate the grid spacing within the module). By showing only grid field peaks, the consistent spacing and orientation of multiple grid cells within a module as well as the fixed offsets between peaks of different cells are apparent. For the illustration, the offsets between the depicted grid peaks have generally been chosen to occur at regular distances, but note that offsets between fields can be at any distance in experimental data (Hafting et al., 2005; Stensola et al., 2012) (e.g., as shown for the grid cell depicted by the filled black circle). Red arrows, within the lattice of peaks, the same movement direction repeatedly corresponds to the same sequence of cells (e.g., open red then blue then green circles). Grey arrow, if a movement direction were represented by few grid cells, there could be ambiguity for directions that are offset by 120 degrees. However, the inclusion of additional cells in the sequence code (e.g., the one depicted by black filled circles) resolves the ambiguity. Purple and blue arrows, the same cells fire for sequences in opposite directions, but the order of the cell activity is reversed. Black and red arrows, multiple sequences code for the same movement direction. However, there is only a limited set of sequences for each direction because of the repetitive nature of the grid lattice. (b) Each number depicts the peak of a hippocampal place field within a 2-D environment. Note that the lack of regularly repeated firing fields results in a different sequence for each combination of movement direction and starting point. Coding with non-repetitive representation is therefore better suited for representing specific trajectories rather than movement direction. (c) Phase precession results in the time-compression of sequences (Dragoi and Buzsáki, 2006), and the sequence of phase processing grid cells within a theta cycle can be used for the readout of the current movement direction. As shown in the example, sequences have different start and end points depending on the position of the animal along the trajectory, but identical sequences will eventually repeat for trajectories with corresponding movement directions. (d) Schematic in which inputs to the entorhinal cortex give rise to speed, head-direction, and spatially selective cells, but only to limited modulation of cells by movement-direction (grey text implies that this information is initially more weakly represented). All types of information are locally processed, and sequential coding of movement direction emerges as an output from grid cells that could be read out by other spatially and directionally selective cells within entorhinal cortex and hippocampus. EC, entorhinal cortex. Hpc, hippocampus.

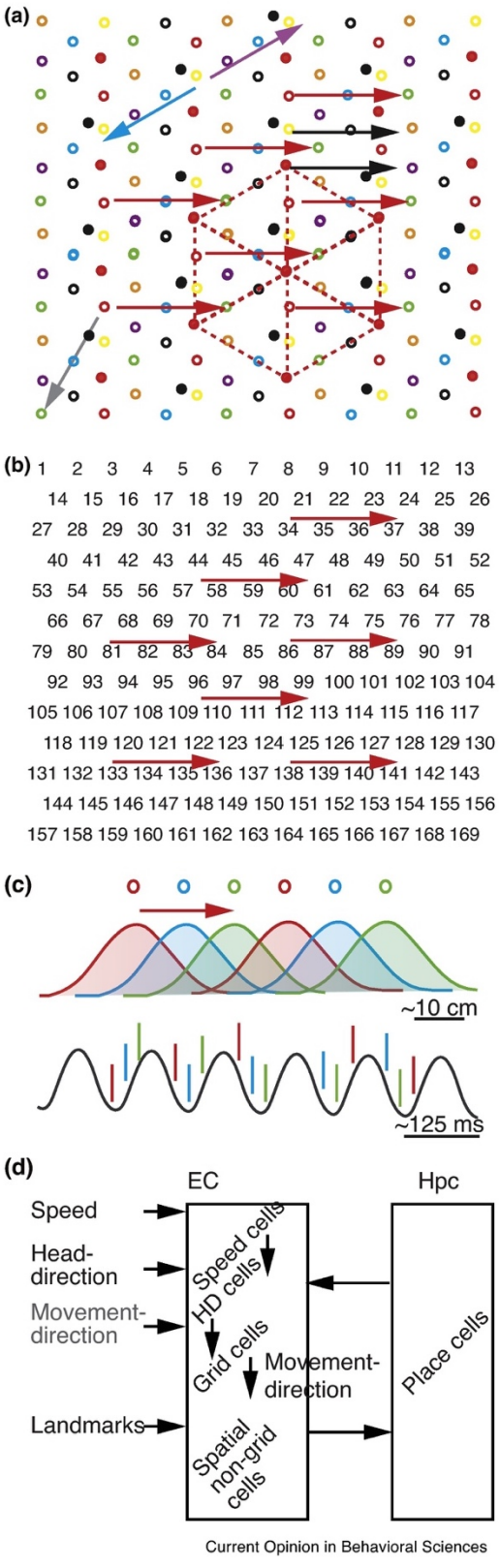
(a)
(b)
1 2 3 4 5 6 7 8 9 10 11 12 13
14 15 16 17 18 19 20 21 22 23 24 25 26
27 28 29 30 31 32 33 34 35 36 37 38 39
40 41 42 43 44 45 46 47 48 49 50 51 52
53 54 55 56 57 58 59 60 61 62 63 64 65
66 67 68 69 70 71 72 73 74 75 76 77 78
79 80 81 82 83 84 85 86 87 88 89 90 91
92 93 94 95 96 97 98 99 100 101 102 103 104
105 106 107 108 109 110 111 112 113 114 115 116 117
118 119 120 121 122 123 124 125 126 127 128 129 130
131 132 133 134 135 136 137 138 139 140 141 142 143
144 145 146 147 148 149 150 151 152 153 154 155 156
157 158 159 160 161 162 163 164 165 166 167 168 169
(c)
~10 cm
~125 ms
(d)
EC
Hpc
Speed
Head-direction
Movement-direction
Landmarks
Speed cells
HD cells
Grid cells
Movement-direction
Spatial non-grid cells
Place cells
Current Opinion in Behavioral Sciences

the regularity is highly advantageous, as it results in a limited number of sequences that are associated with each movement direction (**Figure 5.3a**).

The regularity of the grid cell organization within each module results in a finite set of sequences that correspond to each movement direction

While the fixed grid size and orientation within a module results in ambiguity in the readout of position, the fixed arrangement is advantageous for the readout of movement direction. The repetitive nature of a grid representation would greatly reduce the number of sequences that are associated with each movement direction (**Figure 5.3b**). Accordingly, the tessellation of the environment by grid fields implies that a readout mechanism would only need to learn a limited number of possibilities within each environment. Furthermore, phase differences between grid cells within a module are preserved across environments (Stensola et al., 2012), and the movement-direction code from each module would thus directly transfer to new and distinct environments. Because different modules can realign with respect to each other across environments, the only parameter that would need to be relearned for decoding movement direction across different environments is the relative rotation between pairs of modules.

A temporal code allows for the readout of movement direction within short time windows

Because of frequent changes in movement direction, a neural code for movement direction should be readable within a short time window. It is therefore relevant to note that many grid cells in rodents show theta phase precession, in particular those that are not modulated by head direction (Hafting et al., 2008). Phase precession implies that grid fields that are being entered by the animal fire at a late phase within the theta cycle while grid fields that are exited fire early within the cycle (**Figure 5.3c**). As a consequence, the grid cells with fields just behind and just ahead of the animal fire within a single theta cycle in the order that corresponds to their direction of traversal and thus

to movement direction. Within each theta cycle, there is therefore a sequence of spikes that identifies the movement progression within the grid lattice.

Using theta sequences as a mechanism for reading out movement-direction information from grid cells raises questions about animal species in which theta is either intermittent or not detectible, such as primates and bats (Jutras et al., 2013; Yartsev et al., 2011). First, sequences of grid cell firing along the movement trajectory would nonetheless exist but would need to be decoded from the spatial rather than from the temporal sequence of the grid fields that are traversed. This mechanism is adequate if travelling in a particular direction for distances that correspond to approximately the minimum grid spacing. In lieu of a mechanism that relies on an internal sense of direction, it could also be speculated that an internally generated movement direction signal may not be necessary when external landmarks (e.g., a sun compass, distal cues) are prominent and can provide a consistent directional reference, as often observed for navigation over long distances (Bingman and MacDougall-Shackleton, 2017).

How are head-direction and movement-direction signals integrated?

If grid patterns provide movement-direction information, two important questions arise. First, how are grid cells initially generated while head-direction input is more prominent than movement-direction input? Second, how are grid locations updated if head-direction input is not sufficiently precise? For the first question, we refer to the many published models on grid generation (Giocomo et al., 2011b; Zilli, 2012), including those that use head-direction inputs. Even though the head-direction input may not correspond to movement direction on a moment by moment basis, there is likely a good correspondence on average such that disparities are corrected by learning over long time periods, consistent with the emergence of grid cells within days after pups start exploring environments (Langston et al., 2010; Wills et al., 2010). However, this mechanism would only be feasible if the network learns slow enough to integrate over the

differences between the head direction and movement direction and if an animal's head position compared to its body axis is not biased over long intervals. As an alternative, a weak movement-direction signal could emerge from the medial septal area (King et al., 1998; Welday et al., 2011) or from sensory channels in which proprioceptive and/or optic flow information are processed (**Figure 5.3d**). Finally, it is also feasible that grid cells emerge by mechanisms that require only inputs from location-selective cells (Kropff and Treves, 2008). The second question — updating the location of grid firing — can also be addressed by the close association of grid cells with location-selective cells, which includes spatial non-grid cells within entorhinal cortex (Diehl et al., 2017) and inputs from hippocampal place cells (Bonnevie et al., 2013). In particular, grid cells have been shown to develop after an increasingly accurate hippocampal input has been established (Muessig et al., 2015) and have been shown to depend on hippocampal input (Bonnevie et al., 2013). In addition, it has long been known that a strong directional signal is present in hippocampal place populations which represent a path through the environment (McNaughton et al., 1996), and direction selectivity becomes even more predominant in virtual environments (Aghajan et al., 2015). However, these directional signals are highly specific for particular environments because different hippocampal cell populations are active across environments (Leutgeb et al., 2004). Furthermore, the directional signals would differ with each starting position within 2D environments (**Figure 5.3b**). These considerations make the transformation from environment-specific or behavior-specific hippocampal maps to a more generalized entorhinal map attractive, because only the more generalized map has a limited number of sequences associated with each direction. However, it remains to be tested whether and how a readout of movement direction from grid cells could be used by other cell types and brain regions that process spatial information. If spatial information from hippocampal place cells or other cells with allocentric spatial information is required to generate grid cells in the first place, the animal's current position would already have been updated in input channels to grid cells. With allocentric information already available to grid

cells, directional information from grid cells may nonetheless be useful for navigation across zones with few landmarks, for calibrating a sensory-based spatial map in each novel environment to the animal's own movement patterns, and/or for predicting which future locations are reached when travelling or planning particular movement trajectories (Rennó-Costa and Tort, 2017; Sanders et al., 2015). Moreover, grid cells could also have the function of transforming weakly tuned movement direction signals in mEC into a more robust sequence code for movement direction. Under this condition, grid cells would be the primary path integrators but other cells in the circuit would also path integrate by combining the movement direction and speed signals from entorhinal grid and speed cells.

Conclusions

Although it has been widely assumed that head-direction cells provide one of the critical inputs for path integration by grid cells, head direction information has been found to be insufficient for providing a reliable moment-by-moment estimate of movement direction (Raudies et al., 2015) such that accurate path integration is at least in some circumstances not performed by exclusively relying on head direction signals. Alternative mechanisms are therefore needed, and we evaluated the possibility that information from grid cell networks could generate a movement-direction signal. We propose that the highly modular organization of grid cell populations (Stensola et al., 2012) provides for a limited number of sequences that correspond to each movement direction irrespective of the starting point within the environment. These sequences can be read out when running in the same direction for approximately one grid cycle or, in neural systems with phase precession, on the shorter time-scale of a single theta cycle. Although this mechanism does not exclude the possibility that grid cells receive movement-direction information by not-yet-identified feedforward pathways, we propose that the direction of a movement trajectory could also be obtained from the readout of theta sequences or spatial sequences of grid cells.

Acknowledgements

This work was supported by the National Institute of Health (MH100354, NS084324, NS086947, MH100349, NS102915, NS097772), the Whitehall Foundation (20130571), Walter F. Heiligenberg Professorship to J.K.L, and an HHMI International Student Fellowship to I. Z.

Chapter 5, in full, is material as it appears in *Current Opinion in Behavioral Sciences*, 2018, Zutshi, Ipshita, Leutgeb, Jill K., Leutgeb, Stefan. The dissertation author was the primary researcher and author of this paper.

REFERENCES

Aghajan, Z.M., Acharya, L., Moore, J.J., Cushman, J.D., Vuong, C., and Mehta, M.R. (2015). Impaired spatial selectivity and intact phase precession in two-dimensional virtual reality. Nat. Neurosci.

Alonso, A., and Klink, R. (1993). Differential electroresponsiveness of stellate and pyramidal-like cells of medial entorhinal cortex layer II. J. Neurophysiol. *70*, 128–143.

Alonso, A., and Llinás, R.R. (1989). Subthreshold Na+-dependent theta-like rhythmicity in stellate cells of entorhinal cortex layer II. Nature.

Amaral, D.G., and Witter, M.P. (1989). The three-dimensional organization of the hippocampal formation: A review of anatomical data. Neuroscience *31*, 571–591.

Anderson, M.I., and Jeffery, K.J. (2003). Heterogeneous modulation of place cell firing by changes in context. J. Neurosci.

Anikeeva, P., Andalman, A.S., Witten, I., Warden, M., Goshen, I., Grosenick, L., Gunaydin, L.A., Frank, L.M., and Deisseroth, K. (2012). Optetrode: a multichannel readout for optogenetic control in freely moving mice. Nat. Neurosci. *15*, 163–170.

Aronov, D., Nevers, R., and Tank, D.W. (2017). Mapping of a non-spatial dimension by the hippocampal-entorhinal circuit. Nature.

Atallah, B. V., and Scanziani, M. (2009). Instantaneous Modulation of Gamma Oscillation Frequency by Balancing Excitation with Inhibition. Neuron.

Barry, C., Hayman, R., Burgess, N., and Jeffery, K.J. (2007). Experience-dependent rescaling of entorhinal grids. Nat. Neurosci.

Beason-Held, L.L., Rosene, D.L., Killiany, R.J., and Moss, M.B. (1999). Hippocampal formation lesions produce memory impairment in the rhesus monkey. Hippocampus.

Beed, P., Bendels, M.H.K., Wiegand, H.F., Leibold, C., Johenning, F.W., and Schmitz, D. (2010). Analysis of Excitatory Microcircuitry in the Medial Entorhinal Cortex Reveals Cell-Type-Specific Differences. Neuron *68*, 1059–1066.

Beed, P., Gundlfinger, A., Schneiderbauer, S., Song, J., Böhm, C., Burgalossi, A., Brecht, M., Vida, I., and Schmitz, D. (2013). Inhibitory gradient along the dorsoventral axis in the medial entorhinal cortex. Neuron *79*, 1197–1207.

Belluscio, M.A., Mizuseki, K., Schmidt, R., Kempter, R., and Buzsáki, G. (2012). Cross-frequency phase-phase coupling between θ and γ oscillations in the hippocampus. J. Neurosci.

Bender, F., Gorbati, M., Cadavieco, M.C., Denisova, N., Gao, X., Holman, C., Korotkova, T., and Ponomarenko, A. (2015). Theta oscillations regulate the speed of locomotion via a hippocampus to lateral septum pathway. Nat. Commun.

Bennett, M.R., Gibson, W.G., and Robinson, J. (1994). Dynamics of the CA3 Pyramidal Neuron

Autoassociative Memory Network in the Hippocampus. Philos. Trans. R. Soc. B Biol. Sci. *343*, 167–187.

Beyeler, A., Namburi, P., Glober, G.F., Simonnet, C., Calhoon, G.G., Conyers, G.F., Luck, R., Wildes, C.P., and Tye, K.M. (2016). Divergent Routing of Positive and Negative Information from the Amygdala during Memory Retrieval. Neuron *90*, 348–361.

Bingman, V.P., and MacDougall-Shackleton, S.A. (2017). The avian hippocampus and the hypothetical maps used by navigating migratory birds (with some reflection on compasses and migratory restlessness). J. Comp. Physiol. A Neuroethol. Sensory, Neural, Behav. Physiol.

Blumberg, B.J., Flynn, S.P., Barriere, S.J., Mouchati, P.R., Scott, R.C., Holmes, G.L., and Barry, J.M. (2016). Efficacy of nonselective optogenetic control of the medial septum over hippocampal oscillations: The influence of speed and implications for cognitive enhancement. Physiol. Rep.

Boccara, C.N., Sargolini, F., Thoresen, V.H., Solstad, T., Witter, M.P., Moser, E.I., and Moser, M.B. (2010). Grid cells in pre-and parasubiculum. Nat. Neurosci.

Bonnevie, T., Dunn, B., Fyhn, M., Hafting, T., Derdikman, D., Kubie, J.L., Roudi, Y., Moser, E.I., and Moser, M.-B.B. (2013). Grid cells require excitatory drive from the hippocampus. Nat. Neurosci. *16*, 309–317.

Borhegyi, Z. (2004). Phase Segregation of Medial Septal GABAergic Neurons during Hippocampal Theta Activity. J. Neurosci.

Bostock, E., Muller, R.U., and Kubie, J.L. (1991). Experience-dependent modifications of hippocampal place cell firing. Hippocampus.

Bragin, A., Jando, G., Nadasdy, Z., Hetke, J., Wise, K., and Buzsaki, G. (1995). Gamma (40-100 Hz) oscillation in the hippocampus of the behaving rat. J. Neurosci.

Brandon, M.P., Bogaard, A.R., Libby, C.P., Connerney, M.A., Gupta, K., and Hasselmo, M.E. (2011). Reduction of theta rhythm dissociates grid cell spatial periodicity from directional tuning. Science (80-.). *332*, 595–599.

Brandon, M.P., Koenig, J., Leutgeb, J.K., and Leutgeb, S. (2014). New and Distinct Hippocampal Place Codes Are Generated in a New Environment during Septal Inactivation. Neuron *82*, 789–796.

Brun, V.H., Solstad, T., Kjelstrup, K.B., Fyhn, M., Witter, M.P., Moser, E.I., and Moser, M.-B.B. (2008). Progressive increase in grid scale from dorsal to ventral medial entorhinal cortex. Hippocampus *18*, 1200–1212.

Buetfering, C., Allen, K., and Monyer, H. (2014). Parvalbumin interneurons provide grid cell-driven recurrent inhibition in the medial entorhinal cortex. Nat. Neurosci. *17*, 710–718.

Burak, Y., and Fiete, I.R. (2009). Accurate path integration in continuous attractor network models of grid cells. PLoS Comput. Biol. *5*, e1000291.

Burgess, N., Barry, C., and O'Keefe, J. (2007). An oscillatory interference model of grid cell firing.

Hippocampus *17*, 801–812.

Buzsáki, G. (2002). Theta oscillations in the hippocampus (Cell Press).

Buzsáki, G. (2015). Hippocampal sharp wave-ripple: A cognitive biomarker for episodic memory and planning. Hippocampus *25*, 1073–1188.

Buzsáki, G., and Draguhn, A. (2004). Neuronal oscillations in cortical networks. Science (80-.).

Callaway, E.M., and Luo, L. (2015). Monosynaptic Circuit Tracing with Glycoprotein-Deleted Rabies Viruses. J. Neurosci.

Canto, C.B., and Witter, M.P. (2012). Cellular properties of principal neurons in the rat entorhinal cortex. II. The medial entorhinal cortex. Hippocampus *22*, 1277–1299.

Carpenter, F., Manson, D., Jeffery, K., Burgess, N., and Barry, C. (2015). Grid cells form a global representation of connected environments. Curr. Biol.

Chen, G., Manson, D., Cacucci, F., and Wills, T.J. (2016). Absence of Visual Input Results in the Disruption of Grid Cell Firing in the Mouse. Curr. Biol. *26*, 2335–2342.

Couey, J.J., Witoelar, A., Zhang, S.-J., Zheng, K., Ye, J., Dunn, B., Czajkowski, R., Moser, M.-B., Moser, E.I., Roudi, Y., et al. (2013). Recurrent inhibitory circuitry as a mechanism for grid formation. Nat. Neurosci. *16*, 318–324.

Dannenberg, H., Pabst, M., Braganza, O., Schoch, S., Niediek, J., Bayraktar, M., Mormann, F., and Beck, H. (2015). Synergy of Direct and Indirect Cholinergic Septo-Hippocampal Pathways Coordinates Firing in Hippocampal Networks. J. Neurosci.

Debernardi, A., Sala, E., D'Aliberti, G., Talamonti, G., Franchini, A.F., and Collice, M. (2010). Alcmaeon of croton (Oxford University Press).

Dhillon, A., and Jones, R.S.. (2000). Laminar differences in recurrent excitatory transmission in the rat entorhinal cortex in vitro. Neuroscience *99*, 413–422.

Dickson, C.T., Mena, A.R., and Alonso, A. (1997). Electroresponsiveness of medial entorhinal cortex layer III neurons in vitro. Neuroscience.

Diehl, G.W., Hon, O.J., Leutgeb, S., and Leutgeb, J.K. (2017). Grid and Nongrid Cells in Medial Entorhinal Cortex Represent Spatial Location and Environmental Features with Complementary Coding Schemes. Neuron *94*, 1–10.

Domnisoru, C., Kinkhabwala, A.A., and Tank, D.W. (2013). Membrane potential dynamics of grid cells. Nature *495*, 199–204.

Dragoi, G., and Buzsáki, G. (2006). Temporal Encoding of Place Sequences by Hippocampal Cell Assemblies. Neuron.

Ego-Stengel, V., and Wilson, M.A. (2010). Disruption of ripple-associated hippocampal activity during rest impairs spatial learning in the rat. Hippocampus *20*, 1–10.

Einevoll, G.T., Kayser, C., Logothetis, N.K., and Panzeri, S. (2013). Modelling and analysis of local field potentials for studying the function of cortical circuits. Nat. Rev. Neurosci.

Finkelstein, A., Las, L., and Ulanovsky, N. (2016). 3-D Maps and Compasses in the Brain. Annu. Rev. Neurosci.

Freund, T.F., and Antal, M. (1988). GABA-containing neurons in the septum control inhibitory interneurons in the hippocampus. Nature *336*, 170–173.

Frotscher, M., and Léránth, C. (1985). Cholinergic innervation of the rat hippocampus as revealed by choline acetyltransferase immunocytochemistry: A combined light and electron microscopic study. J. Comp. Neurol.

Fuchs, E.C., Neitz, A., Pinna, R., Melzer, S., Caputi, A., and Monyer, H. (2016). Local and Distant Input Controlling Excitation in Layer II of the Medial Entorhinal Cortex. Neuron *89*, 194–208.

Fuhrmann, F., Justus, D., Sosulina, L., Kaneko, H., Beutel, T., Friedrichs, D., Schoch, S., Schwarz, M.K., Fuhrmann, M., and Remy, S. (2015). Locomotion, Theta Oscillations, and the Speed-Correlated Firing of Hippocampal Neurons Are Controlled by a Medial Septal Glutamatergic Circuit. Neuron *86*, 1253–1264.

Fuhs, M.C., and Touretzky, D.S. (2006). A Spin Glass Model of Path Integration in Rat Medial Entorhinal Cortex. J. Neurosci. *26*, 4266–4276.

Fujimaru, Y., and Kosaka, T. (1996). The distribution of two calcium binding proteins, calbindin D-28K and parvalbumin, in the entorhinal cortex of the adult mouse. Neurosci. Res.

Fyhn, M., Molden, S., Witter, M.P., Moser, E.I., and Moser, M.B. (2004). Spatial representation in the entorhinal cortex. Science (80-.).

Fyhn, M., Hafting, T., Treves, A., Moser, M.-B.B., and Moser, E.I. (2007). Hippocampal remapping and grid realignment in entorhinal cortex. Nature *446*, 190–194.

Fyhn, M., Hafting, T., Witter, M.P., Moser, E.I., and Moser, M.-B. (2008). Grid cells in mice. Hippocampus *18*, 1230–1238.

Gatome, C.W., Slomianka, L., Lipp, H.P., and Amrein, I. (2010). Number estimates of neuronal phenotypes in layer II of the medial entorhinal cortex of rat and mouse. Neuroscience *170*, 156–165.

Geisler, C., Diba, K., Pastalkova, E., Mizuseki, K., Royer, S., and Buzsáki, G. (2010). Temporal delays among place cells determine the frequency of population theta oscillations in the hippocampus. Proc. Natl. Acad. Sci.

Gil, M., Ancau, M., Schlesiger, M.I., Neitz, A., Allen, K., De Marco, R.J., and Monyer, H. (2018). Impaired path integration in mice with disrupted grid cell firing. Nat. Neurosci. *21*, 81–91.

Giocomo, L.M., and Hasselmo, M.E. (2008). Time Constants of h Current in Layer II Stellate Cells Differ along the Dorsal to Ventral Axis of Medial Entorhinal Cortex. J. Neurosci.

Giocomo, L.M., and Hasselmo, M.E. (2009). Knock-Out of HCN1 Subunit Flattens Dorsal-Ventral Frequency Gradient of Medial Entorhinal Neurons in Adult Mice. J. Neurosci.

Giocomo, L.M., Zilli, E.A., Fransén, E., and Hasselmo, M.E. (2007). Temporal frequency of subthreshold oscillations scales with entorhinal grid cell field spacing. Science (80-.).

Giocomo, L.M., Hussaini, S.A., Zheng, F., Kandel, E.R., Moser, M.-B., and Moser, E.I. (2011a). Grid cells use HCN1 channels for spatial scaling. Cell *147*, 1159–1170.

Giocomo, L.M., Stensola, T., Bonnevie, T., Van Cauter, T., Moser, M.B., and Moser, E.I. (2014). Topography of head direction cells in medial entorhinal cortex. Curr. Biol. *24*, 252–262.

Giocomo, L.M.M., Moser, M.-B.B., and Moser, E.I.I. (2011b). Computational models of grid cells.

Gloveli, T., Schmitz, D., Empson, R.M., Dugladze, T., and Heinemann, U. (1997). Morphological and electrophysiological characterization of layer III cells of the medial entorhinal cortex of the rat. Neuroscience.

Gonzalez-Sulser, A., and Nolan, M.F. (2016). Grid cells' need for speed. Nat. Neurosci. *20*, 1–2.

Gonzalez-Sulser, A., Parthier, D., Candela, A., McClure, C., Pastoll, H., Garden, D., Surmeli, G., and Nolan, M.F. (2014). GABAergic Projections from the Medial Septum Selectively Inhibit Interneurons in the Medial Entorhinal Cortex. J. Neurosci. *34*, 16739–16743.

Goutagny, R., Jackson, J., and Williams, S. (2009). Self-generated theta oscillations in the hippocampus. Nat. Neurosci.

Goutagny, R., Gu, N., Cavanagh, C., Jackson, J., Chabot, J.-G.G., Quirion, R., Krantic, S., and Williams, S. (2013). Alterations in hippocampal network oscillations and theta-gamma coupling arise before Aβ overproduction in a mouse model of Alzheimer's disease. Eur. J. Neurosci. *37*, 1896–1902.

van Groen, T., and Wyss, J.M. (1990). The postsubicular cortex in the rat: characterization of the fourth region of the subicular cortex and its connections. Brain Res. *529*, 165–177.

van Groen, T., Miettinen, P., and Kadish, I. (2003). The entorhinal cortex of the mouse: Organization of the projection to the hippocampal formation. Hippocampus *13*, 133–149.

Grossberg, S., and Pilly, P.K. (2012). How Entorhinal Grid Cells May Learn Multiple Spatial Scales from a Dorsoventral Gradient of Cell Response Rates in a Self-organizing Map. PLoS Comput. Biol.

Gu, Y., Lewallen, S., Kinkhabwala, A.A., Domnisoru, C., Yoon, K., Gauthier, J.L., Fiete, I.R., and Tank, D.W. (2018). A Map-like Micro-Organization of Grid Cells in the Medial Entorhinal Cortex. Cell.

Guzman, S.J., Schlögl, A., Frotscher, M., and Jonas, P. (2016). Synaptic mechanisms of pattern completion in the hippocampal CA3 network. Science (80-.). *353*, 1117–1123.

van Haeften, T., Baks-te-Bulte, L., Goede, P.H., Wouterlood, F.G., and Witter, M.P. (2003).

Morphological and numerical analysis of synaptic interactions between neurons in deep and superficial layers of the entorhinal cortex of the rat. Hippocampus.

Hafting, T., Fyhn, M., Molden, S., Moser, M.-B.B., and Moser, E.I. (2005). Microstructure of a spatial map in the entorhinal cortex. Nature *436*, 801–806.

Hafting, T., Fyhn, M., Bonnevie, T., Moser, M.-B.B., and Moser, E.I. (2008). Hippocampus-independent phase precession in entorhinal grid cells. Nature *453*, 1248–1252.

Hales, J.B., Schlesiger, M.I., Leutgeb, J.K., Squire, L.R., Leutgeb, S., and Clark, R.E. (2014). Medial entorhinal cortex lesions only partially disrupt hippocampal place cells and hippocampus-dependent place memory. Cell Rep. *9*, 893–901.

Harris, K.D., Henze, D.A., Hirase, H., Leinekugel, X., Dragoi, G., Czurkó, A., and Buzsáki, G. (2002). Spike train dynamics predicts theta-related phase precession in hippocampal pyramidal cells. Nature.

Harvey, C.D., Collman, F., Dombeck, D.A., and Tank, D.W. (2009). Intracellular dynamics of hippocampal place cells during virtual navigation. Nature.

Hasselmo, M.E. (2008). Grid cell mechanisms and function: Contributions of entorhinal persistent spiking and phase resetting. Hippocampus *18*, 1213–1229.

Hasselmo, M.E., Giocomo, L.M., and Zilli, E.A. (2007). Grid cell firing may arise from interference of theta frequency membrane potential oscillations in single neurons. Hippocampus *17*, 1252–1271.

Hinman, J.R., Brandon, M.P., Climer, J.R., Chapman, G.W., and Hasselmo, M.E. (2016). Multiple Running Speed Signals in Medial Entorhinal Cortex. Neuron *91*, 666–679.

Hippocrates (1990). On the Sacred Disease. Gt. Books West. World.

Jacobs, J., Weidemann, C.T., Miller, J.F., Solway, A., Burke, J.F., Wei, X.-X., Suthana, N., Sperling, M.R., Sharan, A.D., Fried, I., et al. (2013). Direct recordings of grid-like neuronal activity in human spatial navigation. Nat. Neurosci. *16*, 1188–1190.

Jadhav, S.P., Kemere, C., German, P.W., and Frank, L.M. (2012). Awake Hippocampal Sharp-Wave Ripples Support Spatial Memory. Science (80-.). *336*, 1454–1458.

Jaramillo, J., Schmidt, R., and Kempter, R. (2014). Modeling Inheritance of Phase Precession in the Hippocampal Formation. J. Neurosci.

Jeewajee, A., Barry, C., O'Keefe, J., and Burgess, N. (2008). Grid cells and theta as oscillatory interference: Electrophysiological data from freely moving rats. Hippocampus *18*, 1175–1185.

Joshi, A., Salib, M., Viney, T.J., Dupret, D., and Somogyi, P. (2017). Behavior-Dependent Activity and Synaptic Organization of Septo-hippocampal GABAergic Neurons Selectively Targeting the Hippocampal CA3 Area. Neuron *96*, 1342–1357.e5.

Justus, D., Dalügge, D., Bothe, S., Fuhrmann, F., Hannes, C., Kaneko, H., Friedrichs, D., Sosulina,

L., Schwarz, I., Elliott, D.A., et al. (2016). Glutamatergic synaptic integration of locomotion speed via septoentorhinal projections. Nat. Neurosci. *20*, 16–19.

Jutras, M.J., Fries, P., and Buffalo, E.A. (2013). Oscillatory activity in the monkey hippocampus during visual exploration and memory formation. Proc. Natl. Acad. Sci.

Kanter, B.R., Lykken, C.M., Avesar, D., Weible, A., Dickinson, J., Dunn, B., Borgesius, N.Z., Roudi, Y., and Kentros, C.G. (2017). A Novel Mechanism for the Grid-to-Place Cell Transformation Revealed by Transgenic Depolarization of Medial Entorhinal Cortex Layer II. Neuron *93*, 1480–1492.e6.

Kemere, C., Carr, M.F., Karlsson, M.P., and Frank, L.M. (2013). Rapid and continuous modulation of hippocampal network state during exploration of new places. PLoS One.

Kennedy, P.J., and Shapiro, M.L. (2009). Motivational states activate distinct hippocampal representations to guide goal-directed behaviors. Proc. Natl. Acad. Sci.

Killian, N.J., Jutras, M.J., and Buffalo, E.A. (2012). A map of visual space in the primate entorhinal cortex. Nature.

King, C., Recce, M., and O'Keefe, J. (1998). The rhythmicity of cells of the medial septum/diagonal band of Broca in the awake freely moving rat: Relationships with behaviour and hippocampal theta. Eur. J. Neurosci. *10*, 464–477.

Kitamura, T., Pignatelli, M., Suh, J., Kohara, K., Yoshiki, A., Abe, K., and Tonegawa, S. (2014). Island cells control temporal association memory. Science *343*, 896–901.

Kitamura, T., Sun, C., Martin, J., Kitch, L.J., Schnitzer, M.J., and Tonegawa, S. (2015). Entorhinal Cortical Ocean Cells Encode Specific Contexts and Drive Context-Specific Fear Memory. Neuron *87*, 1317–1331.

Kleinfeld, D., Deschênes, M., Wang, F., and Moore, J.D. (2014). More than a rhythm of life: Breathing as a binder of orofacial sensation. Nat. Neurosci.

Kloosterman, F., Van Haeften, T., Witter, M.P., and Lopes Da Silva, F.H. (2003). Electrophysiological characterization of interlaminar entorhinal connections: an essential link for re-entrance in the hippocampal-entorhinal system. Eur. J. Neurosci. *18*, 3037–3052.

Knierim, J.J. (2002). Dynamic interactions between local surface cues, distal landmarks, and intrinsic circuitry in hippocampal place cells. J Neurosci *22*, 6254–6264.

Koenig, J., Linder, A.N., Leutgeb, J.K., and Leutgeb, S. (2011). The spatial periodicity of grid cells is not sustained during reduced theta oscillations. Science (80-.). *332*, 592–595.

Kraus, B.J., Robinson, R.J., White, J.A., Eichenbaum, H., and Hasselmo, M.E. (2013). Hippocampal "Time Cells": Time versus Path Integration. Neuron *78*, 1090–1101.

Kraus, B.J., Brandon, M.P., Robinson, R.J., Connerney, M.A., Hasselmo, M.E., and Eichenbaum, H. (2015). During Running in Place, Grid Cells Integrate Elapsed Time and Distance Run. Neuron.

Kropff, E., and Treves, A. (2008). The emergence of grid cells: Intelligent design or just adaptation? Hippocampus *18*, 1256–1269.

Kropff, E., Carmichael, J.E., Moser, M.-B.B., and Moser, E.I. (2015). Speed cells in the medial entorhinal cortex. Nature *523*, 419–424.

Krupic, J., Burgess, N., and O'Keefe, J. (2012). Neural representations of location composed of spatially periodic bands. Science (80-.).

Krupic, J., Bauza, M., Burton, S., Barry, C., and O'Keefe, J. (2015). Grid cell symmetry is shaped by environmental geometry. Nature *518*, 232–235.

Kumar, S.S., Jin, X., Buckmaster, P.S., and Huguenard, J.R. (2007). Recurrent Circuits in Layer II of Medial Entorhinal Cortex in a Model of Temporal Lobe Epilepsy. J. Neurosci.

Langston, R.F., Ainge, J.A., Couey, J.J., Canto, C.B., Bjerknes, T.L., Witter, M.P., Moser, E.I., and Moser, M.-B.B. (2010). Development of the spatial representation system in the rat. Science (80-.). *328*, 1576–1580.

Lashley, K.S. (1950). In Search of the Engram. Soc. Exp. Biol. Symp.

Lee, M.G., Chrobak, J.J., Sik, A., Wiley, R.G., and Buzsáki, G. (1994). Hippocampal theta activity following selective lesion of the septal cholinergic systeM. Neuroscience.

Leung, L.S. (2011). A Model of Intracellular Theta Phase Precession Dependent on Intrinsic Subthreshold Membrane Currents. J. Neurosci.

Leutgeb, S., Leutgeb, J.K., Treves, A., Moser, M.B., and Moser, E.I. (2004). Distinct ensemble codes in hippocampal areas CA3 and CA1. Science (80-.).

Leutgeb, S., Leutgeb, J.K., Barnes, C.A., Moser, E.I., McNaughton, B.L., and Moser, M.B. (2005). Neuroscience: Independent codes for spatial and episodic memory in hippocampal neuronal ensembles. Science (80-.).

Liu, B., Li, P., Sun, Y.J., Li, Y., Zhang, L.I., and Tao, H.W. (2010). Intervening inhibition underlies simple-cell receptive field structure in visual cortex. Nat. Neurosci. *13*, 89–96.

MacDonald, C.J., Lepage, K.Q., Eden, U.T., and Eichenbaum, H. (2011). Hippocampal "Time Cells" Bridge the Gap in Memory for Discontiguous Events. Neuron *71*, 737–749.

MacDonald, C.J., Carrow, S., Place, R., and Eichenbaum, H. (2013). Distinct Hippocampal Time Cell Sequences Represent Odor Memories in Immobilized Rats. J. Neurosci.

Magee, J.C. (2001). Dendritic mechanisms of phase precession in hippocampal CA1 pyramidal neurons. J. Neurophysiol.

Malkova, L., and Mishkin, M. (2003). One-trial memory for object-place associations after separate lesions of hippocampus and posterior parahippocampal region in the monkey. J. Neurosci. *23*, 1956–1965.

Mallory, C.S., Hardcastle, K., Bant, J.S., and Giocomo, L.M. (2018). Grid scale drives the scale and long-term stability of place maps. Nat. Neurosci. *21*, 270–282.

Mattis, J., Tye, K.M., Ferenczi, E.A., Ramakrishnan, C., O'Shea, D.J., Prakash, R., Gunaydin, L.A., Hyun, M., Fenno, L.E., Gradinaru, V., et al. (2012). Principles for applying optogenetic tools derived from direct comparative analysis of microbial opsins. Nat. Methods.

McNaughton, B.L., and Morris, R.G.M. (1987). Hippocampal synaptic enhancement and information storage within a distributed memory system. Trends Neurosci. *10*, 408–415.

McNaughton, B.L., Barnes, C.A., Gerrard, J.L., Gothard, K.M., Jung, M.W., Knierim, J.J., Kudrimoti, H.S., Qin, Y.-L., Skaggs, W.E., Suster, M., et al. (1996). Deciphering the hippocampal polyglot: the hippocampus as a path integration system. J. Exp. Biol.

McNaughton, B.L., Battaglia, F.P., Jensen, O., Moser, E.I., and Moser, M.-B.B. (2006a). Path integration and the neural basis of the "cognitive map."

McNaughton, N., Ruan, M., and Woodnorth, M.A. (2006b). Restoring theta-like rythmicity in rats restores initial learning in the Morris water maze. Hippocampus.

Mehta, M.R. (2001). Neuronal dynamics of predictive coding. Neuroscientist.

Mehta, M.R., Lee, A.K., and Wilson, M.A. (2002). Role of experience and oscillations in transforming a rate code into a temporal code. Nature.

Melzer, S., Michael, M., Caputi, A., Eliava, M., Fuchs, E.C., Whittington, M.A., and Monyer, H. (2012). Long-range-projecting gabaergic neurons modulate inhibition in hippocampus and entorhinal cortex. Science (80-.).

Miao, C., Cao, Q., Moser, M.-B., and Moser, E.I. (2017). Parvalbumin and Somatostatin Interneurons Control Different Space-Coding Networks in the Medial Entorhinal Cortex. Cell *171*, 507–521.e17.

Mishra, R.K., Kim, S., Guzman, S.J., and Jonas, P. (2016). Symmetric spike timing-dependent plasticity at CA3–CA3 synapses optimizes storage and recall in autoassociative networks. Nat. Commun. *7*, 11552.

Mitchell, S.J., Rawlins, J.N.P., Steward, O., and Olton, D.S. (1982). Medial septal area lesions disrupt theta rhythm and cholinergic staining in medial entorhinal cortex and produce impaired radial arm maze behavior in rats. J. Neurosci. *2*, 292–302.

Miyamichi, K., Shlomai-Fuchs, Y., Shu, M., Weissbourd, B.C., Luo, L., and Mizrahi, A. (2013). Dissecting local circuits: Parvalbumin interneurons underlie broad feedback control of olfactory bulb output. Neuron.

Mizumori, S.J., McNaughton, B.L., Barnes, C. a, and Fox, K.B. (1989). Preserved spatial coding in hippocampal CA1 pyramidal cells during reversible suppression of CA3c output: evidence for pattern completion in hippocampus. J. Neurosci.

Mizumori, S.J., Perez, G.M., Alvarado, M.C., Barnes, C.A., and McNaughton, B.L. (1990).

Reversible inactivation of the medial septum differentially affects two forms of learning in rats. Brain Res. *528*, 12–20.

Morris, R.G.M., Garrud, P., Rawlins, J.N.P., and O'Keefe, J. (1982). Place navigation impaired in rats with hippocampal lesions. Nature.

Moser, E.I., Moser, M.-B., Lipa, P., Newton, M., Houston, F.P., Barnes, C.A., and McNaughton, B.L. (2005). A test of the reverberatory activity hypothesis for hippocampal "place" cells. Neuroscience *130*, 519–526.

Muessig, L., Hauser, J., Wills, T.J., and Cacucci, F. (2015). A Developmental Switch in Place Cell Accuracy Coincides with Grid Cell Maturation. Neuron.

Nakazawa, K., Quirk, M.C., Chitwood, R.A., Watanabe, M., Yeckel, M.F., Sun, L.D., Kato, A., Carr, C.A., Johnston, D., Wilson, M.A., et al. (2002). Requirement for hippocampal CA3 NMDA receptors in associative memory recall. Science *297*, 211–218.

Navratilova, Z., Godfrey, K.B., and McNaughton, B.L. (2016). Grids from bands, or bands from grids? An examination of the effects of single unit contamination on grid cell firing fields. J. Neurophysiol.

Newman, E.L., Gillet, S.N., Climer, J.R., and Hasselmo, M.E. (2013). Cholinergic blockade reduces theta-gamma phase amplitude coupling and speed modulation of theta frequency consistent with behavioral effects on encoding. J. Neurosci. *33*, 19635–19646.

Newman, E.L., Climer, J.R., and Hasselmo, M.E. (2014). Grid cell spatial tuning reduced following systemic muscarinic receptor blockade. Hippocampus *24*, 643–655.

O'Keefe, J. (1976). Place units in the hippocampus of the freely moving rat. Exp. Neurol. *51*, 78–109.

O'Keefe, J., and Recce, M.L. (1993). Phase relationship between hippocampal place units and the EEG theta rhythm. Hippocampus *3*, 317–330.

Ohara, S., Onodera, M., Simonsen, Ø.W., Yoshino, R., Hioki, H., Iijima, T., Tsutsui, K.-I., and Witter, M.P. (2018). Intrinsic Projections of Layer Vb Neurons to Layers Va, III, and II in the Lateral and Medial Entorhinal Cortex of the Rat. Cell Rep. *24*, 107–116.

Oliva, A., Fernández-Ruiz, A., Buzsáki, G., and Berényi, A. (2016). Role of Hippocampal CA2 Region in Triggering Sharp-Wave Ripples. Neuron *91*, 1342–1355.

Parron, C., Poucet, B., and Save, E. (2004). Entorhinal cortex lesions impair the use of distal but not proximal landmarks during place navigation in the rat. Behav. Brain Res.

Pastalkova, E., Itskov, V., Amarasingham, A., and Buzsáki, G. (2008). Internally generated cell assembly sequences in the rat hippocampus. Science (80-.). *321*, 1322–1327.

Pastoll, H., Solanka, L., van Rossum, M.C.W., and Nolan, M.F. (2013). Feedback inhibition enables θ-nested γ oscillations and grid firing fields. Neuron *77*, 141–154.

Penfield, W. (1952). Memory mechanisms. Arch. Neurol. Psychiatry *67*, 178.

Petsche, H., Stumpf, C., and Gogolak, G. (1962). The significance of the rabbit's septum as a relay station between the midbrain and the hippocampus I. The control of hippocampus arousal activity by the septum cells. Electroencephalogr. Clin. Neurophysiol.

Pfeiffer, B.E., and Foster, D.J. (2015). Autoassociative dynamics in the generation of sequences of hippocampal place cells. Science (80-.). *349*, 180–183.

Pilly, P.K., and Grossberg, S. (2014). How does the modular organization of entorhinal grid cells develop? Front. Hum. Neurosci. *8*, 337.

Racine, R.J., and Kimble, D.P. (1965). Hippocampal lesions and delayed alternation in the rat. Psychon. Sci. *3*, 285–286.

Raudies, F., Brandon, M.P., Chapman, G.W., and Hasselmo, M.E. (2015). Head direction is coded more strongly than movement direction in a population of entorhinal neurons. Brain Res.

Reifenstein, E.T., Ebbesen, C.L., Tang, Q., Brecht, M., Schreiber, S., and Kempter, R. (2016). Cell-Type Specific Phase Precession in Layer II of the Medial Entorhinal Cortex. J. Neurosci. *36*, 2283–2288.

Rennó-Costa, C., and Tort, A.B.L. (2017). Place and grid cells in a loop: implications for memory function and spatial coding. J. Neurosci.

Rivas, J., Gaztelu, J.M., and García-Austt, E. (1996). Changes in hippocampal cell discharge patterns and theta rhythm spectral properties as a function of walking velocity in the guinea pig. Exp. Brain Res.

Robinson, J., Manseau, F., Ducharme, G., Amilhon, B., Vigneault, E., El Mestikawy, S., and Williams, S. (2016). Optogenetic Activation of Septal Glutamatergic Neurons Drive Hippocampal Theta Rhythms. J. Neurosci.

Robinson, N.T.M., Priestley, J.B., Rueckemann, J.W., Garcia, A.D., Smeglin, V.A., Marino, F.A., and Eichenbaum, H. (2017). Medial Entorhinal Cortex Selectively Supports Temporal Coding by Hippocampal Neurons. Neuron.

Roux, L., Stark, E., Sjulson, L., and Buzsáki, G. (2014). In vivo optogenetic identification and manipulation of GABAergic interneuron subtypes. Curr. Opin. Neurobiol. *26*, 88–95.

Rowland, D.C., and Moser, M.B. (2014). From cortical modules to memories. Curr. Opin. Neurobiol.

Royer, S., Zemelman, B. V., Losonczy, A., Kim, J., Chance, F., Magee, J.C., and Buzsáki, G. (2012). Control of timing, rate and bursts of hippocampal place cells by dendritic and somatic inhibition. Nat. Neurosci. *15*, 769–775.

Sanders, H., Rennó-Costa, C., Idiart, M., and Lisman, J. (2015). Grid Cells and Place Cells: An Integrated View of their Navigational and Memory Function. Trends Neurosci.

Saper, C.B. (2013). The central circadian timing system. Curr. Opin. Neurobiol.

Sargolini, F., Fyhn, M., Hafting, T., McNaughton, B.L., Witter, M.P., Moser, M.-B., and Moser, E.I. (2006). Conjunctive representation of position, direction, and velocity in entorhinal cortex. Science *312*, 758–762.

Schindelin, J., Arganda-Carreras, I., Frise, E., Kaynig, V., Longair, M., Pietzsch, T., Preibisch, S., Rueden, C., Saalfeld, S., Schmid, B., et al. (2012). Fiji: an open-source platform for biological-image analysis. Nat. Methods *9*, 676–682.

Schlesiger, M.I., Cannova, C.C., Boublil, B.L., Hales, J.B., Mankin, E.A., Brandon, M.P., Leutgeb, J.K., Leibold, C., and Leutgeb, S. (2015). The medial entorhinal cortex is necessary for temporal organization of hippocampal neuronal activity. Nat. Neurosci. *18*, 1123–1132.

Schmidt-Hieber, C., and Häusser, M. (2013). Cellular mechanisms of spatial navigation in the medial entorhinal cortex. Nat. Neurosci. *16*, 325–331.

Schmitzer-Torbert, N., Jackson, J., Henze, D., Harris, K., and Redish, A.D. (2005). Quantitative measures of cluster quality for use in extracellular recordings. Neuroscience *131*, 1–11.

Scoville, W.B., and Milner, B. (1957). Loss of recent memory after bilateral hippocampal lesions. J. Neurol. Neurosurg. Psychiatry *20*, 11–21.

Seidler, B., Schmidt, A., Mayr, U., Nakhai, H., Schmid, R.M., Schneider, G., and Saur, D. (2008). A Cre-loxP-based mouse model for conditional somatic gene expression and knockdown in vivo by using avian retroviral vectors. Proc. Natl. Acad. Sci.

Shapiro, M.L., Tanila, H., and Eichenbaum, H. (1997). Cues that hippocampal place cells encode: Dynamic and hierarchical representation of local and distal stimuli. Hippocampus.

Shirvalkar, P.R., Rapp, P.R., and Shapiro, M.L. (2010). Bidirectional changes to hippocampal theta-gamma comodulation predict memory for recent spatial episodes. Proc. Natl. Acad. Sci.

Skaggs, W.E., McNaughton, B.L., Wilson, M.A., and Barnes, C.A. (1996). Theta phase precession in hippocampal neuronal populations and the compression of temporal sequences. Hippocampus *6*, 149–172.

Solstad, T., Moser, E.I., and Einevoll, G.T. (2006). From grid cells to place cells: A mathematical model. Hippocampus.

Solstad, T., Boccara, C.N., Kropff, E., Moser, M.-B., and Moser, E.I. (2008). Representation of geometric borders in the entorhinal cortex. Science *322*, 1865–1868.

Squire, L.R., and Zola-Morgan, S. (1991). The medial temporal lobe memory system. Science (80-.).

Squire, L.R., Stark, C.E.L., and Clark, R.E. (2004). The medial temporal lobe. Annu. Rev. Neurosci. *27*, 279–306.

Steffenach, H.A., Witter, M., Moser, M.B., and Moser, E.I. (2005). Spatial memory in the rat

requires the dorsolateral band of the entorhinal cortex. Neuron.

Stemmler, M., Mathis, A., and Herz, A.V.M. (2015). Neuroscience: Connecting multiple spatial scales to decode the population activity of grid cells. Sci. Adv.

Stensola, H., Stensola, T., Solstad, T., FrØland, K., Moser, M.-B.B., and Moser, E.I. (2012). The entorhinal grid map is discretized. Nature *492*, 72–78.

Van Strien, N.M., Cappaert, N.L.M., and Witter, M.P. (2009). The anatomy of memory: An interactive overview of the parahippocampal- hippocampal network. Nat. Rev. Neurosci.

Sun, C., Kitamura, T., Yamamoto, J., Martin, J., Pignatelli, M., Kitch, L.J., Schnitzer, M.J., and Tonegawa, S. (2015). Distinct speed dependence of entorhinal island and ocean cells, including respective grid cells. Proc. Natl. Acad. Sci. U. S. A. *112*, 9466–9471.

Sürmeli, G., Cosmin, Daniel Marcu, C.M., Garden, D.L.F., Pastoll, H., and Nolan, M.F. (2015). Molecularly Defined Circuitry Reveals Input-Output Segregation in Deep Layers of theMedial Entorhinal Cortex. Neuron *88*, 1040–1053.

Tang, Q., Burgalossi, A., Ebbesen, C.L., Ray, S., Naumann, R., Schmidt, H., Spicher, D., and Brecht, M. (2014). Pyramidal and Stellate Cell Specificity of Grid and Border Representations in Layer 2 of Medial Entorhinal Cortex. Neuron *84*, 1191–1197.

Tang, Q., Ebbesen, C.L., Sanguinetti-Scheck, J.I., Preston-Ferrer, P., Gundlfinger, A., Winterer, J., Beed, P., Ray, S., Naumann, R., Schmitz, D., et al. (2015). Anatomical Organization and Spatiotemporal Firing Patterns of Layer 3 Neurons in the Rat Medial Entorhinal Cortex. J. Neurosci.

Taube, J.S. (2007). The head direction signal: origins and sensory-motor integration. Annu. Rev. Neurosci. *30*, 181–207.

Taube, J.S., Muller, R.U., and Ranck, J.B. (1990). Head-direction cells recorded from the postsubiculum in freely moving rats. I. Description and quantitative analysis. J. Neurosci. *10*, 420–435.

Tocker, G., Barak, O., and Derdikman, D. (2015). Grid cells correlation structure suggests organized feedforward projections into superficial layers of the medial entorhinal cortex. Hippocampus *25*, 1599–1613.

Treves, A., and Rolls, E.T. (1994). Computational analysis of the role of the hippocampus in memory. Hippocampus *4*, 374–391.

Unal, G., Joshi, A., Viney, T.J., Kis, V., and Somogyi, P. (2015). Synaptic Targets of Medial Septal Projections in the Hippocampus and Extrahippocampal Cortices of the Mouse. J. Neurosci.

Vandecasteele, M., Varga, V., Berényi, A., Papp, E., Barthó, P., Venance, L., Freund, T.F., and Buzsáki, G. (2014). Optogenetic activation of septal cholinergic neurons suppresses sharp wave ripples and enhances theta oscillations in the hippocampus. Proc. Natl. Acad. Sci.

Vanderwolf, C.. H. (1969). Hippocampal electrical activity and voluntary movement in the rat.

Electroencephalogr. Clin. Neurophysiol. *26*, 407–418.

Varga, C., Lee, S.Y., and Soltesz, I. (2010). Target-selective GABAergic control of entorhinal cortex output. Nat. Neurosci. *13*, 822–824.

Wall, N.R., Wickersham, I.R., Cetin, A., De La Parra, M., and Callaway, E.M. (2010). Monosynaptic circuit tracing in vivo through Cre-dependent targeting and complementation of modified rabies virus. Proc. Natl. Acad. Sci.

Welday, A.C., Shlifer, I.G., Bloom, M.L., Zhang, K., and Blair, H.T. (2011). Cosine Directional Tuning of Theta Cell Burst Frequencies: Evidence for Spatial Coding by Oscillatory Interference. J. Neurosci.

Wickersham, I.R., Lyon, D.C., Barnard, R.J.O., Mori, T., Finke, S., Conzelmann, K.-K., Young, J.A.T., and Callaway, E.M. (2007). Monosynaptic restriction of transsynaptic tracing from single, genetically targeted neurons. Neuron *53*, 639–647.

Wills, T.J., Cacucci, F., Burgess, N., and O'Keefe, J. (2010). Development of the hippocampal cognitive map in preweanling rats. Science (80-.). *328*, 1573–1576.

Wilson, J.D., Bullock, J.Y., Sutherland, D.C., Main, C., and O'Brien, K.P. (1978). Antinuclear Antibodies in Patients Receiving Non-Practolol Beta-Blockers. Br. Med. J.

Winson, J. (1978). Loss of hippocampal theta rhythm results in spatial memory deficit in the rat. Science *201*, 160–163.

Winter, S.S., Clark, B.J., and Taube, J.S. (2015). Disruption of the head direction cell network impairs the parahippocampal grid cell signal. Science (80-.). *347*, 870–874.

Winterer, J., Maier, N., Wozny, C., Beed, P., Breustedt, J., Evangelista, R., Peng, Y., D'Albis, T., Kempter, R., and Schmitz, D. (2017). Excitatory Microcircuits within Superficial Layers of the Medial Entorhinal Cortex. Cell Rep. *19*, 1110–1116.

Witter, M.P., and Amaral, D.G. (1991). Entorhinal cortex of the monkey: V. Projections to the dentate gyrus, hippocampus, and subicular complex. J. Comp. Neurol. *307*, 437–459.

Witter, P.M., and Amaral, G.D. (2004). Chapter 20 Hippocampal Formation.

Witter, M.P., Griffioen, A.W., Jorritsma-Byham, B., and Krijnen, J.L.M. (1988). Entorhinal projections to the hippocampal CA1 region in the rat: An underestimated pathway. Neurosci. Lett. *85*, 193–198.

Wolf, H. (2011). Odometry and insect navigation. J. Exp. Biol. *214*, 1629–1641.

Wood, E.R., Dudchenko, P.A., Robitsek, R.J., and Eichenbaum, H. (2000). Hippocampal neurons encode information about different types of memory episodes occurring in the same location. Neuron.

Yartsev, M.M., Witter, M.P., and Ulanovsky, N. (2011). Grid cells without theta oscillations in the entorhinal cortex of bats. Nature *479*, 103–107.

Yoder, R.M., and Pang, K.C.H. (2005). Involvement of GABAergic and cholinergic medial septal neurons in hippocampal theta rhythm. Hippocampus *15*, 381–392.

Yu, J., Gutnisky, D.A., Hires, S.A., and Svoboda, K. (2016). Layer 4 fast-spiking interneurons filter thalamocortical signals during active somatosensation. Nat. Neurosci. *19*, 1647–1657.

Zhang, S.-J., Ye, J., Couey, J.J., Witter, M., Moser, E.I., and Moser, M.-B. (2013). Functional connectivity of the entorhinal-hippocampal space circuit. Philos. Trans. R. Soc. B Biol. Sci. *369*, 20120516–20120516.

Zilli, E.A. (2012). Models of Grid Cell Spatial Firing Published 2005–2011. Front. Neural Circuits *6*, 16.

Zilli, E.A., and Hasselmo, M.E. (2010). Coupled Noisy Spiking Neurons as Velocity-Controlled Oscillators in a Model of Grid Cell Spatial Firing. J. Neurosci.

Zugaro, M.B., Monconduit, L., and Buzsáki, G. (2005). Spike phase precession persists after transient intrahippocampal perturbation. Nat. Neurosci. *8*, 67–71.

Zutshi, I., Leutgeb, J.K., and Leutgeb, S. (2017). Theta sequences of grid cell populations can provide a movement-direction signal. Curr. Opin. Behav. Sci. *17*, 147–154.

Zutshi, I., Fu, M.L., Lilascharoen, V., Leutgeb, J.K., Lim, B.K., and Leutgeb, S. (2018a). Recurrent circuits within medial entorhinal cortex superficial layers support grid cell firing. Nat. Commun.

Zutshi, I., Brandon, M.P., Fu, M.L., Donegan, M.L., Leutgeb, J.K., and Leutgeb, S. (2018b). Hippocampal Neural Circuits Respond to Optogenetic Pacing of Theta Frequencies by Generating Accelerated Oscillation Frequencies. Curr. Biol.